Trinity College Dublin
Coláiste na Tríonóide, Baile Átha Cliath
The University of Dublin

Quantum Control of Thermodynamic Processes in Semiconductors

Conor Murphy

A thesis submitted for the degree of

Doctor of Philosophy

2022

Declaration

I declare that this thesis has not been submitted as an exercise for a degree at this or any other university and it is entirely my own work.

I agree to deposit this thesis in the University's open access institutional repository or allow the Library to do so on my behalf, subject to Irish Copyright Legislation and Trinity College Library conditions of use and acknowledgement.

I consent to the examiner retaining a copy of the thesis beyond the examining period, should they so wish (EU GDPR May 2018).

Signed: _____ Date: _____

Summary

In this thesis, we explore theoretically the thermodynamics of heat exchange in laser driven solid state systems. In particular, we focus on the heat exchanged between phonons and a semiconductor quantum dot exciton, driven by both shaped laser pulses and continuous wave lasers, examining how the formation of strong-field dressed states allows a solid state emitter to absorb or emit acoustic phonons in a controlled way. We discuss these effects from the perspective of quantum thermodynamics and outline the possibility of using them to implement controlled thermodynamic processes and for optical cooling of solids to low temperatures, proposing a laser cooling protocol that makes active use of strong coherent driving.

We derive a secularised Bloch-Redfield master equation to calculate the dynamics of an exciton in a GaAs/InGaAs quantum dot, driven by a linearly chirped Gaussian laser pulse. Using full counting statistics, we compute the statistics of the heat transfer between the exciton and the phonon bath, along with the statistics of the work done on the exciton by the driving laser. We construct a thermodynamic cycle, where the laser driving of the exciton forms the hot stroke. Analysing the efficiency of this engine, we identify parameter regimes of the driving laser which lead to quasi reversible heat absorption from the phonons by the quantum dot exciton. We find that certain classes of linearly chirped pulses result in isothermal heat transfers, with heat being absorbed by the exciton when it has a temperature close to that of the phonon bath.

We extend the model of a heat engine composed of a laser driven exciton coupled to phonons to include a driving laser which has a more complex time dependent driving frequency, beyond that of simple linear chirping. Using numerical optimisation methods, we maximise the efficiency with respect to the temporal profile of the frequency of the driving laser. We find that it is always possible to achieve higher efficiencies compared to a linearly chirped pulse, with most improvement found for short Gaussian pulses. Moreover, we find that the frequency profiles of the laser which maximise the efficiency of the heat engine, also lead to increased heat absorption, when compared to their linearly chirped counterparts. These optimised shapes all result in a longer duration for isothermal heat transfer, leading to increased efficiencies.

To analyse the heat absorption that arises from steady state driving, we derive a

secularised Bloch-Redfield master equation, which includes the dissipation due to the spontaneous emission of photons by the quantum dot. We analytically solve for the steady state of the system, and write an analytical expression for the power of the heat absorption from the phonons. The dependence of the heat absorption is explicitly seen in the analytical expression, where the role of the effective temperature of the photon scattering processes is evident. We identify the region in the space of parameters of the driving laser where heat absorption from the phonons is achieved. Finally, we calculate the full probability distribution for the number of excitations exchanged between the exciton and each bath, which appears to have a Gaussian structure at late times, with a mean which shifts linearly in time.

We extend the quantum dot heat pumping model to treat heat pumping of phonons using steady state laser driving of Silicon vacancy centres in diamond. We find that the heat absorption from the phonons is strong enough to counteract the background heating of the material due to the driving laser. With this net heat absorption, we propose a laser cooling protocol based on this driven silicon vacancy platform. In this instance, we use a non-secular Bloch-Redfield master equation along with full counting statistics to calculate the cooling spectrum. The cooling spectra exhibit significant changes with increasing driving strength, where the cooling power is significantly increased and cooling is sustained over a much larger range of driving frequencies. Finally, we compare the cooling spectra from a secular, non-secular and phenomenological Lindblad model, and identify regimes where each theory is appropriate. We find that the secular theory is inappropriate at weak driving, where the secular approximation is invalid due to degeneracies in the Hamiltonian. At strong driving, where the secular approximation is valid, the secular and non-secular theories agree, and at weak driving the non-secular theory and the phenomenological Lindblad theory agree.

Acknowledgements

Firstly, I would like to thank Prof. Paul Eastham for his guidance and support during this PhD.

Over the course of the past four years, I have had the pleasure of sharing an office with some interesting characters, who have been some of my closest friends and to who I owe many thanks.

Outside of physics, I would like to thank Sarah May and my family for their support and encouragement. Finally, I would like to thank Finn and Jack, with whom I've lived with for the majority of my time in Trinity. Without them, living in Dublin would have been an altogether much less enjoyable experience.

List of Publications

C.N. Murphy, P.R. Eastham, Quantum control of excitons for reversible heat transfer, Commun Phys 2, 120, (2019)

P.R. Eastham, C.N. Murphy, Quantum control of solid-state qubits for thermodynamic applications, Proc. SPIE 11702, Photonic Heat Engines: Science and Applications III, 117020I, (2021)

C.N. Murphy, L.T. Tude, P.R. Eastham, Laser cooling beyond rate equations: Approaches from quantum thermodynamics, Applied Sciences 12, no. 3: 1620, (2022)

Contents

List of Figures

1 Introduction

Thermodynamics is a corner stone of classical physics, with four laws governing the behaviour of heat, work and energy in any system. The theory makes no assumptions about the microscopic details of the systems which it describes. Thermodynamics has been the driving force behind technological marvels of the industrial revolution, birthing engines and refrigerators. Now with the ability to create and manipulate systems at the nanoscale which exhibit quantum mechanical features, the interplay between quantum mechanics and thermodynamics is now feasibly addressed in laboratory experiments. Technical questions such as how heat and work are defined in a quantum system and how the third law is satisfied in microscopic systems, which are subject to quantum and thermal fluctuations, are currently active areas of research. Beyond such theoretical questions, there is active research into building the next generation of thermal machines, those composed of microscopic systems whose dynamics are governed by the laws of quantum physics. Such systems have been thriving in nature for hundreds of millions of years, with claims that processes such as photosynthesis exploit quantum coherence to achieve almost maximum efficiencies in the conversion of solar energy to chemical energy [1]. An understanding of how this process works is still not yet complete, and building equivalently efficient quantum thermal machines is in its infancy. In this light, building models of elementary thermal machines composed of simple quantum systems coupled to thermal baths can lead to insights into building more complicated thermal machines.

In this thesis, we examine the thermodynamics of heat exchange between laser driven solid state emitters and the phonons with which they interact. We begin by exploring the potential for typical quantum control schemes used for the state preparation of quantum dot excitons, to induce qausi-reversible heat transfer between the exciton and phonons. Once we understand the role of the strong-field dressed state formation on the control of the heat flows, we begin to design more efficient thermodynamic protocols. We use numerical optimisation methods to show that, in principle, one can achieve a significantly higher degree of reversibility in the transfer of heat with more complex and non-trivial shaped laser pulses.

Moving from time dependent control of excitons in semiconductor quantum dots, we focus on the steady state heat pumping that results from the action of a continuous

wave driving laser. We consider the driven exciton as a heat pump, absorbing heat from the phonon modes of the lattice and emitting this heat into the electromagnetic environment, analysing the steady state mean heat power, along with the statistical properties of the heat transfer.

We then extend our understanding of heat pumping in a quantum dot to the steady state driving of silicon vacancy centres in diamond, where we find the heat absorption from the phonons can overcome the background heating effect due to the driving laser. We propose a laser cooling protocol which makes active use of the strong-field dressed states, resulting from the strong coherent driving. This leads to increased cooling powers and to an overall more robust solid state laser cooling mechanism. We comment on the use of secular and non-secular master equations to model such laser cooling processes, and present results which suggest the secular approximation may not always be appropriate.

In the remainder of this chapter, we introduce the relevant concepts that underpin the results presented. In section 1.1 we provide a general overview of the optical excitation of quantum dots, in both an isolated setting and then in a more realistic environment when the interaction between the exciton and the phonons is considered. In section 1.2 we introduce the basics of quantum thermodynamics. We discuss the elementary model of a maser as a heat engine, which introduces the concept of a virtual temperature of a qubit, before discussing a more dynamical perspective of quantum thermodynamics. We introduce the field of master equations for open quantum systems, a methodology which underpins all results in this thesis and finally discuss the concept of full counting statistics, which allows for the study of the statistical properties of heat and work in open quantum systems. We discuss the field of laser cooling of solids in section 1.3, repeating a classic derivation of the four level model of laser cooling, which is a useful comparison to the strongly and coherently driven silicon vacancy model we report in the results. Lastly, in section 1.4 we give a detailed outline of the remainder of the thesis.

1.1 Semiconductor Quantum Dots and Excitons

The majority of the work in this thesis is concerned with the optical excitation of self-assembled semiconductor quantum dots, with both conventional continuous wave lasers and with more advanced excitation schemes that are generally encountered in the context of quantum control experiments. It is then instructive to review both semiconductor quantum dots themselves, their interactions with light, the intrinsic electron-phonon interaction and the typical quantum control techniques used for state preparation of quantum dot excitons. These will form the basic theoretical background for our results on the thermodynamic properties of laser controlled heat flows in quantum dots.

1.1.1 Introduction to Quantum Dots and Excitons

Semiconductor quantum dots (QD) are zero-dimensional heterostructures, meaning they have a nanoscale extent in all three spatial dimensions. In this thesis, we consider self-assembled semiconductor quantum dots, which are typically grown using the Stranski-Krastanov mechanism. This involves of the deposition of the QD material on a crystal substrate of the host material, layer by layer. Beyond a critical thickness of the layers, growth continues through nucleation, where the formation of nano-islands occurs. The islands are then embedded in the host medium [2]. Choosing a QD material such that it has a lower band gap than the host medium results in a confined system which has discrete states, instead of energy bands, as in conventional solid state systems. These states are confined to the extent of the quantum dot, no longer of the form of delocalised Bloch functions, resulting in a potential landscape sketched in fig. 1.1 seen by the occupying electrons. This energy level structure can be tuned by varying the materials used in order to alter the magnitude of the confining potentials, or by varying the shape and size of the dot in the growth process. The tunability of these heterostructures makes them very useful for many applications, e.g., quantum dot lasers [3], single photon sources [4, 5], quantum information processing and quantum computing [6, 7, 8, 9].

The lowest energy optically active excitation in a semiconductor quantum dot is known as an exciton. The annihilation of an incoming photon, results in a promotion of an electron from it's valence state to the conduction state, which we regard as the creation of an exciton. A bosonic quasi-particle, the exciton is composed of a Coulomb bound electron-hole pair. Excitons are not unique to quantum dots, and also form in bulk semiconductors, between carriers in the conduction and valence bands. However, their binding energies in bulk tend to be very low, and the bound pair thermally dissociates into free carriers [10]. In QDs however, excitons are much more stable, with binding energies often on the order of meV [11]. This increased binding energy is due to the

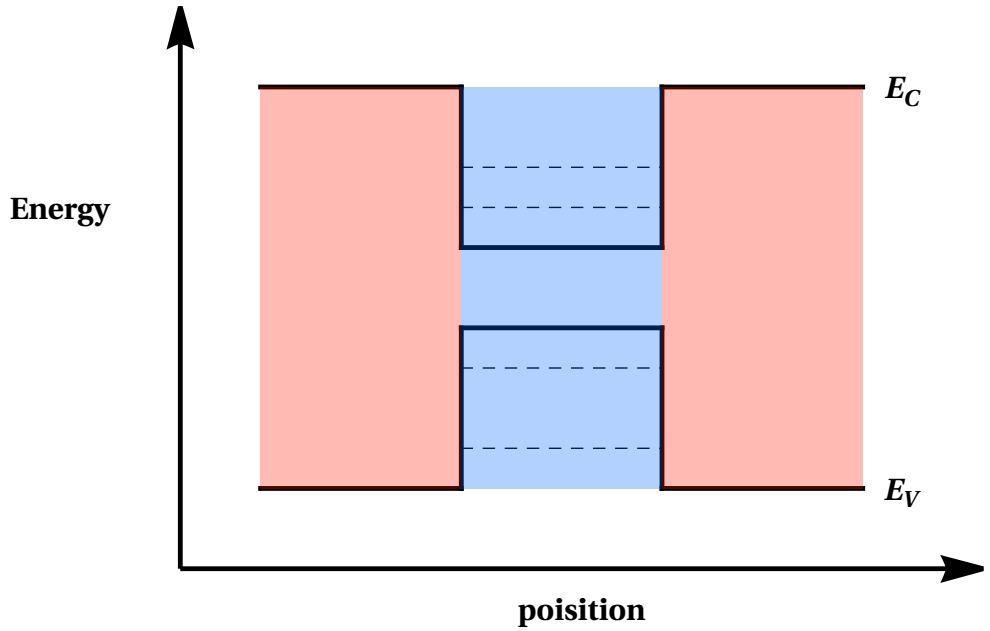

Figure 1.1: Schematic of band structure for a QD in the growth direction, with the resulting discrete states (dashed)

confinement effect of the QD.

Typically, the lowest conduction state has a spin $\pm 1/2$, with the uppermost valence state having a spin of $\pm 3/2$ [12]. This leads to four possible spin states for the exciton, antiparallel spin with total spin ± 1, and parallel spin with total spin ± 2. Including the ground state of the QD and the state with two excitons, there are six excitonic states, which we refer to as the ground state $|g\rangle$, the bright states $|b^{\pm}\rangle$, the dark states $|d^{\pm}\rangle$ and the biexciton state $|B\rangle$ [12]. The bright exciton state is named as such due to the ability to create such a state through the excitation of the QD with circularly polarised light. Correspondingly, it is not possible to create either of the dark states through optical excitation.

The optical activity of these states allows for the optical control of the excitonic degrees of freedom, a crucial ingredient in the development of quantum technologies built from QDs. Beyond control of the excitonic degrees of freedom, quantum control experiments have also been carried out using the internal spin states of QDs [13, 14, 15], with the electron spin having much longer coherence time than that of the exciton in QDs, typically over one microsecond. Quantum dots do however suffer from some limitations, specifically in terms of scalability. If one is to use many QD qubits, single qubit operations require the individual addressing of a single nanostructure with lasers, which typically have beam waists on the order of several optical wavelengths, i.e. several hundred nanometers. For sizeable qubit interactions, the inter-dot spacing needs to be on the order of only several nanometers [16].

1.1.2 Optical Excitation and Control of Semiconductor Quantum Dots

In many applications of quantum dots in technology, the ability to prepare and control excitonic states is required. This is generally achieved through the use of lasers. In this thesis, we will be concerned with the use of lasers to control the flow of energy from phonon modes to the quantum dot. With this in mind, it is useful to review the fundamentals of the optical excitation of quantum dots, specifically under the influence of quantum control based laser schemes. We will initially review optical control of quantum dots in the ideal case of isolated electronic degrees of freedom. Later, we will return to optical control methods, paying special attention to the interaction between the exciton and the phonons.

In this thesis we will use optical excitation schemes exclusively, as such we can neglect the dark state. Moreover, by choosing to work with lasers whose frequencies are not tuned close to the biexciton transition frequency, we can neglect the biexciton states. Lastly, we can specifically optically excite one of the bright states by using circularly polarised light. As such, we can treat the excitonic degrees of freedom as a two level system (TLS), with the ground state denoted $|0\rangle$ and the single exciton state denoted $|1\rangle$. Driving the exciton transition with a constant frequency and constant amplitude laser, we can write the Hamiltonian for the system as

$$H = \frac{\Delta}{2}\left(|1\rangle\langle 1| - |0\rangle\langle 0|\right) - \frac{\Omega}{2}\left(|0\rangle\langle 1| + |1\rangle\langle 0|\right) \tag{1.1}$$

in a frame rotating at the laser frequency and where we have made the rotating wave approximation. $\Delta = E_x - \omega_L$, which we refer to as the detuning i.e., the difference between the exciton transition energy and the frequency of the applied field, and $\Omega = E_0 \langle 0|\, \hat{\vec{d}} \cdot \vec{e}\, |1\rangle$, which is known as the Rabi frequency. We assume an electric field of the form $\vec{E}(t) = \vec{e} E_0 \cos(\omega t)$, with $\vec{e}$ the polarisation vector of the field. Note, a detailed derivation of this Hamiltonian will be presented in chapter 2, where we explicitly perform the unitary transformation and rotating wave approximation mentioned above.

The eigenstates of this Hamiltonian are known as laser dressed states, denoted as $|+\rangle$ and $|-\rangle$, with energies $+\Lambda/2$ and $-\Lambda/2$, where $\Lambda = \sqrt{\Delta^2 + \Omega^2}$. Expanded into the original basis states, these dressed states are of the form

$$\begin{aligned} |-\rangle &= \cos(\phi)\,|0\rangle + \sin(\phi)\,|1\rangle \\ |+\rangle &= -\sin(\phi)\,|0\rangle + \cos(\phi)\,|1\rangle \end{aligned} \tag{1.2}$$

with $\tan\phi = \frac{\Omega}{\Lambda+\Delta}$. For resonant excitation, we have $\phi = \pi/4$, which results in perfectly even superpositions of the original states, as expected.

In the absence of any influence from the phonons, we can solve for the dynamics of the exciton population $p_{1,1} = \langle |1\rangle \langle 1| \rangle$ and the polarisation $p_{0,1} = \langle |0\rangle \langle 1| \rangle$ using the optical Bloch equations[17],

$$\frac{d}{dt}p_{1,1} = -i\frac{\Omega}{2}\left(p_{0,1} - p_{0,1}^*\right), \tag{1.3}$$

$$\frac{d}{dt}p_{0,1} = i\Delta p_{0,1} - i\frac{\Omega}{2}\left(2p_{1,1} - 1\right), \tag{1.4}$$

where we have set $\hbar = 1$.

At this point, it is instructive to specifically examine three different methods of optical excitation of quantum dots: continuous wave excitation, constant frequency laser pulses and linearly chirped laser pulses. Some important changes occur when we consider laser pulses. The electric field envelope as now time dependent, $E_0 \to E_0(t)$, and as such, so too is the Rabi frequency, $\Omega \to \Omega(t)$. For laser pulses with time dependent frequency, the detuning will also be time dependent, $\Delta \to \Delta(t) = E_x - \omega(t)$. Both of these changes result in dressed states which now have time dependent decomposition into the basis exciton states, and a time dependent dressed state splitting $\Lambda(t)$. Eqns. 1.3 and 1.4 remain valid, the only changes being the time dependence of Rabi frequency and detuning. Again, we will derive the Hamiltonian for laser pulses with time dependent frequencies in full in chapter 2. With these optical Bloch equations, we can begin to unwrap the basis of optical control of quantum dots.

From eqns. 1.3 and 1.4 we can see that under the influence of a resonant continuous wave (CW) laser, the exciton population oscillates with a frequency Ω. These are the well known Rabi oscillations, which are shown in fig. 1.2. Once the laser is switched off, i.e. $\Omega = 0$, the exciton population remains unchanged. The amplitude of the occupation oscillation is one in the case of a resonant excitation, but decreases as the laser is detuned further and further from the exciton transition frequency.

In practice, CW lasers are not used for state preparation in QD excitons, laser pulses are often used instead. In this case, the Rabi frequency becomes a time dependent quantity, $\Omega(t)$, due to the time dependence of the envelope function of the electric field. Using a Gaussian laser pulse, the Rabi frequency will also have a Gaussian temporal structure. In fact, not much is changed as we shift from a CW laser driving to that of a laser pulse. We define a quantity known as the pulse area as the time integrated Rabi frequency [12],

$$\theta = \int_{-\infty}^{+\infty} \Omega(t)dt.$$

The exciton occupation is an oscillatory function of the pulse area, identical to the case of CW laser, the Rabi oscillations we mentioned above. To generate the single exciton state, $|1\rangle$, with unit probability, a pulse area which is an odd integer multiple

of π is needed. This method of generating excitons is limited, with the final occupation sensitive to fluctuations in both the frequency of the applied laser and to the pulse area. Despite this sensitivity to both the pulse area and driving frequency, population inversion of excitons has been achieved in QDs via Rabi rotations [18, 19, 20, 21]. If one considers ensembles of quantum dots, population inversion of the entire ensemble is impossible. This is due to the variation of the energy of the excitons and their coupling to the laser, owing to inhomogeneities in the growth process [22]. This spread of exciton energies is known as inhomogeneous broadening. When one considers the effect of the phonons, this method is in general even further limited, as we will see later. We note that the pulse area analysis breaks down in the limit of ultra-short pulses [23, 24], where the slowly varying envelope approximation, used to derive the coupled matter-Maxwell equations, is no longer valid.

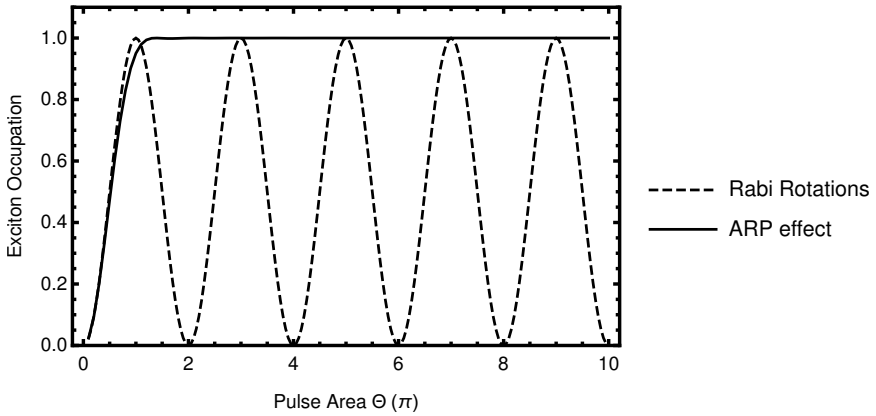

Figure 1.2: Exciton occupation as a function of pulse area for a resonant CW laser/pulse (dashed) and for ARP protocol (solid).

Using chirped laser pulses, a significantly more robust method of optical excitation can be constructed. This is known as the method of adiabatic rapid passage (ARP). A linearly chirped laser pulse refers to one whose instantaneous frequency varies linearly in time. Now, both the frequency of the laser and the Rabi frequency are time dependent quantities, $\omega_l(t)$ and $\Omega(t)$. To generate such pulses, a transform limited Gaussian pulse is passed through a chirp filter. The result of this process is an increase in the temporal width τ, from its original transform limited value τ_0, and a frequency that varies linearly in time. The complex electric field is

$$E(t) = \frac{\theta}{\sqrt{2\pi\tau_0\tau}} e^{-t^2/2\tau^2} e^{-i\left(\omega_l t + \frac{1}{2}at^2\right)}. \tag{1.5}$$

For the detuning and the instantaneous Rabi frequency, we have

$$\Delta(t) = -\frac{at}{a^2+\tau_0^4} \tag{1.6}$$
$$\Omega(t) = \frac{\theta}{\sqrt{2\pi\sqrt{a^2+\tau_0^4}}} e^{\frac{t^2\tau_0^2}{2\left(a^2+\tau_0^4\right)}}.$$

The temporal width of the chirped pulse is related to the temporal width of the unchirped original pulse through [25]

$$\tau^2 = \tau_0^2 + a^2/\tau_0^2.$$

Using a chirped pulse leads to a much more robust method for the creation of an exciton in the QD. Fig. 1.2 shows the exciton occupation under the case of an ARP protocol. The robustness is easily understood if we examine the structure of the dressed states. We wrote the dressed states in eqn. 1.2. Writing them explicitly in terms of the instantaneous detuning, $\Delta(t)$ and Rabi frequency, $\Omega(t)$, we have

$$|-\rangle = \sqrt{\left(\frac{\Lambda(t)-\Delta(t)}{2\Lambda(t)}\right)}|0\rangle + \sqrt{\left(\frac{\Lambda(t)+\Delta(t)}{2\Lambda(t)}\right)}|1\rangle \tag{1.7}$$
$$|+\rangle = -\sqrt{\left(\frac{\Lambda(t)+\Delta(t)}{2\Lambda(t)}\right)}|0\rangle + \sqrt{\left(\frac{\Lambda(t)-\Delta(t)}{2\Lambda(t)}\right)}|1\rangle.$$

As $t \to -\infty$, $\Omega \to 0$ and the dressed states each map to one of the original exciton basis states. For positive spectral chirp, $a > 0$, we have that $|+\rangle_{t\to-\infty} = |0\rangle$ and $|-\rangle_{t\to-\infty} = |1\rangle$. For negative spectral chirp, we have the opposite. Similarly, long after the pulse, as $t \to +\infty$, for the positive spectral chirp we have $|+\rangle_{t\to+\infty} = |1\rangle$ and $|-\rangle_{t\to+\infty} = |0\rangle$, while for negative spectral chirp we have the opposite. Crucially, each of the dressed states map to a different original exciton state, before and after the pulse. Fig. 1.3 shows dressed state energies under a generic ARP protocol, with the mappings to the original exciton basis states indicated for both positive a negative spectral chirp.

Under the action of such an ARP protocol, the system can adiabatically evolve along one of the dressed state trajectories, taking the system from $|0\rangle$ to $|1\rangle$. The sign of the chirping simply determines which of the dressed states the system evolves along. Ignoring the effect of the phonons for now, we can see that this protocol always takes the system from $|0\rangle$ to $|1\rangle$, regardless of the sign of chirp, as long as parameters are chosen such that the adiabatic approximation is valid. The condition for the adiabatic approximation is $\Lambda(t) \gg |\frac{d}{dt}\theta_{\text{phase}}(t)|$, where $\theta_{\text{phase}}(t) = \tan^{-1}(\Delta(t)/\Omega(t))$ is the phase angle. [25]. Fig 1.4 shows a calculation of the final exciton probability as a function of these two parameters, in the absence of the interaction between the exciton and

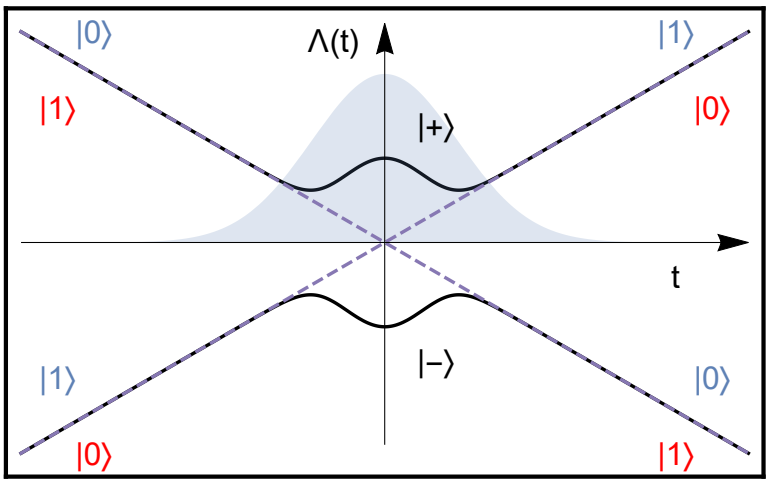

Figure 1.3: Generic dressed state splitting during an ARP driving sequence. The blue shaded region depicts the pulse amplitude. The states in blue (red) denote the dressed state mappings before and after the pulse for the case of negative (positive) spectral chirp.

phonons. This protocol is robust against fluctuations in both the pulse area θ and the chirp a. This robustness is predicted to be a benefit for state preparation in ensembles of QDs, which have a spread of exciton transition frequencies [22].

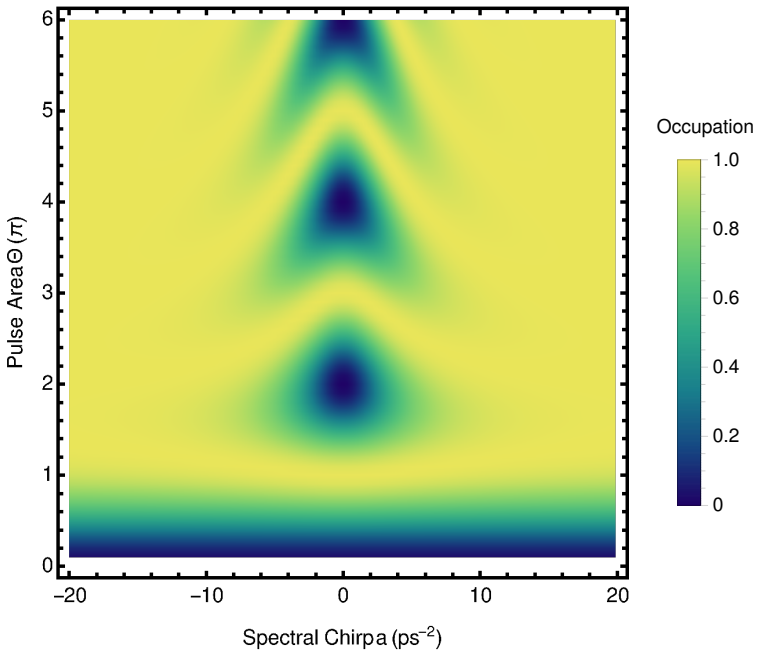

Figure 1.4: A calculation of the final exciton occupation under the action of an adiabatic rapid passage pulse, as a function of the spectral chirp, a and pulse area θ in a closed system.

ARP with quantum dots has been achieved experimentally on the picosecond timescale [26, 27, 28] and on the sub-picosecond timescale [29]. These experimental achievements have paved the way for applications in efficient generation of single and entangled photon sources [5, 30, 31]. ARP has also been proposed for state preparation of multiple interacting two level systems [32], as a method of generating entanglement in an inho-

mogeneous ensemble of interacting quantum dots [33] and as a method for realising a Bose Einstein condensate in ensembles of quantum dots [34].

1.1.3 Exciton-Phonon Interaction

Quantum dots are often referred to as artificial atoms, as they exhibit many of the same features as atomic systems in terms of their discrete level structures. However, important differences arise in the optical properties of quantum dots and atomic systems due to the embedding of the QD within a host crystal, leading to interactions between the carriers and the phononic bath of the surrounding medium, an interaction that is clearly absent in atomic systems. This difference manifests itself in the emission and absorption spectra, which show features such as a sharp zero phonon line along with phonon sidebands [35] due to the optical phonons and a broad background due to the acoustic phonons [36, 37, 38]. This interaction also introduces new decoherence channels, limiting their applicability in quantum technologies that rely on long-lived coherences.

In semiconductor quantum dots made from materials such as GaAs, as considered in this thesis, there are six phonon modes: one longitudinal acoustic (LA), two transverse acoustic (TA), one longitudinal optic (LO) and two transverse optic (TO) modes. Although the electrons in a semiconductor quantum dot exhibit confinement in all three spatial dimensions, we can consider the phonons modes as bulk phonon modes, due to the small lattice mismatch between the QD material and the material of the host medium [12].

There are three electron-phonon coupling mechanisms present in semiconductor QDs. The deformation potential coupling, which couples the exciton to the LA modes, the piezoelectric coupling, which couples the exciton to all acoustic modes, and the Frölich coupling of the exciton to the LO mode. For low energy states in qubits (long wavelength states close to the band edge), the dominant coupling mechanism is deformation potential coupling [14, 36, 37, 39, 40, 41, 42]. These states will have the largest interaction with small wave vector phonons. A position dependent energy results from inhomogeneous displacements of the lattice positions, which locally alter the band gap of the electrons. The coupling of the phonons to the charge density results in a coupling to the exciton, as the exciton states have different charge configurations. This coupling is of a pure dephasing form, with a Hamiltonian

$$H_{\mathrm{e-ph}} = \sum_q \left(|1\rangle\langle 1| - |0\rangle\langle 0| \right) g_q \left(b_q + b_q^\dagger \right). \tag{1.8}$$

When discussing electron-phonon interactions, we can use the spectral density to quantify the electron-phonon coupling. Defined formally as $J(\omega) = \sum_q |g_q|^2 \delta(\omega - \omega_q)$, the spectral density can be calculated explicitly once a geometry is specified for the quan-

tum dot. In the case of spherical and elliptical QDs, the spectral density has been calculated analytically [43, 44]. It is useful however to use a simplified form,

$$J(\omega) = A\omega^3 e^{-\frac{\omega^2}{\omega_c^2}},$$

which has the same features seen in the calculations for both. For small energies the spectral density increases as ω^3, while for large frequencies, it decreases exponentially. This exponential decay of the spectral density is captured by the cutoff frequency ω_c [42]. Fig. 1.5 shows the spectral density for the exciton phonon interaction in a GaAs/InGaAs quantum dot as considered in this thesis. The parameters for this system will be specified later in chapter 2. Qualitatively, the spectral density shows a peak value at some energy, and remains finite over a small finite range of frequencies. From this simple model, we can see that phonons of sufficiently large energy are essentially uncoupled from the excitonic degrees of freedom of the quantum dot.

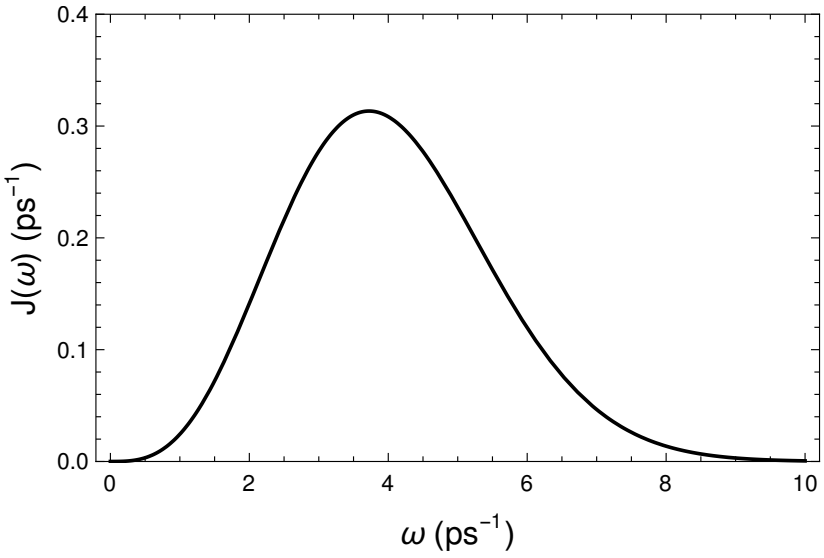

Figure 1.5: Spectral density for the exciton-phonon interaction in a GaAs/InGaAs quantum dot.

1.1.4 Influence of Phonons on the Optical Excitation of Semiconductor Quantum Dots

Returning to the state preparation schemes, the interaction between the excitons and phonons will hinder the effectiveness of the optical excitation protocols we reviewed. Although the interaction Hamiltonian is of a pure dephasing structure, when written in the basis of the laser dressed states, it takes the form

$$H_{e-ph} = \left(\cos^2\theta\,|+\rangle\langle+| + \sin^2\theta\,|-\rangle\langle-| + \sin 2\theta\,(|-\rangle\langle+| + |+\rangle\langle-|)\right)\sum_q \left(g_q b_q + g_q^* b_q^\dagger\right). \tag{1.9}$$

In this basis, the coupling has a pure dephasing term and also terms which lead to transitions between the dressed states. It is clear when we look at the interaction Hamiltonian in this basis that the laser field induces an energy flow between the phononic and excitonic degrees of freedom.

If we include the effects of the phonons into the optical excitation schemes discussed previously, we can understand the limitations on the optical state preparation schemes we introduced. The pure dephasing terms in the interaction Hamiltonian lead to a decay of the coherence that the laser driving will induce. Moreover, for the case of the exciton occupation function, the Rabi oscillations will also be damped due to emission and absorption of lattice phonons. Fig. 1.6 shows the damped Rabi oscillations as a function of pulse area, illustrating the effect of the phonon induced damping on the dynamics of the exciton. This was calculated using eqn. 2.24 which we will derive in chapter 2, the master equation describing the dynamics of the laser driven excitonic degrees of freedom under influence of the interaction with the phonons. For a CW pumping scheme, the net effect of the interaction is to take the excitonic degree of freedom to a thermal state in the basis of laser dressed states, at a temperature equal to that of the host lattice, T_L. The steady state of the exciton will then be

$$\rho_{ss} = e^{-\Lambda/k_B T_L} \left|+\right\rangle \left\langle+\right| + \left(1 - e^{-\Lambda/k_B T_L}\right) \left|-\right\rangle \left\langle-\right| . \tag{1.10}$$

In the case of the constant frequency Gaussian laser pulse, the interaction has the same effect, to bring the system towards the thermal state written above. To circumvent this, shorter pulses can be used, to limit the duration of time with which the exciton and phonons interact. It is important to note, however, that by shortening the duration of the pulse, larger Rabi frequencies may need to be used to generate the desired pulse area. The exciton-phonon scattering rates are proportional to $\Omega^2 J(\Lambda)$, a result which we derive later. Increasing Ω will initially act to increase the exciton-phonon scattering rates, for small Ω. However, as Ω is increased such that bath is sampled at a dressed state splitting, Λ, that is greater than the position of the peak in the spectral density, the scattering rates then begin to drop off with increasing Ω.

The effect on of the phonons on the ARP protocol is more interesting. The ARP protocol offered the most robust method of state preparation, and we saw the basic principle of its operation in fig 1.3, in terms of the dressed state trajectories. In this framework, the emission and absorption of phonons are associated with the system jumping between these states. Now including the effect of the exciton phonon interaction, fig. 1.7 shows a calculation of the final exciton occupation as a function of both the chirp and the pulse area, after an ARP pulse, illustrating the damping effect of the phonons at a temperature of 20 K. Again, this was calculated using 2.24 which we will derive in chapter 2. We now see an asymmetry with respect to the sign of the chirp. The protocol is practically useless in the case of negative spectral chirp, while for the

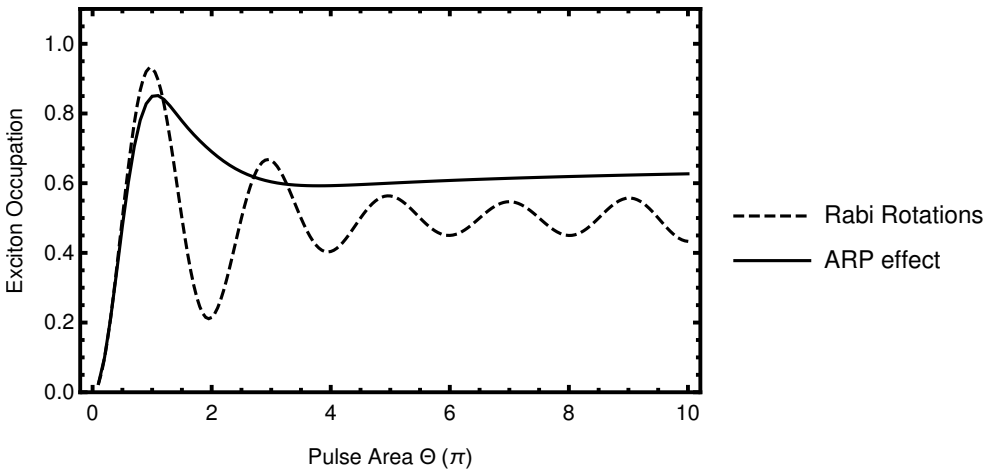

Figure 1.6: A calculation of the exciton occupation as a function of pulse area for a resonant CW laser of laser pulse (dashed) and for the ARP protocol (solid), including the damping effect of the phonons at a temperature of 20 K.

positive spectral chirp we see that the final occupation is now less than unity. This deviation from unity will depend on temperature.

As in the previous cases, the simplest approach to minimising the effect of the phonons is to simply lower the temperature of the lattice. This is an effective method in the case of ARP. As for the asymmetry in the chirp parameter, this can be explained by looking at the composition of the dressed states at early times before the pulse. We saw that for the negative spectral chirp, the $|0\rangle$ state corresponded to the upper dressed state at early times, with the converse being true for positive spectral chirp. The result is that during the initial evolution, as soon as the pulse amplitude is non-negligible, the system will attempt to thermalise with the lattice, in the basis of laser dressed states, and so spontaneously emit phonons until the majority of the population is in the lower dressed state, which for negative spectral chirp, corresponds to $|0\rangle$ at late times. The positive spectral chirp trajectories involve the system evolving along the lower dressed state, the interaction with the phonons cause some population to be excited into the upper dressed state, but at the end of the protocol, the majority of the population resides in the lower dressed state, which is $|1\rangle$. The effectiveness of this approach is sensitive to temperature, and it works best at low temperatures [41, 45].

It is possible to make active use of the phonons for state preparation, in contrast to their hindering effect on Rabi oscillations, as discussed above. It is actively used in a protocol for robust, high fidelity and fast preparation of excitons and biexcitons using off resonant strong laser pulses [46]. This method combines the simplicity of the traditional Rabi oscillation methods with the robustness of adiabatic rapid passage protocols, and not only performs well at strong exciton-phonon coupling (where other schemes fail) but is instead improved. By driving the dot with a blue detuned laser pulse, which is not so strong that the coupling to the phonons vanishes due to the cutoff in the spectral density, the population of the system can incoherently relax from

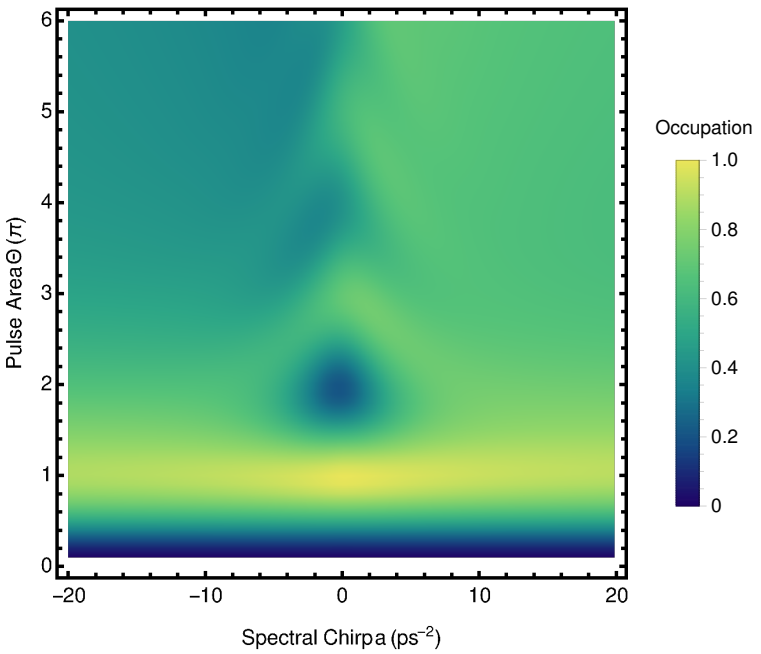

Figure 1.7: A calculation of the final exciton occupations under the action of an adiabatic rapid passage pulse, as a function of the spectral chirp, a and pulse area θ, including the damping effect of the phonons at a temperature of 20 K.

the upper to lower dressed state via the emission of phonons. The blue detuning is key, so that the lower dressed state has a significant excitonic fraction. It is necessary that the pulse duration is long enough such that the population tends towards the thermal occupation of the dressed basis that would be reached for a continuous wave driving laser as shown in [47]. This proposal for incoherent population inversion has since been experimentally verified for both the exciton and bi-exciton states [48, 49, 50]. These processes are of course sensitive to the temperature of the lattice. This ability to control the coupling between the exciton and the acoustic phonon has been dubbed dynamic vibronic coupling and has also been used to incoherently depopulate the exciton on a timescale of 20 ps, an order of magnitude faster than optical decay [51, 52].

An effective method to overcome the limitations induced by the phonons on state preparation is to work in the so-called reappearance regime. We have mentioned that with suitably large dressed state splittings, the spectral density $J(\Lambda)$ is probed at energies beyond its peak, thus resulting in reduced scattering rates. By observing Rabi oscillations at increasing values of the Rabi frequency, the initially increasingly damped oscillations begin to reappear. This is what is known as the reappearance phenomenon [53]. Fig. 1.8 shows the reappearance phenomenon. For sufficiently large pulse area, we see that the Rabi rotations reappear. This has been predicted for Rabi rotations but has not yet been seen experimentally, due to large pulse areas that are needed. For resonant pulses, the dressed state splitting will always cross the strong coupling region of the spectral density. However, for ARP, this can be avoided. The chirping of the laser frequency allows one to design laser dressed splitting profiles which are always

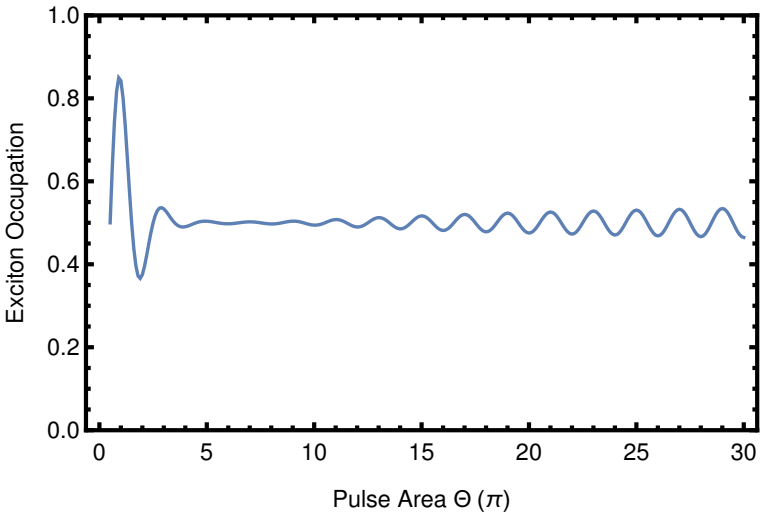

Figure 1.8: Reappearance of the Rabi rotations for sufficiently large pulse areas, with the phonon bath at a temperature of 50 K.

larger than the values for which the coupling is strong, avoiding increased scattering rates. Reappearance in ARP has been reported [45, 54]. To achieve this, high chirp rates are needed.

1.2 Quantum Thermodynamics and Open Quantum Systems

Quantum thermodynamics is fundamentally concerned with the thermodynamics of single or few particle quantum systems. The laws of thermodynamics, the first two of which are

$$\begin{aligned} dU &= dQ + dW, \\ \Delta S &\geq \int \frac{dQ}{T}, \end{aligned} \tag{1.11}$$

were originally derived for macroscopic systems. When we shrink thermal machines down to the scale of atoms, fluctuations in these thermodynamic quantities, both quantum and thermal, are no longer negligible, and quantities like heat and work become stochastic. It is then natural to ask, is it possible to derive the laws of classical macroscopic thermodynamics from the principles of quantum mechanics, rendering thermodynamics as emergent from quantum theory?

Beyond such fundamental questions, there are many practical technological applications for which quantum thermodynamics can be deployed. Cutting edge quantum technology, such as digital and analogue quantum computers, are by their very nature composed of small interacting quantum systems, qubits. Much like classical computation, where Landauer showed in 1961 that the erasure of a single bit of information must lead to the dissipation of heat, related to a change in information entropy [55], a limiting factor of these quantum technologies is heat dissipation. Thermodynamic laws can put fundamental bounds on the performance of these technologies. This is true beyond just quantum computers, and holds for many quantum machines. Thermodynamic arguments can be used to quantify the potential benefit that quantum thermal machines may have over classical equivalents, that arise due to quantum mechanical effects.

We begin by defining the concept of a thermal machine A thermal machine is a system connected to a set of thermal reservoirs. The two most common situations we encounter are the heat engine and refrigerator. In a heat engine, a thermal gradient across the system, resulting from a difference in temperatures between the baths, drives a heat flow across the system. This heat current is then used as a resource by the system to generate work, which is in turn used to perform a task. The well known Carnot efficiency is the fundamental upper bound on the efficiency of such a process, and is

$$\eta = 1 - \frac{T_C}{T_H}. \tag{1.12}$$

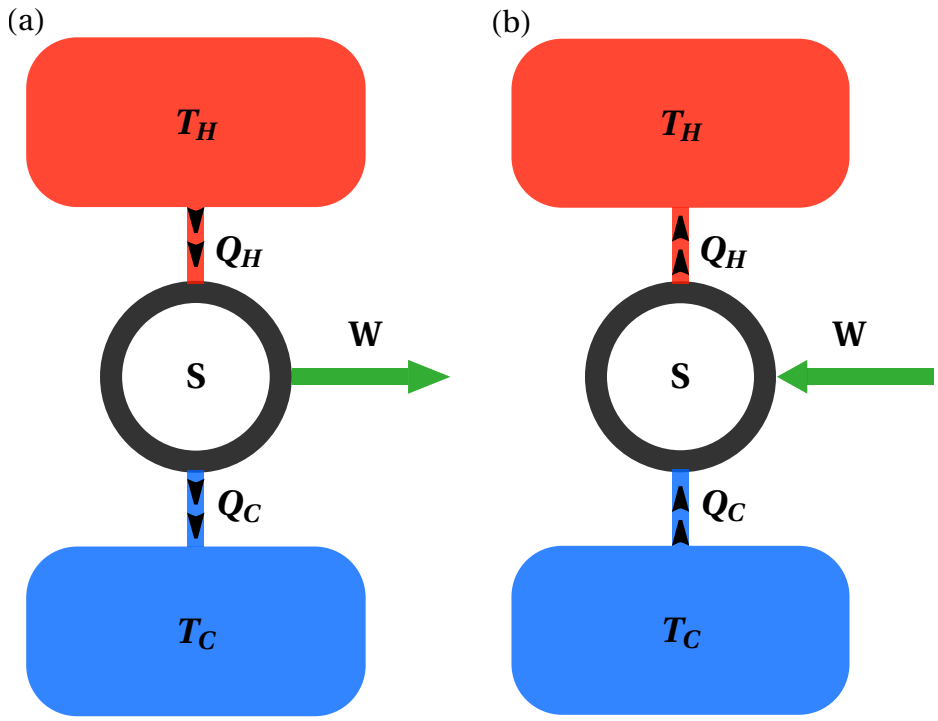

Figure 1.9: Schematic of a heat engine (a) and a refrigerator (b). The green arrow denotes a work flow out of/into the system.

A refrigerator operates in the reverse direction. Work is supplied to the system in order to drive a heat current in the opposite direction, cooling the cold reservoir. Fig. 1.9 provides a general schematic of the operation of a heat engine and a refrigerator.

Shifting from a classical thermal machine to a quantum thermal machine, it is important to understand which features of quantum systems change the behaviour of thermal machines, and moreover, understand if these effects are always beneficial. The most basic quantum feature that a quantum thermal machine may possess is coherence. The extraction of work from a single heat bath has been predicted to benefit from quantum coherence and quantum correlations [56, 57, 58, 59]. Quantum coherence has even been suggested to increase the efficiency in solar cells [33, 60], which results in a quantum limit for the photovoltaic operation that exceeds the classical limit. Similarly, it has been proposed that noise induced coherence can increase the power of a photocell quantum heat engine, by breaking detailed balance [60]. This coherence would be induced through the thermal reservoirs driving the heat engine and is robust against environmental decoherence.

However, many of the benefits seen in the above examples were attributed to effects from non-thermal reservoirs [60, 61, 62, 63, 64], rather than from the intrinsic quantum nature of the working fluid. Initial predictions were that quantum coherence would generally act to reduce the performance [65, 66, 67, 68, 69, 70]. Subsequent study revealed quantum coherence in the internal states of the system was predicted to have

a measurable effect on the performance of QTMs in the limit of small engine action [71]. This was demonstrated experimentally in a system of nitrogen vacancy (NV) centres [72]. The authors reported a higher output power with respect to that of any equivalent classical machine, and an equivalent output power for a continuous and two-stroke heat engine, as predicted. The same effects were also reported in a heat engine composed of a single atom [73].

There has been a variety of physical system which have been proposed, or in some cases even realised, as a platform for various quantum thermal machines. These include optomechanical setups [74, 75, 76, 77], atom-cavity systems [78], trapped ions [79], superconducting qubits [80, 81] and even single atoms [73, 82]. Many of these proposals and realisations are cyclical thermal machines, analogous to those encountered in classical thermodynamics. Particle exchange thermal machines have also been proposed, composed of metallic quantum dots (QD) [83, 84, 85, 86, 87]. Metallic QDs are quasi zero-dimensional quantum structures, coupled to two thermal reservoirs, which can be at different temperatures and chemical potentials. These particle exchange proposals use energy filtering to control the flow of particles [88]. These were predicted to achieve efficiencies that could approach that Carnot limit [86]. Thermoelectric efficiencies at maximum power were also predicted to approach the theoretical maximum, a quantity known the Curzon-Ahlborn efficiency [83, 85, 88]. These predictions have been verified in experimental realisations of quantum dot heat engines [89]. The classic thought experiment, known as Maxwell's demon, was brought to life when it was realised with a cavity coupled to a superconducting qubit [90]. Work was cyclically extracted from the system, connected to a thermal reservoir, by exploiting information about its microstate, revealing the interplay between quantum information and thermodynamics.

We will consider the elementary example of a maser as a heat engine, to introduce the idea of a quantum thermal machine. Following this, we will introduce the concept of an open quantum system and quantum master equations, which provide the natural language with which to discuss quantum thermal machines. From this dynamical perspective of an open quantum system, we will show how the first law of thermodynamics can be derived, and how the traditional Carnot efficiency limit of a heat engine arises. Lastly, we will introduce the field of full counting statistics (FCS), a tool used to quantify the stochastic nature of the thermodynamic variables in quantum thermodynamics.

1.2.1 The Maser as a Heat Engine

One of the first quantum systems to be explored from a thermodynamic perspective was the maser, the microwave equivalent of a laser. Scovil and Schulz-DuBois analysed the operation of a maser as a heat engine [91] in 1959. This was a pivotal work in

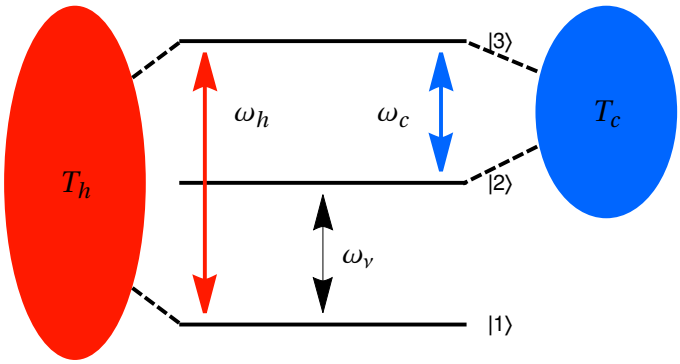

Figure 1.10: Schematic of the maser as a heat engine.

the beginning of the field of quantum thermodynamics. The maser can be effectively described as a three level system, connected to two heat baths, as shown in fig. 1.10. Levels $|1\rangle$ and $|3\rangle$ are split by an energy ω_h and connected to a thermal reservoir at temperature T_h. Levels $|2\rangle$ and $|3\rangle$ are split by an energy ω_c and connected to a heat bath at a temperature T_c. These pairs of levels are in thermal equilibrium with the heat bath they are connected to, resulting in

$$\frac{n_3}{n_1} = e^{-\frac{\omega_h}{k_B T_h}} \tag{1.13}$$

$$\frac{n_3}{n_2} = e^{-\frac{\omega_c}{k_B T_c}} \tag{1.14}$$

Levels $|1\rangle$ and $|2\rangle$ are split by an energy $\omega_\nu = \omega_h - \omega_c$. These levels are not connected to any heat reservoir. Under appropriate conditions, the steady state of the system can have a population inversion in levels $|2\rangle$ and $|1\rangle$, producing the masing effect. The condition for population inversion, defined as $n_2 > n_1$, is

$$\frac{n_2}{n_1} = e^{-(\omega_h/k_B T_h - \omega_c/k_B T_c)} > 1$$

$$\frac{\omega_h}{\omega_c} < \frac{T_h}{T_c}. \tag{1.15}$$

The exchange of energy between the reservoirs and the associated pairs of levels is regarded as heat, and energy exchanged with the field, i.e., the microwave photons emitted from the population inversion between $|2\rangle$ and $|1\rangle$, is regarded as work. From this simple analysis, we have that a closed cycle obeys the first law:

$$\omega_h = \omega_c + \omega_\nu. \tag{1.16}$$

Moreover, we can calculate an efficiency for this engine. The efficiency is defined as the ratio of the microwave photon energy and the hot reservoir excitation energy, the

ratio of work done and the heat absorbed from the hot reservoir,

$$\eta = \frac{\omega_\nu}{\omega_h} = 1 - \frac{\omega_c}{\omega_h} \leq 1 - \frac{T_c}{T_h}. \tag{1.17}$$

$$\tag{1.18}$$

The maser can also be operated as a refrigerator. If we don't work in the regime of population inversion, and instead drive the transition $|1\rangle$ to $|2\rangle$ through some external field, i.e., we perform work on the system, we can take heat from the cold reservoir and dump it into the hot reservoir. The coefficient of performance of this refrigerator is defined as the ratio of the heat absorbed from the cold reservoir and the work done on the system.

$$\text{COP} = \frac{Q_c}{W} \leq \frac{T_c}{T_h - T_c} \tag{1.19}$$

This is the Carnot bound of a refrigerator. The maser obeys the Carnot bounds, and obeys the second law.

1.2.2 Theory of Open Quantum Systems

The example of a maser as a quantum thermal machine is very simple. A more complete analysis of a thermal machine involves knowledge of the state of the quantum system which forms the "working fluid". The theory of open quantum systems provides the natural language and framework to deal with such situations. Open quantum systems are systems which are coupled to large reservoirs or baths, with many degrees of freedom. Typically, we only care about the dynamics of the system itself. As for the reservoirs, these are usually thermal reservoirs, and we only care about their influence on the dynamics of the central systems of interest, and not on their own dynamics. This situation is commonplace in physics, for example, we may wish to model the optical properties of an atom or an optically active defect in a solid. To do this, we must include the spontaneous emission of photons into the electromagnetic environment, and also the interaction of the electrons with the phonons in the case of the solid state defect, but we do not care at all about the state of these fields themselves.

Fig. 1.11 shows a general schematic of an open system. The Hamiltonian for the combined system and environment has many, potentially infinite, degrees of freedom (DOF). However, we only wish to be able to model the dynamics of the small number of DOF that describe the system. The tools we use to model these situations are known as master equations. These are equations of motions of the state of the system, which include the influence of the environment on the system, without capturing the dynamics of the environments themselves.

To derive the quantum master equation for an open system, we begin by writing a

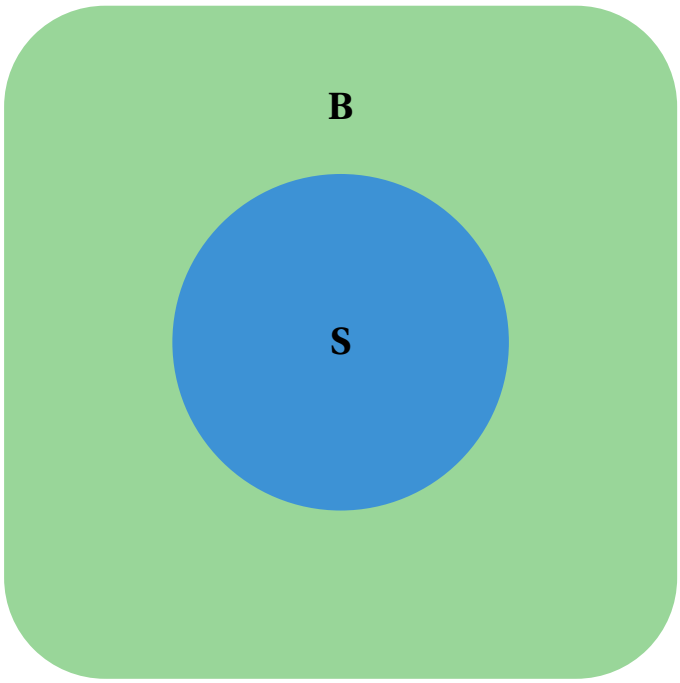

Figure 1.11: Schematic of a system (S) coupled to an environment or bath (B)

general Hamiltonian for a quantum system coupled to an environment,

$$H = H_S + H_B + H_I. \tag{1.20}$$

H_S is the Hamiltonian for the system, H_B is the Hamiltonian for the environment, and H_I is the Hamiltonian for the system-bath interaction. The full state of this combined system and environment will satisfy the unitary evolution

$$\frac{d}{dt}\rho(t) = -i\left[H, \rho(t)\right]. \tag{1.21}$$

Solving for the unitary dynamics of such a system is typically impossible, due to the large number (potentially infinite) of degrees of freedom of the environment. The state of such a combined system and environment, ρ, clearly contains information about both the system and the environment. We define a reduced state, which describes only the state of the system of interest,

$$\rho_S = \mathrm{Tr}_B\left[\rho\right], \tag{1.22}$$

which satisfies

$$\frac{d}{dt}\rho_S(t) = -i\mathrm{Tr}_B\left[H, \rho(t)\right]. \tag{1.23}$$

The Lindblad master equation,

$$\frac{d}{dt}\rho_S(t) = -i\left[H_S, \rho_S(t)\right] + \sum_k \gamma_k \left(A_k \rho_S(t) A_k^\dagger - \frac{1}{2}\left[A_k^\dagger A_k \rho_S(t) + \rho_S(t) A_k^\dagger A_k\right]\right) \tag{1.24}$$

is the most general master equation which is completely positive and trace preserving for any initial condition. This master equation can be derived from rigorous quantum dynamical semigroup arguments [92]. The first term represents the unitary dynamics. The second term captures the effect of the environment on the reduced system. The operators A_k are known as jump operators, and γ_k are the associated rates for these jumps. Note that eqn. 1.24 was not derived from any microscopic theory, and is simply the most general trace-preserving and completely positive form for the equation of motion of the state of the reduced system. With this master equation, one can quickly phenomenologically model an open system by simply choosing the jump operators which have the desired effect, say pure dephasing or population relaxation. For example, if the system of interest is a two-level system with levels $|1\rangle$ and $|2\rangle$ and we want to model its dynamics under the influence of its interaction with an environment, we can include effects of emission and absorption of excitations into and from the bath by including two jump operators, $A_1 = |1\rangle\langle 2|$ and $A_2 = |2\rangle\langle 1|$, as well as specifying the rates for such processes.

It is often more insightful to derive the master equation from a microscopic theory, starting from the Hamiltonian for the combined system and environment. Doing this results in a master equation which can accurately describe real physical systems, rather than a simple phenomenological model. Crucially, a master equation derived from a microscopic theory is only valid under a strict set of conditions and approximations: the condition of initial separability of the state of the total system, the Born approximation, the Markov approximation and the secular approximation. The separability of initial state of the total system ensures there are no initial system-bath correlations, i.e. $\rho(0) = \rho_S(0) \otimes \rho_B(0)$. The Born approximation asserts that the state of the environment is unchanged as a result of the interaction with the system. This means the state of the total system is always uncorrelated, i.e. $\rho(t) = \rho_S(t) \otimes \rho_B$. The Markov approximation implies that the correlation functions of the environment decay much faster than the timescale of the dynamics of the system. The secular approximation is used to discard all fast rotating terms in the interaction picture, such that all transition frequencies in the master equation that satisfy $|\omega_{a,b} - \omega_{c,d}| \ll 1/\tau_{sys}$ are neglected. $\omega_{a,b}$ is the energy gap between levels a and b in the system, and τ_{sys} is the characteristic timescale for the dynamics of the reduced system. The secular approximation is only strictly necessary to obtain Lindblad master equations, which ensures positivity of the density matrix. It is not necessary for all master equations, e.g., the Bloch-Redfield master equation. The secular approximation is also not always valid, it breaks down when the Hamiltonian of the system has degeneracies. We will encounter this scenario when we discuss the silicon vacancy laser cooling protocol outlined in chapter 5, where we will derive a Bloch-Redfield master equation that is not brought into Lindblad form.

It is useful to outline the general procedure for deriving a quantum master equation from a microscopic theory, as we do so many times in this thesis. With a Hamiltonian

partitioned as

$$\hat{H} = \hat{H}_S + \hat{H}_B + \hat{H}_I, \tag{1.25}$$

with $\hat{H}_S$ the Hamiltonian for the system of interest, $\hat{H}_B$ the Hamiltonian of the bath and $\hat{H}_I$ the Hamiltonian describing their interaction. We define the free Hamiltonian of the system and bath as $\hat{H}_0 = \hat{H}_S + \hat{H}_B$. We move to the interaction picture, defining $\tilde{H}_I = e^{i\hat{H}_0 t}\hat{H}_I e^{-i\hat{H}_0 t}$. Note: Operators in the Schrödinger picture will be denoted as $\hat{O}$ and the corresponding operators in the interaction picture as $\tilde{O}$. The density matrix in the interaction picture evolves according to,

$$\frac{\partial}{\partial t}\tilde{\rho}(t) = -i\left[\tilde{H}_I(t), \tilde{\rho}(t)\right], \tag{1.26}$$

which has the formal solution

$$\tilde{\rho}(t) = \tilde{\rho}(0) - i\int_0^t ds\left[\tilde{H}_I(s), \tilde{\rho}(s)\right]. \tag{1.27}$$

Upon substituting this solution back into eqn. 1.26 we get

$$\frac{\partial}{\partial t}\tilde{\rho}(t) = \left[\tilde{H}_I(t), \tilde{\rho}(t_0)\right] - \int_0^t ds\left[\tilde{H}_I(t), \left[\tilde{H}_I(s), \tilde{\rho}(s)\right]\right]. \tag{1.28}$$

Taking the trace over the bath degrees of freedom we find

$$\frac{\partial}{\partial t}\tilde{\rho}_S(t) = \mathrm{Tr}_B\left[\tilde{H}_I(t), \tilde{\rho}(0)\right] - \int_0^t ds\mathrm{Tr}\left[\tilde{H}_I(t), \left[\tilde{H}_I(s), \tilde{\rho}(s)\right]\right], \tag{1.29}$$

for the reduced system density matrix.

At this point, we make the approximations mentioned above. Separability of the initial state, means that

$$\hat{\rho}(0) = \tilde{\rho}(0) = \hat{\rho}_S(0) \otimes \hat{\rho}_B(0). \tag{1.30}$$

We can set the first term on the right-hand side of eqn. 1.29 to zero, which can be justified by removing a term $\mathrm{Tr}_B\left[\hat{H}_I, \rho_B(0)\right]$ from the interaction picture Hamiltonian and including it instead in the system Hamiltonian, and we are left with

$$\frac{\partial}{\partial t}\tilde{\rho}_S(t) = -\int_0^t ds\mathrm{Tr}_B\left[\tilde{H}_I(t), \left[\tilde{H}_I(s), \tilde{\rho}(s)\right]\right]. \tag{1.31}$$

We then make the Born approximation, which assumes that the state of the environment remains unchanged and the density matrix of the total system then factorises at all times as

$$\tilde{\rho}(t) \approx \tilde{\rho}_S(t) \otimes \tilde{\rho}_B. \tag{1.32}$$

This approximation essentially neglects correlations that build up between the system and bath. It is only valid in the limit of a weak system bath interaction. Lastly,

we introduce the Markov approximation, which makes the integro-differential equation time local. At the moment the evolution equation is time non-local as $\tilde{\rho}(t)$ depends on its past history through the integration over $\tilde{\rho}(s)$. To make this time local, we make the replacement $\tilde{\rho}(s) \to \tilde{\rho}(t)$ on the right-hand side of eqn. (1.31). The Markovian master equation in the interaction picture can then be written

$$\frac{\partial}{\partial t}\tilde{\rho}_S(t) = -\int_0^t ds \mathrm{Tr}_B \left[\tilde{H}(t), \left[\tilde{H}_I(s), \tilde{\rho}(t)\right]\right]. \tag{1.33}$$

We decompose the Hamiltonian as $\hat{H}_I = \sum_\alpha \hat{A}_\alpha \otimes \hat{B}_\alpha$ where $\hat{A}_\alpha$ and $\hat{B}_\alpha$ are system and bath operators respectively. In the interaction picture, this Hamiltonian becomes

$$\begin{aligned}\tilde{H}_I &= \sum_\alpha \hat{A}_\alpha(t) \otimes \hat{B}_\alpha(t) \\ &= \sum_\alpha e^{i\hat{H}_s t}\hat{A}_\alpha e^{-i\hat{H}_s t} \otimes e^{i\hat{H}_B t}\hat{B}_\alpha e^{-i\hat{H}_B t}.\end{aligned} \tag{1.34}$$

Expanding the commutators of eqn. (1.33) gives

$$\begin{aligned}\frac{\partial}{\partial t}\tilde{\rho}_S(t) = -\int_0^t ds \mathrm{Tr}_B \{ &\tilde{H}_I(t)\tilde{H}_I(s)\tilde{\rho}_S(t)\tilde{\rho}_E \\ &- \tilde{H}_I(s)\tilde{\rho}_S(t)\tilde{\rho}_B\tilde{H}_I(t) \\ &- \tilde{H}_I(t)\tilde{\rho}_S(t)\tilde{\rho}_B\tilde{H}_I(s) \\ &+ \tilde{\rho}_S(t)\tilde{\rho}_E\tilde{H}_I(s)\tilde{H}_I(t) \}.\end{aligned} \tag{1.35}$$

The master equation can then be written as

$$\begin{aligned}\frac{\partial}{\partial t}\tilde{\rho}_S(t) = -\sum_{\alpha,\beta}\int_0^t ds \Big(&\left[\, \hat{A}_\alpha(t), \hat{A}_\beta(s)\tilde{\rho}_s(t)\right] C_{\alpha,\beta}(t-s) \\ &+ \left[\tilde{\rho}_s(t)\hat{A}_\beta(s), \hat{A}_\alpha(t)\,\right] C_{\beta,\alpha}(s-t)\Big),\end{aligned} \tag{1.36}$$

where we define the correlation functions as

$$C_{\alpha,\beta}(t,s) = \langle \hat{B}_{\alpha(t)}\hat{B}_\beta(s)\rangle_B = \mathrm{Tr}_E\left[\hat{B}_{\alpha(t)}\hat{B}_\beta(s)\hat{\rho}_B\right]. \tag{1.37}$$

In the case that the environment is in a stationary state we can write these more simply as

$$C_{\alpha,\beta}(t,s) = \mathrm{Tr}_E\left[\hat{B}_\alpha(t-s)\hat{B}_\beta\hat{\rho}_E\right] \equiv C_{\alpha,\beta}(t-s). \tag{1.38}$$

Transforming back into the Schröodinger picture, we get a master equation

$$\begin{aligned}\frac{\partial}{\partial t}\hat{\rho}_S(t) = &- i\left[\hat{H}_s, \hat{\rho}_S(t)\right] \\ &- \sum_{\alpha,\beta}\int_0^t ds\left(\left[\,\hat{A}_\alpha(t), \hat{A}_\beta(s)\hat{\rho}_s(t)\right] C_{\alpha,\beta}(t-s)\right. \\ &\left.+\left[\hat{\rho}_s(t)\hat{A}_\beta(s), \hat{A}_\alpha(t)\,\right] C_{\beta,\alpha}(s-t)\right). \end{aligned} \tag{1.39}$$

Specifying a Hamiltonian, and calculating the corresponding correlation functions, this master equation can be used to calculate the dynamics of the system. With further approximations, eqn. 1.39 can give master equations which are of Lindblad form. We will derive a master equation in such a way when we discuss a laser driven quantum dot coupled to the phonon reservoir in chapter 2.

1.2.3 Dynamical Perspective of Quantum Thermodynamics

Returning to thermodynamics, we can now understand some of the fundamental principles of thermodynamics from the perspective of the dynamics of these systems, rather than just a steady state analysis as we saw with the maser. We saw that the general dynamical equation of motion for the state of an open quantum system is of the form

$$\dot{\rho(t)} = -i\left[H, \rho(t)\right] + \mathcal{D}\left[L\right]\rho(t), \tag{1.40}$$

where $\mathcal{D}$ is the dissipator describing the interaction between the system and the environment, and L is some jump operator which models the relevant transition. In 1979 Alicki wrote down a simple but powerful description of heat and work from this dynamical equation [93]. Working in the Heisenberg picture, so that any coherent evolution is captured by the time dependence of the Hamiltonian, and not of the state, the rate of change of the total energy of the system is partitioned as follows:

$$\frac{d}{dt}U = \frac{d}{dt}\langle H\rangle = \mathrm{Tr}\left[\rho(t)\frac{\partial H}{\partial t}\right] + \mathrm{Tr}\left[H\frac{d}{dt}\rho\right], \tag{1.41}$$

$$\frac{d}{dt}\langle H\rangle = \mathrm{Tr}\left[\rho(t)\frac{\partial H}{\partial t}\right] + \mathrm{Tr}\left[H\mathcal{D}\left[\mathcal{L}\right]\rho\right], \tag{1.42}$$

$$\frac{d}{dt}\langle H\rangle = \frac{d}{dt}\langle W\rangle + \frac{d}{dt}\langle Q\rangle. \tag{1.43}$$

This partition has a clear interpretation. Changes in work are associated with changes in the driving Hamiltonian. Changes in heat are associated with a change in the

state,

$$\langle W \rangle = \int dt \mathrm{Tr}\left[\rho(t)\frac{\partial H}{\partial t}\right] \tag{1.44}$$

$$\langle Q \rangle = \int dt \mathrm{Tr}\left[H\frac{d}{dt}\rho\right]. \tag{1.45}$$

We now consider a cyclical process, with a system connected to two reservoirs, with a Hamiltonian $H(t) = H_0 + H'(t)$. A cyclical process implies $H'(t_0) = H'(t_f) = 0$, for a cycle operating from time t_0 to time t_f. Crucially, the change in total energy of the system must satisfy $\Delta U = \Delta W + \Delta Q = 0$. From this condition, we can write

$$-\Delta W = -\int_{t_0}^{t_f} \mathrm{Tr}\left[\rho\frac{\partial H(t)}{\partial t}\right] \tag{1.46}$$

$$= \int_{t_0}^{t_f} \mathrm{Tr}\left[H(t)\dot{\rho}(t)\right] \tag{1.47}$$

$$= \Delta Q_1 + \Delta Q_2, \tag{1.48}$$

where ΔQ_i are the heats exchanged between the system and bath i in the time t_0 to t_f. The total work done must equal to the sum of the changes of heat in the baths. At this point, we can introduce the concept of the entropy production rate, $\sigma(t)$. It is defined as the difference between the rate of change of entropy for the baths, $J^S = J_1^S + J_2^S$, and the rate of change of the entropy of the system, $dS(\rho)/dt$,

$$\sigma(t) = \frac{dS(\rho)}{dt} - J_1^S - J_2^S. \tag{1.49}$$

Alicki proved that this quantity, must satisfy

$$\sigma(t) \geq 0, t \geq 0. \tag{1.50}$$

This is simply a statement that the total change in entropy of the universe must not be negative. We note here, to calculate the entropy of a quantum system, we can use the von Neumann definition,

$$S(\rho) = -k_B \mathrm{Tr}\left[\rho \ln \rho\right]. \tag{1.51}$$

For a thermal reservoir, we know from conventional classical thermodynamics that

$$J_i^S = \frac{1}{k_B T_i}\frac{dQ_i}{dt}. \tag{1.52}$$

As we are considering a cyclical process, by definition we have $\Delta S_{\mathrm{cycle}} = 0$. As such,

we can assert that

$$0 = \int_{t_0}^{t_f} \frac{dS}{dt} dt = \int_{t_0}^{t_f} \sigma(t) + \frac{1}{k_B T_1} \frac{dQ_1}{dt} + \frac{1}{k_B T_2} \frac{dQ_2}{dt}, \tag{1.53}$$

which leads to the inequality,

$$\frac{1}{k_B T_1} \Delta Q_1 + \frac{1}{k_B T_2} \Delta Q_2 \leq 0. \tag{1.54}$$

Combing this with eqn. 1.48, we can write the efficiency for this cyclical process, as

$$\eta = \frac{-W(t_f)}{Q_1(t_0)} \leq 1 - \frac{T_2}{T_1}. \tag{1.55}$$

We thus retrieve the Carnot efficiency bound from a completely general description of the dynamics of an open quantum system weakly coupled to two thermal reservoirs.

1.2.4 Full Counting Statistics

We have seen how to define heat and work in a driven open quantum system. Fundamentally, however, when we are dealing with systems composed of single or few quantum objects, the fluctuations of thermodynamic quantities become important. At the scale of atoms at low temperatures, both quantum and thermal fluctuations can have significant effects. Maxwell's demon, for example, extracts work by exploiting thermal fluctuations [94, 95]. Thermodynamic quantities such as heat and work are then treated as stochastic variables, in what is known as stochastic thermodynamics. Stochastic thermodynamics has been a powerful tool in predicting the role of fluctuations in small thermodynamic systems, providing fluctuations theorems which such systems must obey [96, 97, 98, 99]. Full counting statistics provides the framework to calculate not only the mean value of thermodynamic quantities as in the previous section, but higher order cumulants, or even a direct calculation of the full probability distribution for heat and work [100, 101].

In this thesis, we will be considering driven quantum systems. As such, we will introduce the method of full counting statistics in this context. Following the treatment outlined in [102], we start with a Hamiltonian partitioned into its system, bath and interaction components $\hat{H}(t) = \hat{H}_S(t) + \hat{H}_{SB} + \hat{H}_B$, where we assume that the interaction term is small compared to both the system and bath free Hamiltonians, i.e. the weak coupling approximation. We define a complete set of projection operators, composed of the instantaneous eigenstates of the free system and bath Hamiltonians, $P_{i,\alpha}(t) = \left|\mathrm{e_i}^S(t)\right\rangle \left\langle \mathrm{e_i}^S(t)\right| \otimes \left|\mathrm{e}_\alpha\right\rangle \left\langle \mathrm{e}_\alpha\right|$. These projection operators then satisfy the fol-

lowing,

$$\hat{H}_S(t)P_{i,\alpha}(t) = \mathrm{e}_{\mathrm{i}}^S(t)P_{i,\alpha}(t), \tag{1.56}$$

$$\hat{H}_B P_{i,\alpha}(t) = \mathrm{e}_\alpha^B P_{i,\alpha}(t), \tag{1.57}$$

$$P_{i,\alpha}^\dagger(t) = P_{i,\alpha}(t), \tag{1.58}$$

$$\sum_{i,\alpha} P_{i,\alpha}(t) = I, \tag{1.59}$$

$$P_{i,\alpha}(t)P_{i',\alpha'}(t) = \delta_{i,i'}\delta_{\alpha,\alpha'}P_{i,\alpha}(t). \tag{1.60}$$

If we perform a measurement of the energy of the system and of the environment at time t_0, the starting time of some driving protocol, we can write the joint probability for measuring system and environmental energies $e_i^S(t_0)$ and $e_\alpha^B(t_0)$ as

$$p_{i,\alpha} = \mathrm{Tr}\left\{P_{i,\alpha}(t_0)\hat{\rho}(t_0)\right\}. \tag{1.61}$$

Measuring the outcomes $e_i^S(t_0)$ and $e_\alpha^B(t_0)$ for the energy of the system and bath, (assuming a non-degenerate spectrum for both the system and bath) the state of the combined system is then projected onto the corresponding state, with the post measurement state given by

$$\hat{\rho}_{i,\alpha} = p_{i,\alpha}^{-1}P_{i,\alpha}(t_0)\hat{\rho}(t_0)P_{i,\alpha}(t_0). \tag{1.62}$$

Performing a second measurement then at t_f, after the driving protocol we are considering, the density matrix has undergone a unitary evolution to

$$\hat{\rho}_{i,\alpha}(t_f) = \hat{U}_{t_f,t_0}\hat{\rho}_{i,\alpha}\hat{U}_{t_f,t_0}^\dagger. \tag{1.63}$$

We can use the conditional probability distribution function (PDF) to characterise the probability of finding the system and environment in energy eigenstates $e_{i'}^S(t_f)$ and $e_{\alpha'}^B(t_f)$ given the results of the first measurements, i.e., having measured the system and bath energies $e_i^S(t_0)$ and $e_\alpha^B(t_0)$. This PDF is written as

$$p_{t_f,t_0}(i',\alpha' \mid i,\alpha) = \mathrm{Tr}\left\{P_{i',\alpha'}(t_f)\hat{\rho}_{i,\alpha}(t_f)\right\}. \tag{1.64}$$

Rewriting this as a conditional PDF for measuring *changes* in energy of the system and environment $\Delta\mathrm{e}^S$ and $\Delta\mathrm{e}^B$, we have

$$p_{t_f,t_0}(\Delta\mathrm{e}^S,\Delta\mathrm{e}^B) = \sum_{i,i',\alpha,\alpha'} \delta(\Delta\mathrm{e}^S - (\mathrm{e}_{i'}^S(t_f) - \mathrm{e}_i^S(t_0))) \\ \delta(\Delta\mathrm{e}^B - (\mathrm{e}_{\alpha'}^B - \mathrm{e}_\alpha^B))p_{t_f,t_0}(i',\alpha' \mid i,\alpha)p_{i,\alpha}. \tag{1.65}$$

For a change $\Delta \mathrm{e}^S$ of the system, we can associate $-\Delta \mathrm{e}^B$ as the amount that corresponds to heat exchanged with the environment. We neglect any small contribution of energy that is stored or released from the interaction Hamiltonian, a valid assumption given the weakly coupled system-bath approximation. The joint PDF of internal energy $E = \Delta \mathrm{e}^S$ and heat exchange Q becomes

$$p_{t_f,t_0}(E,Q) = \sum_{i,i',\alpha,\alpha'} \delta(E - (\mathrm{e}^S_{i'}(t_f) - \mathrm{e}^S_i(t_0))) \times \\ \delta(Q - (\mathrm{e}^B_{\alpha'} - \mathrm{e}^B_\alpha)) p_{t_f,t_0}(i',\alpha' \mid i,\alpha) p_{i,\alpha}. \tag{1.66}$$

Integrating over E, we get the PDF of exchanging an amount of heat Q with the environment, after a time t during the protocol,

$$p(Q,t) = \sum_{\alpha,\alpha'} \delta(Q - (\mathrm{e}^B_{\alpha'} - \mathrm{e}^B_\alpha)) p(\alpha', t \mid \alpha, t_0) p(\alpha, t_0). \tag{1.67}$$

We now write $p(\alpha', t \mid \alpha, t_0)p(\alpha, t_0)$ explicitly in terms of the density matrix, evolution operators, and projection operators, as

$$p(\alpha', t \mid \alpha, t_0)p(\alpha, t_0) = \mathrm{Tr}\left\{ P_{\alpha'} \hat{U}(t,t_0) P_\alpha \hat{\rho}(0) P_\alpha \hat{U}^\dagger(t,t_0) P_{\alpha'} \right\}, \tag{1.68}$$

and we can then define the characteristic function for heat:

$$G_Q(u,t) = \int_{-\infty}^{\infty} dQ p(Q,t) e^{iQu} = \sum_{\alpha,\alpha'} p(\alpha', t \mid \alpha, t_0) p(\alpha, t_0) e^{iu(e_{\alpha'} - e_\alpha)}. \tag{1.69}$$

Assuming the total density matrix factorises at the initial time, and that the initial density matrix of the environment is given by a thermal state,

$$\hat{\rho}_B(0) = \frac{e^{-\beta \hat{H}_B}}{Z_B}, \tag{1.70}$$

we have that all environmental projectors commute with $\hat{\rho}(0)$ and that

$$\sum_{\alpha,\alpha'} P_\alpha e^{\pm iue_\alpha} = e^{\pm iu\hat{H}_B}. \tag{1.71}$$

Then we can write the characteristic function as

$$G_Q(u,t) = \mathrm{Tr}\left\{ U^\dagger(t,t_0) e^{iu\hat{H}_B} U(t,t_0) e^{-iu\hat{H}_B} \hat{\rho}(0) \right\}, \tag{1.72}$$

$$= \mathrm{Tr}\left\{ e^{iu\hat{H}_B/2} U(t,t_0) e^{-iu\hat{H}_B/2} \hat{\rho}(0) e^{-iu\hat{H}_B/2} U^\dagger(t,t_0) e^{iu\hat{H}_B/2} \right\}. \tag{1.73}$$

or more compactly as

$$G_Q(u,t) = \mathrm{Tr}\left\{\hat{\rho}^u(t)\right\} \tag{1.74}$$

with

$$\hat{\rho}^u(t) = \hat{U}_{u/2}(t,t_0)\hat{\rho}(0)\hat{U}^\dagger_{-u/2}(t,t_0), \tag{1.75}$$

$$\hat{U}_{u/2}(t,t_0) = e^{iu\hat{H}_B}\hat{U}(t,t_0)e^{-iu\hat{H}_B}, \tag{1.76}$$

as in [100].

We can use the same formalism, namely the two point projective measurement formalism [102, 103], to calculate the statistics of the work done on the system by some external force. This is only valid in the weak coupling regime, where the interaction energy $\hat{H}_{SB}$ can be neglected. This two point projective measurement involves a projective measurement of the energy of the system before some external force implements a control sequence, and a second projective measurement after the control sequence. Including both the projective measurements of the bath, which count the change in heat, and projective measurements of the energy of the system, we can compute the work, simply using the first law of thermodynamics. We can then rewrite eqn. 1.73 for work as

$$G_W(u,t) = \mathrm{Tr}\Big\{e^{-iu\hat{H}_S(t)/2}\, e^{iu\hat{H}_B/2}U(t,t_0)e^{iu\hat{H}_S(0)/2}e^{-iu\hat{H}_B/2}\hat{\rho}(0) \times\, e^{-iu\hat{H}_B/2}e^{iu\hat{H}_S(0)/2}U^\dagger(t,t_0)e^{iu\hat{H}_B/2}e^{-iu\hat{H}_S(t)/2}\Big\} \tag{1.77}$$

$$G_W(u,t) = \mathrm{Tr}\Big\{e^{-iu\hat{H}_S(t)}e^{iu\hat{H}_B/2}U(t,t_0)e^{-iu\hat{H}_B/2}e^{iu\hat{H}_S(0)}\hat{\rho}(0)e^{-iu\hat{H}_B/2}U^\dagger(t,t_0)e^{iu\hat{H}_B/2}\Big\} \tag{1.78}$$

as in [101], where u in this instance is now the Fourier conjugate variable to work and not heat, and where we have made the assumption that $\left[\hat{H}_S, \hat{\rho}(0)\right] = 0$. The characteristic function for work can be written more compactly as

$$G_W(u,t) = \mathrm{Tr}\left\{e^{-iu\hat{H}_S(t)}\hat{\rho}^u(t)\right\} \tag{1.79}$$

$$\hat{\rho}^u(t) = \hat{U}_{u/2}(t,t_0)e^{iu\hat{H}_s(0)}\hat{\rho}(0)\hat{U}^\dagger_{-u/2}. \tag{1.80}$$

To apply the method of FCS to an open quantum system, we simply follow steps outlined in section 1.2.2, for the modified counting field density matrix $\hat{\rho}^u(t)$. We will derive such a master equation explicitly in the results, for the case of a laser driven exciton coupled to a phonon reservoir.

1.3 Laser cooling of solids

1.3.1 History of laser cooling of solids

Laser cooling of gasses was a pivotal achievement in the late 70s that paved the way for many of the landmark quantum physics breakthroughs of the last 50 years. Demonstrated in 1978, when David Wineland and colleagues cooled ions to 40 K [104], rapid progress over the following ten years lead to laser cooling of neutral atoms to 2 μK [105]. The concept of using light to cool solids was proposed nearly 100 years ago, in 1929, by Pringsheim [106]. This proposal was based on the observation that some materials emitted light at shorter wavelengths than with which they were illuminated with, a process that was dubbed anti-Stokes fluorescence. While Stokes fluorescence refers to the emission of light by a material which has a shorter wavelength than which it was illuminated with, with the excess energy dumped into the phonon modes of the material, anti-Stokes fluorescence then involves the removal of energy from the phonon modes of the material. These processes are mediated by the interaction between the optically active electronic degrees of freedom and the phonon modes of the material. Such a laser cooling protocol is typically realised in rare-earth (RE) doped glasses and has been explored in semiconductors.

Fig. 1.12 shows a schematic of the basic cooling mechanism for both RE doped glasses and semiconductors. In the case of RE doped glasses, the lowest energy optically active transition, typically from the top of a ground state manifold to the bottom of an excited state manifold, is pumped with a laser. Fast thermalisation with the lattice leads to a thermal population in the higher lying states in the excited manifold. Spontaneous emission returns the system to the bottom of the ground state manifold, where again thermalisation with the lattice results in a population of the higher lying ground state manifold levels. The heat absorption is entirely due to this thermalisation of the cold population distributions of the levels within each manifold. Similarly, in the semiconductor model, the system is pumped at the band gap energy, where a cold distribution of carriers is generated. Interactions with the phonon modes result in thermalisation of these excited charge carriers, such that their distribution in the conduction band is that of a Fermi-Dirac distribution at a temperature equal to that of the lattice temperature. These carriers then recombine, emitting photons, which carry away the excess energy.

This process of anti-Stokes cooling was somewhat controversial, with claims that excitation and subsequent fluorescence was a reversible cycle, and thus any energy yield greater than unity would be a complete transformation of heat into work [107, 108]. These controversies were only laid to rest when Landau eventually developed a thermodynamic theory to describe the entropy of the input beam and fluorescent light, which proved that the fluorescence carried much higher entropy than the pump laser

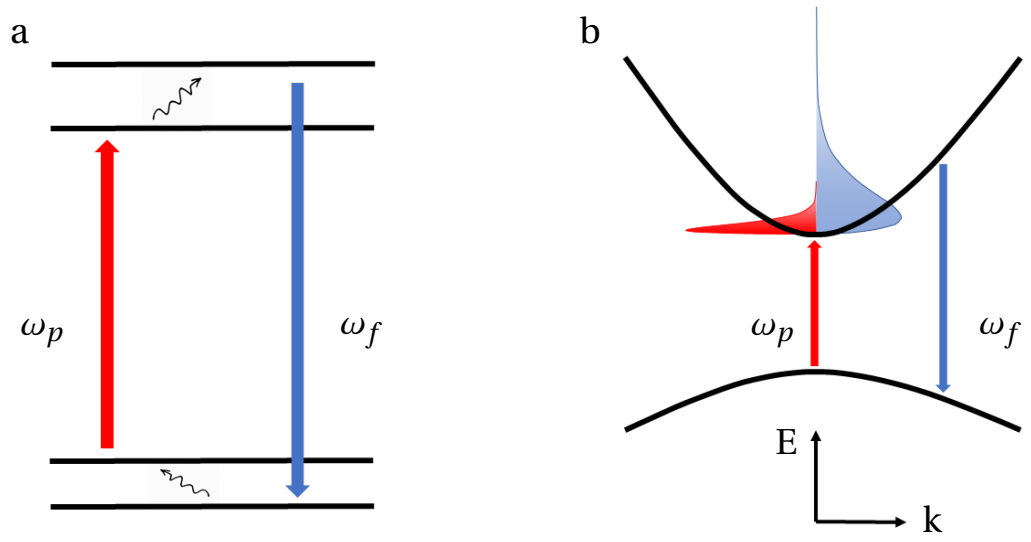

Figure 1.12: Laser cooling scheme for (a) RE doped glasses and (b) semiconductors. Wavy black arrows indicate phonon absorption processes.

beam, and that the process was irreversible [109]. We note here that this description of laser cooling is essentially the reverse of the model of the maser as a heat engine. In the maser, incoherent energy from a thermal bath was used to generate a coherent work output.

As early as 1950, RE doped solids were suggested to be used as the medium for anti-Stokes based optical refrigeration [110]. The advantage of these materials was the shielding of the optically active 4f electrons by the filled 5s and 5p outer shells. This shielding limited the electron-phonon interaction, thus suppressing nonradiative decay. It wasn't until 1995 that laser cooling of RE doped glasses was achieved [111], when ytterbium-doped fluorozirconate was cooled 0.4 K below room temperature. Over the following twenty years, the field progressed more slowly than laser cooling of gasses, with the cooling record of 91 K achieved in 2015 with Yb doped $YLiF_4$ [112]. It is accepted that RE doped glasses ultimately have a minimum cooling temperature of 50-100 K [113, 114]. Once the temperature of the medium reaches of order $k_B T = \Delta E$, with ΔE the width of the ground state manifold, the cooling drops off rapidly due to a thermal depletion of the population at the top of the manifold.

This limitation on the minimum cooling temperature does not exist in semiconductors, with theoretical predictions of cooling to temperatures as low as 10 K in bulk GaAs [115, 116]. Electrons and holes obey Fermi-Dirac statistics, which results in a full valence band at temperatures below the band gap, in contrast to the thermal depletion of the higher lying ground state levels we saw in the case of RE doped glasses. Although the density of electrons (holes) can be much higher in semiconductors than the density of RE dopants in glasses, many body processes restrict the densities which will lead

to cooling [117], to those of moderately doped glasses. Despite this limitation in the density of carriers, the net cooling power in semiconductors can still be up to 6 orders of magnitude higher due to the increased radiative recombination rates [118]. In 2013, laser cooling of CdS nanobelts to 250 K was reported. The validity of this report has since been questioned, however, and laser cooling in semiconductors remains an elusive goal [113]. The limitations of semiconducting media come from the need for almost perfect materials, to minimise non-radiative relaxation. Moreover, the high refractive index of semiconductors results in total internal reflection of the light, which may result in re-absorption of the emitted phonons [117].

1.3.2 Four Level Model of Laser Cooling of Solids

Laser cooling of RE-doped solids can be modelled using an effective 4 level structure. Although simple, this model captures the relevant physics, through a simple rate equation approach, describing resonant pumping of the RE dopants. As mentioned above, the RE doped systems are typically composed of a ground state manifold and an excited state manifold of levels. Fig. 1.13 provides a schematic of this cooling scheme, with the excited state manifold split by an energy gap E_e and the levels in the ground state manifold split by an energy E_g.

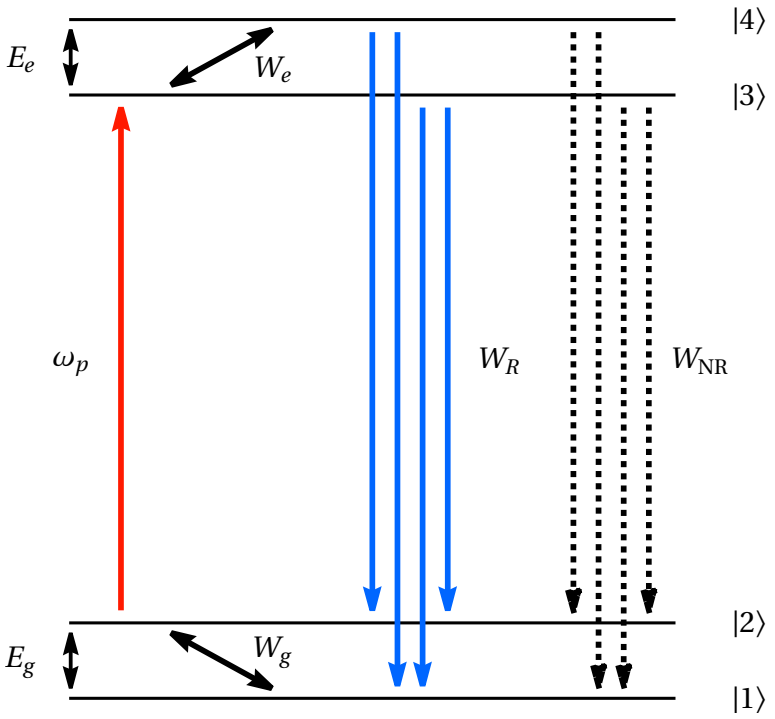

Figure 1.13: Schematic of the four level model of laser cooling RE doped glasses.

For laser cooling, we drive the $|2\rangle \rightarrow |3\rangle$ transition resonantly. This driving acts to equalise the populations in states $|2\rangle$ and $|3\rangle$. Spontaneous emission acts to take the populations from the excited state manifold to the ground state manifold. We refer to

these as radiative relaxation transitions, which proceed with a rate W_R. For simplicity, we assume that all of the radiative relaxation rates are the same. There are also non-radiative relaxation processes that take the populations in the excited states back to the ground state levels. These non-radiative transition occur with a rate W_{NR}, which we also assume to be equal, for simplicity. Lastly, there are thermalisation processes within each manifold, which act to bring the populations within a manifold to a Boltzmann distribution at a temperature equal to the lattice temperature. These arise from the electron-phonon interaction in the medium. These thermalisation processes occur with rates W_g and W_e, for the ground and excited states, respectively.

Using a rate equation model, we can write a set of coupled differential equations for the populations of the four levels. This type of model has been considered by many authors [114, 117, 119, 120]. Here we repeat this derivation, writing the set of coupled differential equations for the populations of each of the four levels,

$$\frac{dN_2}{dt} = -\sigma\left(N_2 - N_3\right)\frac{I}{\omega_p} + \left(N_3 + N_4\right)\left(W_R + W_{NR}\right) + \left(e^{-E_g/k_BT}N_1 - N_2\right)W_g, \quad (1.81)$$

$$\frac{dN_3}{dt} = \sigma\left(N_2 - N_3\right)\frac{I}{\omega_p} - 2N_3\left(W_R + W_{NR}\right) + \left(N_4 - e^{-E_e/k_BT}N3\right)W_e, \quad (1.82)$$

$$\frac{dN_4}{dt} = -2N_4\left(W_R + W_{NR}\right) - \left(N_4 - e^{-E_e/k_BT}N_3\right)W_e, \quad (1.83)$$

$$N = N_1 + N_2 + N_3 + N_4. \quad (1.84)$$

We have set $\hbar = 1$ and assume that the degeneracy of all the levels is 1. We can write down the difference between the absorbed power and the emitted power, which we denote P_{Net},

$$P_{\text{Net}} = \left[\sigma N_2 + \alpha_b\right] I - \left\{\left[\left(N_3 + N_4\right)\left(2\omega_p + \delta E_g\right) + 2N_4\delta E_{\text{e}}\right] W_R + \sigma N_3 I\right\}. \quad (1.85)$$

We have introduced α_b, the parasitic background absorption of the pump laser, which heats the solid. Taking the steady state limit, this can be expressed more succinctly as

$$P_{\text{Net}} = \left(\alpha_{\text{res}} + \alpha_b\right) I - \alpha_{\text{res}}\eta_q\frac{\nu_f}{\omega_p}I, \quad (1.86)$$

where we have ignored saturation. α_{res} is the ground state absorption, η_q the quantum efficiency and ω_f the mean fluorescence energy, defined as

$$\alpha_{\text{res}} = \frac{\sigma N}{1 + e^{E_g/k_BT}}, \quad (1.87)$$

$$h\omega_f = \omega + \frac{E_g}{2} + \frac{E_e}{1 + \left(\frac{2(W_R+W_{NR})}{W_e} + 1\right)e^{\frac{E_e}{k_BT}}}, \quad (1.88)$$

$$\eta_q = \frac{W_R}{W_R + W_{NR}}. \quad (1.89)$$

Dividing the net power by the total absorbed power, $P_{\text{abs}} = (\alpha_{\text{res}} + \alpha_b)\, I$, results in an expression for the cooling, efficiency

$$\eta_C = \eta_{\text{q}} \eta_{\text{abs}} \frac{\omega_f}{\omega} - 1. \tag{1.90}$$

This four level model allows us to understand the temperature dependence of the cooling. We can see from eqn. 1.87 the absorption quickly decreases as $k_B T < E_g$. In order to cool to lower temperatures, a narrow ground state manifold splitting is needed. The mean fluorescence energy also decreases as the temperature is lowered, reducing the cooling rate. This is a result of the decreasing thermal population of the upper level excited state as the temperature decreases. Moreover, if the electron-phonon interaction rate is smaller than the spontaneous emission rate, this redshift of the emitted photons is enhanced. Electron phonon thermalisation cannot occur, and all spontaneous emission is due to cold electrons. In fact, this cold electron recombination is also a problem for semiconductors at low temperatures, where carriers primarily interact with the low energy slow phonon modes [116].

1.4 Outline of the Thesis

In this thesis, we will explore the thermodynamics of heat exchanges in laser driven solid state systems. Specifically, we examine how the formation of strong-field dressed states allows a solid state emitter to absorb or emit acoustic phonons in a controlled way. We investigate how the form of the driving field can be tailored to produce different thermodynamic processes, including both reversible and irreversible heat absorption. This leads to an understanding of the origin of reversibility for time dependent laser controlled heat transfer. We discuss these effects from the perspective of quantum thermodynamics and outline the possibility of using them for optical cooling of solids to low temperatures, proposing a laser cooling protocol that makes active use of strong coherent driving.

In chapter 2 we introduce the laser driven quantum dot exciton-phonon model. We write the Hamiltonian for a quantum dot exciton, driven by a linearly chirped Gaussian laser pulse, including the interactions with the phonons of the surrounding medium. We derive both a secularised Bloch-Redfield master equation for this system and the corresponding counting field master equation, which we use to calculate the full counting statistics of the heat absorption. We investigate the dependence of the heat absorbed as a function of the laser parameters and introduce a toy model to calculate the efficiency of these heat transfers. We explain the results through the introduction of effective temperatures to describe the excitonic degrees of freedom. Finally, we present the probability distribution of the heat exchanged between the exciton and the phonons, and the probability distribution of the work done on the exciton.

In chapter 3 we extend the model of a heat engine composed of a laser driven exciton coupled to phonons to include more complex temporal profiles for the frequency of laser, beyond that of simple linear chirping. We use numerical optimisation methods to maximise the efficiency with respect to the temporal profile of the driving laser frequency.

In chapter 4 we present a steady state heat pumping model based on the same driven quantum dot-phonon model. We include the effects of spontaneous emission of photons by the exciton, and derive the Bloch-Redfield master equation and counting field master equation for the system with the added exciton-photon interaction terms in the Hamiltonian. We derive analytical expressions for the heat pump power, as a function of the laser parameters, and use full counting statistics methods to calculate the full probability distribution of the number of excitations transferred between the exciton and each bath.

In chapter 5 we extend the quantum dot heat pumping model to treat heat pumping of phonons using steady state laser driving of silicon vacancy centres in diamond, and propose a laser cooling protocol which is not impeded by the background heating

effects of the driving laser. We calculate the cooling power as a function of the laser parameters, and examine the effects of the strong coherent driving, in comparison to the weak driving regime, as is conventionally considered in laser cooling protocols. Finally, we compare the cooling spectra from a secular, non-secular and phenomenological Lindblad model, and identify regimes where each theory is appropriate.

Part I

Quantum Controlled Heat Absorption

2 Reversible Heat Transfer in Laser Controlled Excitons

In sections 1.1.2 and 1.1.6 we introduced the concept of adiabatic rapid passage in quantum control experiments on quantum dots. Specifically, we considered the effect of the phonons during the ARP state preparation protocol. The net effect was to limit the effectiveness, reducing the probability of preparing the exciton state of the quantum dot. We can view the exciton-phonon interactions during the ARP pulse as a driven system exchanging heat with a bath. In the case of CW laser driving, this problem was examined by Gauger and Wabnig [121], in their treatment of a laser driven exciton as a heat pump. They found that by using a red detuned laser, it was possible to continuously extract heat from the phonon reservoir, and use spontaneous emission of light from the exciton to discard the excess energy extracted from the lattice.

In this chapter, we extend this treatment to the case of chirped laser pulses. We consider the flow of heat between the exciton and phonons, under the action of an ARP laser pulse driving the exciton. Using a time-dependent field allows for the control of the temporal structure of the dressed state splitting, and thus control over the instantaneous exciton-phonon scattering rates. Such control will, in principle, allow for the design of a quantum thermal machine, where the excitonic degrees of freedom play the role of the working fluid, and the phonon reservoir plays the role of a thermal reservoir.

Such a treatment will require the use of quantum master equation techniques, to write down the equations of motion of the laser driven exciton under the influence of its interaction with the phonons. We follow the procedure outlined in [122] and derive a secular Bloch-Redfield master equation of Lindblad form, which enables us to numerically solve for the dynamics of the exciton. In order to compute the thermodynamic properties of the system, we follow the steps outlined in [100, 101] to write down the equivalent counting field master equation for this problem. With these tools, we can solve for the dynamics of the heat and work probability distributions.

2.1 Theoretical Methods

2.1.1 Model of Exciton-Laser-Phonon Interaction

We begin by deriving the Bloch Redfield master equation, which captures the dynamics of the laser driven exciton-phonon problem. In the absence of a driving laser, the Hamiltonian of the quantum dot is simply given by

$$\hat{H}_0 = E_g \hat{s}_z, \tag{2.1}$$

with E_g denoting the energy gap between the 0 and 1 exciton states. Here we have used the pseudo spin 1/2 operators defined as $\hat{s}_z = \frac{1}{2}\left(|1\rangle\langle 1| - |0\rangle\langle 0|\right)$ to simplify the notation, and introduce $\hat{s}^+ = |1\rangle\langle 0|$.

To include the interaction between the exciton and driving laser field, we add a dipole coupling term, $\hat{H}_{\text{drive}} = -\hat{\vec{d}} \cdot \vec{E}(t)$. For a laser with a time-dependent frequency and amplitude, the electric field has the form

$$\vec{E}(t) = \vec{e} E_0(t) \cos\left(\int^t \omega(\tau) d\tau\right), \tag{2.2}$$

with $\omega(\tau)$ the time-dependent frequency of the laser. Inserting this electric field into the driving Hamiltonian, we have

$$\begin{aligned}
\hat{H}_{\text{drive}} &= -\left(\langle 0|\, \hat{\vec{d}} \cdot \vec{e}\, |1\rangle\, |0\rangle\langle 1| + \text{h.c.}\right) \times \frac{E_0(t)}{2}\left[e^{i\int^t \omega(\tau)d\tau} + e^{-i\int^t \omega(\tau)d\tau}\right] \\
&= -\frac{\Omega(t)}{2}\left(|0\rangle\langle 1| + |1\rangle\langle 0|\right) \times \left[e^{i\int^t \omega(\tau)d\tau} + e^{-i\int^t \omega(\tau)d\tau}\right],
\end{aligned} \tag{2.3}$$

with $\Omega(t) = E_0(t)\langle 0|\, \hat{\vec{d}} \cdot \vec{e}\, |1\rangle$. Moving to the interaction picture, operators will have a time-dependence governed by

$$i\frac{d}{dt}O = \left[O, \hat{H}_0\right]. \tag{2.4}$$

For the Schrödinger picture operator $\hat{s}^- = |0\rangle\langle 1|$, we have its interaction picture counterpart $\tilde{s}^-(t)$, which is governed by

$$i\frac{d}{dt}\tilde{s}^-(t) = \left[\tilde{s}^-(t), \hat{H}_0\right] \tag{2.5}$$

$$= E_g \tilde{s}^-(t). \tag{2.6}$$

We then have that $\tilde{\hat{s}}^-(t) = e^{-iE_g t}\hat{s}^-$. Writing the driving Hamiltonian in the interaction picture, we have,

$$\hat{H}_{\text{drive}} = -\frac{\Omega(t)}{2}\left[|0\rangle\langle 1|\, e^{+i\int^t(\omega(\tau)-E_g)d\tau} + \text{h.c.}\right], \tag{2.7}$$

where we have ignored terms which have factors $e^{\pm i\int^t(\omega(\tau)+E_g)}$. This amounts to neglecting fast oscillating terms, and is known as the rotating wave approximation [17]. Undoing the interaction picture transformation, the driving Hamiltonian in the Schrödinger picture then becomes

$$\hat{H}_{\text{drive}} = -\frac{\Omega(t)}{2}\left[|0\rangle\langle 1|\, e^{+i\int^t\omega(\tau)d\tau} + \text{h.c.}\right]. \tag{2.8}$$

We perform one last transformation to a rotating frame, which helps remove the time-dependence from the exponential terms. This transformation amounts to re-defining the zero of energy. We use a unitary operator $\hat{U} = e^{+i\phi(t)s_z}$, where $\phi(t) = \int^t\omega(\tau)d\tau$. States and operators in this new frame can be expressed as

$$\left|\tilde{\psi}\right\rangle = hatU\,|\psi\rangle\,, \tag{2.9}$$

$$\tilde{O} = \hat{U}\hat{O}\hat{U}^\dagger, \tag{2.10}$$

where the tilde now signifies states and operators in the rotating frame, not the interaction picture as above.

Taking the derivative with respect to time, we have $i\frac{d}{dt}\tilde{O} = \omega(t)\left[\tilde{O}, s_z\right]$. For the Hamiltonian, we have

$$\tilde{H} \to \hat{U}H\hat{U}^\dagger + i\dot{\hat{U}}\hat{U}^\dagger, \tag{2.11}$$

$$= \hat{U}H\hat{U}^\dagger - \omega(t)s_z. \tag{2.12}$$

Finally, we can write the Hamiltonian for the exciton driven by a laser field with a time-dependent amplitude and time-dependent frequency as

$$H = \Delta(t)\hat{s}_z - \Omega(t)\hat{s}_x, \tag{2.13}$$

where $\Delta(t) = E_g - \omega(t)$. For brevity, we have dropped the tilde, and for the remainder of the chapter we will work in this rotating frame.

As in the introduction, we introduce the eigenstates of the Hamiltonian of the system as $|+\rangle$ and $|-\rangle$, the laser dressed states, with eigenvalues $\pm\Lambda(t)/2$, where $\Lambda(t) = \sqrt{\Delta(t)^2+\Omega(t)^2}$. These dressed states, expanded in the basis of the original states $|0\rangle$ and $|1\rangle$, are

$$|-\rangle = \sqrt{\left(\frac{\Lambda(t)-\Delta(t)}{2\Lambda(t)}\right)}|0\rangle + \sqrt{\left(\frac{\Lambda(t)+\Delta(t)}{2\Lambda(t)}\right)}|1\rangle\,, \tag{2.14}$$

$$|+\rangle = -\sqrt{\left(\frac{\Lambda(t)+\Delta(t)}{2\Lambda(t)}\right)}|0\rangle + \sqrt{\left(\frac{\Lambda(t)-\Delta(t)}{2\Lambda(t)}\right)}|1\rangle\,.$$

In this dressed state basis, we define new pseudo-spin operators, defined as

$$\begin{aligned} R_z &= \frac{1}{2}\left(|+\rangle\langle+| - |-\rangle\langle-|\right), \\ R_+ &= |+\rangle\langle-|. \end{aligned} \tag{2.15}$$

We can view these new spin operators, $\hat{\vec{R}}$, as generated from the original spin operators, $\hat{\vec{S}}$, by a rotation about the y-axis by an angle $\theta = \arctan\left(\Omega(t)/\Delta(t)\right)$. This angle is time-dependent due to the time-dependence of the frequency and amplitude of the driving laser. This rotation can be expressed as

$$\vec{R} = \begin{pmatrix} \cos\theta & 0 & \sin\theta \\ 0 & 1 & 0 \\ -\sin\theta & 0 & \cos\theta \end{pmatrix} \vec{S} = \begin{pmatrix} \Delta/\Lambda & 0 & \Omega/\Lambda \\ 0 & 1 & 0 \\ -\Omega/\Lambda & 0 & \Delta/\Lambda \end{pmatrix} \vec{S}.$$

The original pseudo spin operators can be expanded into this new rotated basis as

$$\begin{aligned} s_z &= \frac{\Delta}{\Lambda}R_z + \frac{\Omega}{2\Lambda}\left(R_+ + R_-\right), \\ s^+ &= \frac{\Omega}{\Lambda}R_z + \left(\frac{\Delta+\Lambda}{2\Lambda}\right)R_+ + \left(\frac{\Delta-\Lambda}{2\Lambda}\right)R_-, \\ s^- &= \frac{\Omega}{\Lambda}R_z + \left(\frac{\Delta-\Lambda}{2\Lambda}\right)R_+ + \left(\frac{\Delta+\Lambda}{2\Lambda}\right)R_-. \end{aligned} \tag{2.16}$$

The Hamiltonian of the exciton can then be expressed compactly as

$$\hat{H}_S(t) = \Lambda(t)\hat{R}_z. \tag{2.17}$$

The exciton interacts with the longitudinal acoustic phonons of the host medium, which can be accurately modelled by a deformation potential coupling [14]. This coupling can be qualitatively viewed as a shift in the position of the harmonic potential of the oscillators, $H_I = g\hat{s}_z \otimes \hat{x}$, with the direction of the shift depending on the state of the QD, where g is the coupling constant of the interaction. Adding in both the free phonon Hamiltonian and the phonon-exciton deformation potential interaction term, we have the full Hamiltonian for the system and bath,

$$\hat{H} = \Delta(t)\hat{s}_z - \Omega(t)\hat{s}_x + \sum_k \omega_k \hat{b}_k^\dagger \hat{b}_k + \hat{s}_z \otimes \sum_k (g_k \hat{b}_k + g_k^* \hat{b}_k^\dagger). \tag{2.18}$$

This Hamiltonian is known as the spin-boson Hamiltonian, and is a quintessential model in the field of open quantum systems. In this exciton-phonon problem, the phonons play the role of the reservoir, whose dynamics are unimportant. As such, we can derive a Bloch Redfield master equation, which describes only the dynamics of the exciton, retaining the effects of the interaction with the phonons.

2.1.2 Bloch-Redfield Master equation

We can follow the steps in [122] and in the introduction, to derive the Bloch-Redfield master equation. We use eqn. 1.33 from the introduction as our starting point,

$$\frac{d}{dt}\tilde{\rho}(t) = -\int_{-\infty}^{t} dt' \mathrm{Tr}_B \left[\tilde{H}_I(t), \left[\tilde{H}_I(t'), \tilde{\rho}(t) \otimes \tilde{\rho}_B\right]\right], \tag{2.19}$$

where $\tilde{H}_I(t) = P(t)\Phi(t)$, is the exciton-phonon coupling Hamiltonian. The operators $P(t)$ and $\Phi(t)$ are the system and bath interaction operators, respectively, in the interaction picture, defined as

$$\begin{aligned}
P(t) &= e^{iH_S(t)t} s_z e^{-iH_S(t)t} \\
&= e^{i\Lambda(t)tR_z} \left[\frac{\Delta}{\Lambda} R_z + \frac{\Omega}{2\Lambda}\left(R_+ + R_-\right)\right] e^{-i\Lambda(t)tR_z} \\
&= \frac{\Delta}{\Lambda} R_z + \frac{\Omega}{2\Lambda}\left(R_+ e^{i\Lambda(t)t} + R_- e^{-i\Lambda(t)t}\right), \\
\Phi(t) &= e^{iH_B t} \sum_k \left(g_k \hat{b}_k + g_k^* \hat{b}_k^\dagger\right) e^{-iH_B t} \\
&= \sum_k \left(g_k \hat{b}_k e^{-i\omega_k t} + g_k^* \hat{b}_k^\dagger e^{i\omega_k t}\right).
\end{aligned} \tag{2.20}$$

The interaction picture transformation above is not generally valid when the Hamiltonian has an intrinsic time-dependence. A true interaction picture transformation is obtained via a time ordered exponential unitary operator, $U = \mathcal{T}\left(e^{-i\int^t \hat{H}_S(t')dt'}\right) \otimes e^{-iH_B t}$. We use a much simpler unitary operator, given simply by the exponentiated system Hamiltonian, $U = e^{-i\Lambda(t)\hat{R}_z t} e^{-iH_B t}$. Clearly this does not generate the correct dynamics for the system, however we only use this form of unitary operator to calculate the effect of the phonons on short time scales, $t_c \sim 1/\omega_c$, with ω_c the cut off frequency in the spectral density. The final master equation for the density matrix of the exciton will be obtained by undoing this transformation. The dissipative part of the dynamics should be well approximated in the limit that $t_c d\Delta(t)/dt, t_c d\Omega(t)/dt \ll \Lambda(t)$ [122], as is the case in this work. Expanding out the commutators in eqn. 2.19, we get

$$\begin{aligned}
\frac{d}{dt}\tilde{\rho}(t) = -\int d\omega J(\omega) \int^t dt' \big([\, P(t)P(t')\tilde{\rho}(t) - P(t')\tilde{\rho}(t)P(t)] \times \\
\left[(n(\omega)+1)\, e^{-i\omega(t-t')} + n(\omega) e^{+i\omega(t-t')}\right] + \\
[-P(t)\tilde{\rho}(t)P(t') + \tilde{\rho}(t)P(t')P(t)] \times \\
\left[(n(\omega)+1)\, e^{i\omega(t-t')} + n(\omega) e^{-i\omega(t-t')}\,]\right)
\end{aligned} \tag{2.21}$$

with $n(\omega)$, the Bose-Einstein occupation function and where we have replaced the summation over modes by an integration over ω with the spectral density function, $J(\omega)$.

We can simplify eqn. 2.21 to

$$\frac{d}{dt}\tilde{\rho}(t) = -\int d\omega J(\omega)\left(P(t)P_+(t)\tilde{\rho}(t) - P_+(t)\tilde{\rho}(t)P(t) - P(t)\tilde{\rho}(t)P_-(t) + \tilde{\rho}(t)P_-(t)P(t)\right)$$

with the operators $P_\pm$ obeying $P_-(t) = P_+^\dagger(t)$ and given by

$$\begin{aligned}
P_+(t) &= \int^t dt' P(t')\left[(n(\omega)+1)\,e^{-i\omega(t-t')} + n(\omega)e^{i\omega(t-t')}\right] \\
&= (n(\omega)+1)\left[\frac{\Delta}{\Lambda}\frac{R_z}{-\omega+0} + \frac{\Omega}{2\Lambda}\left(\frac{R_+e^{+i\Lambda(t)t}}{i\left(\omega+\Lambda(t)\right)+0} + \frac{R_-e^{-i\Lambda(t)t}}{i\left(\omega-\Lambda(t)\right)+0}\right)\right] \\
&+ n(\omega)\left[\frac{\Delta}{\Lambda}\frac{R_z}{-\omega+0} + \frac{\Omega}{2\Lambda}\left(\frac{R_+e^{+i\Lambda(t)t}}{i\left(-\omega+\Lambda(t)\right)+0} + \frac{R_-e^{-i\Lambda(t)t}}{i\left(-\omega-\Lambda(t)\right)+0}\right)\right]. \qquad (2.22)
\end{aligned}$$

It is possible to write $P_\pm(t)$ more succinctly as $P_+(t) = \Gamma_c R_z + \Gamma_a R_+ + \Gamma_b R_-$ with the coefficients Γ_α defined as

$$\begin{aligned}
\Gamma_a &= \frac{\Omega}{2\Lambda(t)}\int d\omega J(\omega)\left[\frac{n(\omega)+1}{i\left(\omega+\Lambda\right)+0} + \frac{n(\omega)}{i\left(-\omega+\Lambda\right)+0}\right]e^{+i\Lambda(t)t}, \\
\Gamma_b &= \frac{\Omega}{2\Lambda(t)}\int d\omega J(\omega)\left[\frac{n(\omega)+1}{i\left(\omega-\Lambda\right)+0} + \frac{n(\omega)}{i\left(-\omega-\Lambda\right)+0}\right]e^{-i\Lambda(t)t}, \\
\Gamma_c &= \frac{\Delta}{\Lambda(t)}\int d\omega J(\omega)\left[\frac{n(\omega)+1}{i\omega+0} + \frac{n(\omega)}{-i\omega+0}\right]. \qquad (2.23)
\end{aligned}$$

Using the identity $\lim_{\eta\to 0}\frac{1}{x\pm i\eta} = \mathrm{P}\left(\frac{1}{x}\right) \mp i\pi\delta(x)$, the integrals can be computed. Finally, we perform the secular approximation, discarding terms with fast oscillating coefficients, and transform back to the Schrödinger picture. We are left with the master equation for the dynamics of the driven quantum dot in contact with the phonon bath,

$$\begin{aligned}
\frac{d}{dt}\hat{\rho}(t) = &-\left[\gamma_a\left(\Omega(t),\Delta(t)\right)/2\right]\left(\left\{\hat{R}_-\hat{R}_+,\hat{\rho}(t)\right\}_+ - 2\hat{R}_+\hat{\rho}(t)\hat{R}_-\right) \qquad (2.24) \\
&-\left[\gamma_e\left(\Omega(t),\Delta(t)\right)/2\right]\left(\left\{\hat{R}_+\hat{R}_-,\hat{\rho}(t)\right\}_+ - 2\hat{R}_-\hat{\rho}(t)\hat{R}_+\right) \\
&- i\left[\hat{H}_s(t),\hat{\rho}(t)\right].
\end{aligned}$$

This is a time-dependent Bloch-Redfield master equation in Lindblad form, obtained from the secularized Born-Markov approximation in the interaction picture. A phononic Lamb shift has been omitted from this master equation, as its effects are negligible in the parameter regimes that we examine in this work [122]. The master equation explicitly shows the origin of the decay terms. Phonon absorption and emission events are accompanied by transitions between the two laser dressed states of the quantum

dot. The rates in the above equation are given by

$$\gamma_a = 2\left(\frac{\Omega(t)}{2\Lambda(t)}\right)^2 \pi J(\Lambda(t)) n(\Lambda(t)) \tag{2.25}$$

$$\gamma_e = 2\left(\frac{\Omega(t)}{2\Lambda(t)}\right)^2 \pi J(\Lambda(t)) \left[n(\Lambda(t)) + 1\right] \tag{2.26}$$

We have yet to specify a spectral density function. In general, the spectral density of the bath is given by $J(\omega) = \sum_q g_q \delta\left(\omega - \omega_q\right)$. For this work we take the model used in [123] for an GaAs/InGaAs quantum dot, $J(\omega) = \frac{A\hbar}{k_B \pi}\omega^3 e^{-\omega^2/\omega_c^2}$, with cutoff frequency $\hbar\omega_c = 2$ meV and $A = 11.2$ fs K^{-1}. We plot the spectral density in fig (2.1). The Markov approximation remains valid when the spectral density is relatively flat over the linewidth of the system, which is satisfied at the temperatures we consider in this work [122]. For the control field, as in [54, 122] we use a pulse of the form:

$$\Delta(t) = -\frac{a}{a^2 + \tau_0^4} t + \delta \tag{2.27}$$

$$\Omega(t) = \frac{\Theta_0}{\sqrt{2\pi\sqrt{a^2 + \tau_0^4}}} e^{-\frac{t^2\tau_0^2}{2\left(a^2+\tau_0^4\right)}}.$$

The parameters used to specify the pulse are the spectral chirp a, pulse area Θ_0, unchirped pulse duration τ_0 and the detuning between the central frequency of the laser and the exciton transition frequency δ.

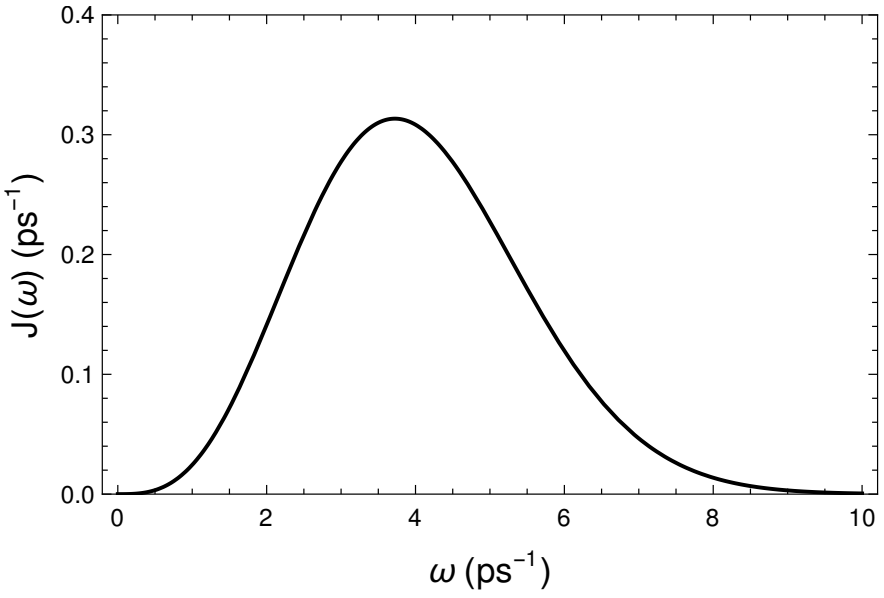

Figure 2.1: Spectral density for the exciton-phonon interaction in a GaAs/InGaAs quantum dot.

2.1.3 Counting Field Master Equation

To generate the probability distribution of the heat exchanges between the system and bath, along with the probability distribution for the work performed on the system via the control field, we must derive the counting field master equation. As we saw in the introduction, this involves introducing counting fields into the definition of both the density matrix and the evolution operators. We follow the procedure outlined in [100, 101].

In the interaction picture, the state of the full system plus bath, which we denote ρ, can be expressed through the use of interaction picture evolution operators U_I. We begin with the known equation for the total density matrix of the system plus bath in the interaction picture, $\tilde{\rho}$, which will be denoted simply as ρ from here onward,

$$\rho(t) = \hat{U}_I \hat{\rho}_0 \hat{U}_I^\dagger,$$

with U_I the interaction picture evolution operator. We then introduce the counting fields to $\hat{U}_I$, as described in section 1.2.2, and arrive at

$$\hat{\rho}^u(t) = \hat{U}_{I,u/2}(t,t_0)\hat{\rho}^u(0)\hat{U}^\dagger_{I,-u/2}(t,t_0) \tag{2.28}$$

$$\hat{U}_{I,u/2}(t,t_0) = e^{iu\hat{H}_B}\hat{U}_I(t,t_0)e^{-iu\hat{H}_B}, \tag{2.29}$$

for the counting field evolution operator and the counting field density matrix.

We take the time derivative of both sides of eqn. 2.28, and note that $i\dot{\hat{U}}_{I,u/2} = \hat{H}_c^{u/2}(t)\hat{U}_{I,u/2}$, where $\hat{H}_I(t)$ the interaction Hamiltonian coupling the exciton and phonons and is defined as $\hat{H}_I^u(t) = e^{iu\hat{H}_B}\hat{H}_I(t)e^{-iu\hat{H}_B}$. This results in

$$\frac{\partial}{\partial t}\rho^u(t) = -i\hat{H}_I^{u/2}(t)\rho^u(t) + i\rho^u(t)\hat{H}_I^{-u/2}(t),$$

which is the equivalent of the standard von-Neumann equation for the density matrix of the quantum dot system. Formally integrating the above equation, we substitute the result back into itself and take the trace over the degrees of the freedom of the bath, leaving

$$\begin{aligned}\frac{\partial}{\partial t}\rho_S^u(t) = \mathrm{Tr}_B\{ &-\int_{-\infty}^{t}\left(\hat{H}_I^{u/2}(t)\hat{H}_I^{u/2}(s)\rho_s^u(t)\otimes\rho_B - \hat{H}_I^{u/2}(t)\rho_s^u(t)\otimes\rho_B\hat{H}_I^{-u/2}(s)\right)\\ &+\int_{-\infty}^{t}\left(\hat{H}_I^{u/2}(s)\rho_s^u(t)\otimes\rho_B\hat{H}_I^{-u/2}(t) - \rho_s^u(t)\otimes\rho_B\hat{H}_I^{-u/2}(s)\hat{H}_I^{-u/2}(t)\right)\}\,,\end{aligned} \tag{2.30}$$

for the counting field density matrix of the exciton.

We repeat the derivation carried out in section 2.1.2, which includes the process of

secularisation to ensure positivity of the density matrix, and we obtain the counting field master equation for the state of the exciton in the Schrödinger picture

$$\begin{aligned}\frac{\partial}{\partial t}\hat{\rho}_S^u(t) = &- i\left[\hat{H}_s(t), \hat{\rho_S^u}(t)\right] \\ &- \gamma_e\left(\left\{\hat{R}_+\hat{R}_-, \hat{\rho}_S^u(t)\right\}_+ - 2e^{+iu\Lambda(t)}\hat{R}_-\hat{\rho}_S^u(t)\hat{R}_+\right) \\ &- \gamma_a\left(\left\{\hat{R}_-\hat{R}_+, \hat{\rho}_S^u(t)\right\}_+ - 2e^{-iu\Lambda(t)}\hat{R}_+\hat{\rho}_S^u(t)\hat{R}_-\right)\end{aligned} \tag{2.31}$$

where, once again, the Lamb shift term has been neglected.

The full counting statistics of the work and heat can be derived directly from the modified density matrix, $\hat{\rho}_s^u(t)$, through the characteristic functions, defined as

$$G_Q(t,u) = \mathrm{Tr}\hat{\rho}_S^u(t) \tag{2.32}$$

$$G_W(t,u) = \mathrm{Tr}e^{iuE_G|1\rangle\langle 1|}\hat{\rho}_S^u(t). \tag{2.33}$$

These characteristic functions, each have a different initial condition, $\hat{\rho}_S^u(-\infty) = \hat{\rho}_S(-\infty)\forall u$ and $\hat{\rho}_S^u(-\infty) = e^{-iuE_g|1\rangle\langle 1|}\hat{\rho}_S(-\infty)$, for the case of heat and work respectively [101]. Solving for the characteristic function numerically, we can get the full probability distributions for the heat and the work.

The role of the operators, $e^{\pm iuE_g|1\rangle\langle 1|}$, in the definition of the work distribution, is to carry out a two-point projective measurement. This amounts to measuring the quantum dot for the presence of exciton before and after the protocol, in essence measuring the total change in the energy of the system. This in essence computer the change work done on the exciton by the driving laser through the first law, subtracting the change in heat from the change in total energy.

Alternatively, we can compute the moments of the heat and work distributions directly from the characteristic functions. For the first moment of the heat distribution, the mean heat exchanged between system and bath, we have

$$\langle Q\rangle = \frac{1}{i}\frac{\partial G_Q(u,t_f)}{\partial u}\bigg|_{u=0} = \frac{1}{i}\frac{\partial}{\partial u}\mathrm{Tr}\left[\hat{\rho}(t,u)\right]\bigg|_{u=0} = \frac{1}{i}\frac{\partial}{\partial u}\mathrm{Tr}\left[\int_{-\infty}^{t}\hat{\hat{L}}^u\left[\hat{\rho}(t',u)\right]\right]dt'\bigg|_{u=0},$$

with $\hat{\hat{L}}^u$ the counting field Liouville superoperator which generates the dynamics of $\hat{\rho}(t,u)$ as in eqn. 2.31, $\partial\hat{\rho}(t,u)\partial t = \hat{\hat{L}}^u\hat{\rho}(t,u)$. Inserting in the Liouville superoperator,

we have

$$\langle Q\rangle = -\frac{1}{i}\mathrm{Tr}\int_{-\infty}^{t} dt'\gamma_a/2\left(\left\{\hat{R}_-\hat{R}_+,\frac{\hat{\rho}(t,u)}{\partial u}\right\} - 2e^{+iu\Lambda(t)}\hat{R}_+\frac{\partial\hat{\rho}(t,u)}{\partial u}\hat{R}_- \right.$$
$$\left. -i\Lambda(t)2e^{+iu\Lambda(t)}\hat{R}_+\hat{\rho}(t,u)\hat{R}_-\right)$$
$$\gamma_e/2\left(\left\{\hat{R}_+\hat{R}_-,\frac{\hat{\rho}(t,u)}{\partial u}\right\} - 2e^{-iu\Lambda(t)}\hat{R}_-\frac{\partial\hat{\rho}(t,u)}{\partial u}\hat{R}_+ \right.$$
$$\left. +i\Lambda(t)2e^{-iu\Lambda(t)}\hat{R}_-\hat{\rho}(t,u)\hat{R}_+\right)\Big|_{u=0}. \quad (2.34)$$

Terms with $\hat{R}_\pm\frac{\partial\hat{\rho}(t,u)}{\partial u}\hat{R}_\mp$ cancel and $\hat{\rho}(t,0)=\hat{\rho}(t)$,

$$\langle Q\rangle = \mathrm{Tr}\int_{-\infty}^{\infty} dt'\Lambda(t')\left(\gamma_a(t)\hat{R}_+\hat{\rho}(t)\hat{R}_- - \gamma_e(t)\hat{R}_-\hat{\rho}(t)\hat{R}_+\right), \quad (2.35)$$
$$= \int_{-\infty}^{\infty} dt'\Lambda(t')\left(\gamma_a(t)P_\downarrow(t) - \gamma_e(t)P_\uparrow(t)\right) \quad (2.36)$$

where we have used $\mathrm{Tr}\left[\hat{R}_\pm\hat{\rho}\hat{R}_\mp\right] = P_{\downarrow/\uparrow}$, with $P_{\downarrow/\uparrow}$ as the probability of being in the lower/upper dressed state respectively.

This result for the mean heat can also be found using the formula put forward by Alicki in 1979 [93]:

$$\dot{Q} = \mathrm{Tr}\left[\dot{\hat{\rho}}(t)\hat{H}_s(t)\right]. \quad (2.37)$$

The benefit of the full counting statistics approach comes in the calculation of higher order moments, beyond the mean, and in the ability to calculate of the full probability distribution.

Similarly, for the work, we follow the same procedure and recover the first law.

$$\langle W\rangle = \frac{1}{i}\frac{\partial G_Q(u,t_f)}{\partial u}\Big|_{u=0} = \frac{1}{i}\frac{\partial}{\partial u}\mathrm{Tr}\left[e^{iu\hat{H}_0}\hat{\rho}(t,u)\right]\Big|_{u=0} = \frac{1}{i}\frac{\partial}{\partial u}\mathrm{Tr}\left[\int_{-\infty}^{t} e^{iu\hat{H}_0}\hat{\hat{L}}^u\left[\hat{\rho}(t',u)\right]\right]dt'\Big|_{u=0}$$

$$\langle W\rangle = \left[\hat{H}_0,\hat{\rho}(t,0)\right] + \frac{1}{i}\,e^{iu\hat{H}_s}\frac{\partial}{\partial u}\int_{-\infty}^{t}\hat{\hat{L}}^u\left[\hat{\rho}(t',u)\right]\Big|_{u=0}$$

$$\langle W\rangle = \langle\hat{H}_0\rangle + \langle Q\rangle. \quad (2.38)$$

The expressions for the mean heat and work involve only $\hat{\rho}(t,0)$. We need to only solve the much simpler standard Bloch Redfield master equation (2.24) to calculate these quantities. A calculation of the full distributions involves numerically solving the counting field master equation (2.31).

2.2 Results

Before analysing the results of the heat flows between the system and environment, it is instructive to re-examine the dressed states of the exciton, and the effect of the sign of the chirp. The purple dotted line in fig. 2.2 depicts energy level structure of the dressed states over time, in the limit that the field of the driving laser goes to zero. This leads to dressed states which are, at all times, the bare $|0\rangle$ and $|1\rangle$ exciton basis sates. The dressed state splitting in this case is simply $\Lambda(t) = |\Delta(t)|$.

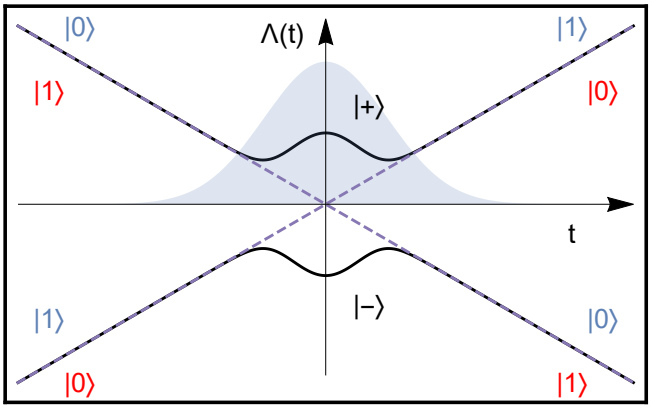

Figure 2.2: Generic dressed state splitting during an ARP driving sequence. The blue shaded region depicts the pulse amplitude. The states are the dressed state mappings before and after the pulse for positive spectral chirp. The states in blue denote the dressed state mappings before and after the pulse for the case of negative spectral chirp.

With a non-zero laser field amplitude, the degeneracy of the levels at the crossing is lifted and results in two distinct non degenerate dressed states, whose structure we wrote down in section 2.1.1. At early and late times, i.e., before and after the driving sequence, both of the dressed states each map exactly to one of the exciton basis states. This designation will depend on the sign of the chirp, as indicated in the figure. For positive spectral chirp, we have $|-\rangle_{t\to-\infty} = |0\rangle$ and $|-\rangle_{t\to+\infty} = |1\rangle$. In an isolated setting, the system would adiabatically evolve along $|-\rangle$ in time, effectively inverting the population from $|0\rangle$ to $|1\rangle$. Conversely, for negative spectral chirp, we have $|+\rangle_{t\to-\infty} = |0\rangle$ and $|+\rangle_{t\to+\infty} = |1\rangle$. Identical to the case of positive spectral chirp, the system would adiabatically evolve along the upper dressed state to effectively invert the population of the QD exciton to $|1\rangle$.

We know this inversion is limited in practice due to the interaction with the phonons. The emission and absorption of phonons into/from the bath prompts transitions between the dressed states. Taking a generic chirped Gaussian laser pulse with a central frequency resonant with the exciton transition frequency, the effect of the phonons is to reduce the final occupation from unity. For positive spectral chirp, if we measure the QD to start and end in 0, we know a transition from $|-\rangle$ to $|+\rangle$ must have taken place, which we associate with the absorption of a phonon. Likewise, for negative spec-

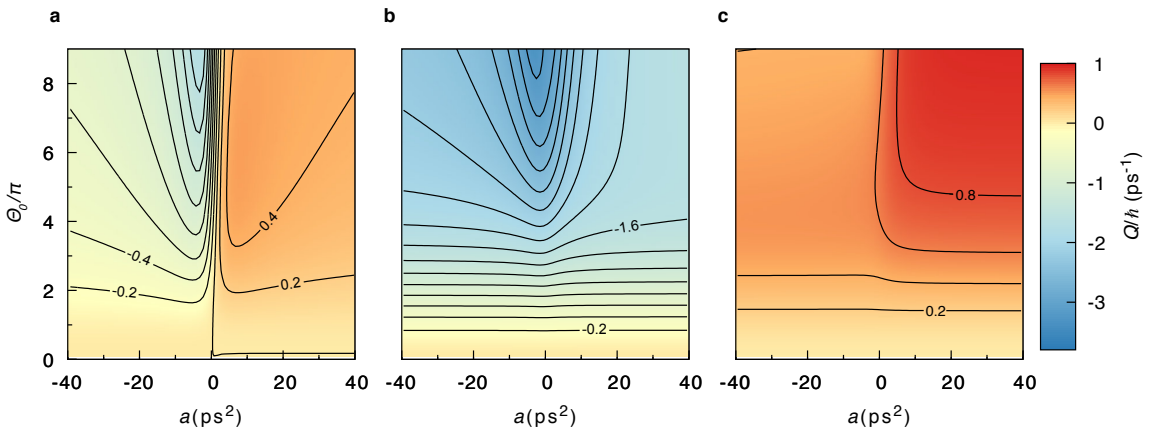

Figure 2.3: Exciton-phonon heat flow for laser-driven excitons. Predicted heat absorbed ($\hbar$/ps) by a quantum-dot exciton transition, initially in its ground state, driven by a chirped laser pulse with a given spectral chirp (horizontal axes) and pulse area (vertical axes). Results are shown for different detunings of the exciton from the pulse centre frequency, $\delta = \omega_x - \omega(t = 0)$: (a) 0 (b) -2.5 ps^{-1} (c) 2.5 ps^{-1}. The contour spacing is $0.2\hbar$/ps.

tral chirp, such a measurement would indicate that a phonon emission event has taken place. It is important to note that the energies of the emitted and absorbed phonons will depend on the time at which the transition occurs, due to the time-dependence of the splitting $\Lambda(t)$.

2.2.1 Mean Heat Abosrbed

Fig. 2.3 is a plot of the mean heat transferred from the phonon reservoir at $T = 20$ K, to exciton, for pulses with a range of values of spectral chirp a, pulse area Θ_0 and for different values of fixed detuning $\delta = E_X - \omega_0$. In panel (a) we have plotted the mean heat absorbed for a pulse with a central frequency resonant with the exciton transition. There is a net absorption of heat from the phononic environment for positive spectral chirp and emission of heat from the QD to the bath for negative values of the spectral chirp. Panel (b) is a plot of the heat absorption for a chirped Gaussian pulse with some negative fixed detuning, i.e. $E_g - \omega_l = \delta < 0$. Such pulses lead to an emission of heat into the phonon environment for all values of a and Θ considered. Positive fixed detuning δ, shown in panel (c), leads to net heat absorption for all pulse parameters in the range considered. The dependence of the direction of the heat flow on the sign of the spectral chirp is clear from our discussion of the dressed state structures above. The fact that the direction of heat flow also depends on the sign of the fixed detuning is not quite as apparent, and will become more obvious when we consider the effective temperature of the exciton later in this chapter.

2.2.2 Completing the Cycle

In principle, there are two possibilities of using this heat transfer as a stroke in a thermal machine. The first option is to simply build a chiller. The goal of such a machine would be to simply cool the environment to which it is coupled. To do this with our quantum dot system is trivial. We need only use spontaneous emission of photons to take the quantum dot back to $|0\rangle$ after each driving pulse. Neglecting background heating due to the driving laser, the cooling power would be limited by the emission lifetime of the dot, which is on the order of nanoseconds [124].

The second option is to use this heat transfer as the hot stroke of a heat engine. In order to close the cycle, we would need to add in a cold stroke. If we close this cycle with some ideal, generic and completely reversible cold stroke, then investigating the performance of the entire cycle would provide us with a way to investigate the reversibility of the hot stroke. Fig. 2.4 shows a schematic of the chiller and heat engine cycles. We will refer to these later in the chapter and discuss how we compute the temperature and entropy during the cycles.

To complete the cycle, we must specify a second thermal bath, which will play the role of the cold reservoir. For this cold stroke, we take a completely reversible heat transfer between system and cold bath, at a temperature T_C. Any deviations from the Carnot efficiency of this engine must then come exclusively from the hot stroke. In order to calculate such an efficiency, we must calculate the heat and work exchanges during each stroke. To do this, we calculate the changes in entropy of the system and bath.

$$\Delta S^{\mathrm{h}}_{\mathrm{sys}} = \frac{Q}{T_{\mathrm{h}}} + \Delta S_{\mathrm{irr}}$$

$$\Delta S^{\mathrm{h}}_{B_{\mathrm{h}}} = -\frac{Q}{T_{\mathrm{h}}}$$

To complete the thermodynamic cycle, the system must return to its initial state, implying the change in entropy of the system due to the cold stroke must be the negative of the change in entropy of the system due to the hot stroke and with a completely reversible cold stroke this also gives the change in entropy of the cold bath,

$$\Delta S^{\mathrm{c}}_{\mathrm{B_c}} = \Delta S^{\mathrm{h}}_{\mathrm{sys}}.$$

The total change in entropy during the entire cycle is given by

$$\Delta S = \Delta S_{\mathrm{irr}} = \Delta S^{\mathrm{h}}_{\mathrm{sys}} + \Delta S^{\mathrm{h}}_{\mathrm{B_h}} = -k_B \mathrm{Tr}\left[\hat{\rho}\log\hat{\rho}\right] - \frac{Q}{T_{\mathrm{h}}},$$

where we have computed the change in entropy of the system using the Von Neumann definition. From the first law of thermodynamics, the net work out of the system is simply given by the difference between the heat in and the heat out of the system,

$W_{\rm out} = Q_{\rm in} - Q_{\rm out}$, resulting in

$$\eta = \frac{-T_{\rm h}\Delta S^{\rm h}_{\rm B_h} + T_c\left(\Delta S_{\rm irr} - \Delta S^{\rm h}_{\rm B_h}\right)}{-T_{\rm h}\Delta S^{\rm h}_{\rm B_h}}, \tag{2.39}$$

for the efficiency of the entire cycle We are using the sign convention that Q is the heat exchanged during the hot stroke, transferred from hot bath to the quantum dot.

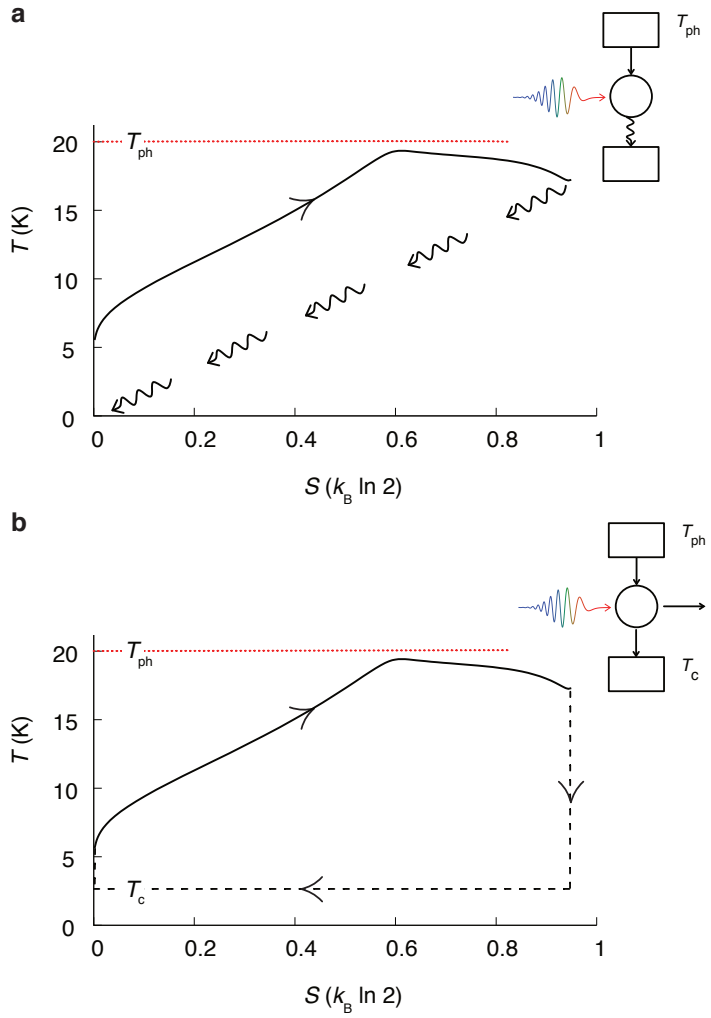

Figure 2.4: Heat engines and chillers. **a** The cycle for a quantum-dot chiller. The solid curve in the temperature-entropy plot shows these quantities for the quantum-dot as it is driven by a laser pulse and absorbs heat from the phonon bath. The temperature shown is defined by eqn. 2.40. The wavy lines depict the subsequent radiative decay, which returns the quantum dot to its ground state. The upper (lower) square box in the engine diagram represents the phonon (electromagnetic) environment, and the circle the quantum dot. **b** The cycle for a quantum-dot heat engine. This comprises the same heat-absorption stroke as the chiller, but the cycle is then closed by a partial Carnot cycle, which implements a reversible heat transfer to a bath at a temperature $T_c < T_{\rm ph}$

2.2.3 Efficiency

Fig. 2.5 shows the efficiencies for such cycles for a range of values of spectral chirp and pulse area, for two values of detuning, δ, and two values of unchirped pulse duration, τ, with the cold bath set at a temperature of $T_C = 2.7$ K and the phonon reservoir at $T = 20$ K. The efficiency is shown as a fraction of the Carnot efficiency, which in this case is $\eta_C = 1 - T_c/T_h = 0.87$. The efficiency for a resonant pulse, with $\tau_0 = 2$ ps, is shown in Panel (a). The peak efficiency here is about $0.61\eta_C$ at $a = 8.0\text{ps}^2$ and $\Theta_0 = 6.3\pi$. This efficiency is not close to the Carnot efficiency, but it is 80% of the Chambadl-Novikov efficiency, or the endoreversible efficiency at maximum power [125] which is also often referred to as the Curzon-Ahlborn efficiency. For these temperatures, this would be $\eta = 1 - \sqrt{T_c/T_h} = 0.73\eta_C$.

Panel (b) shows the effect of introducing positive detuning ($E - \omega_L = \delta > 0$), again, onto the longer ($\tau_0 = 2$ ps) pulse. Similar to the resonant case, as the chirp is increased from zero to finite positive values, the efficiency rapidly increases before approaching a limit. This behaviour is also seen in the heat absorption map fig. 2.3(c). This saturation can be attributed to the way the temporal chirp, $\alpha = d\Delta(t)/dt = a/\left(a^2 + \tau_0^4\right)$, and pulse duration $\tau = \tau_0^2 + a^2/\tau_0^2$, depend on the spectral chirp. For large a, the temporal chirp α decreases with a, while τ increases, such that the product $\alpha\tau$ asymptotes to $1/\tau_0$. We see non-zero efficiencies for most of the parameter space, negative chirp sector included. This is a consequence of the net heat absorption seen over the same parameter region, observed in the associated heat absorption map.

Panels (c) and (d) show the corresponding results for a smaller value of τ_0, i.e., a higher bandwidth driving pulse. This leads to higher efficiencies which, for the positively-detuned case shown in fig. 2.5(d), reach $0.95\eta_C$. This maximum is achieved at the upper boundary of the plot $\Theta_0 = 9\pi$, in the region of positive chirp $a \gtrsim 5$ ps^2. We conclude that such pulses lead to reversible exciton-phonon heat transfers.

The reversibility of the heat transfer process can also be quantified by the entropy generation. Fig. 2.6 shows the entropy of the exciton for two choices of pulse parameters, as a function of time. One of these, which we refer to as the Carnot pulse, corresponds to a point in fig. 2.5 (d) in the maximum efficiency region, $\Theta_0 = 9\pi$, a = 10 ps^2. The other, which we choose for comparison with the chirped case, is the point of maximum efficiency in fig. 2.5 (b) along the line of zero chirp ($\Theta_0 = 6.0\pi$, $\eta = 0.84\eta_C$, $Q/\hbar = 0.62\text{ps}^{-1}$). We also plot, as the dashed line, the corresponding entropy decrease of the phonon reservoir, Q/T_{ph}. The gap between the two curves is the overall entropy generation. These choices will show us the effects of including chirp into the driving protocol on the performance of the thermal machine. As one would expect from the difference in efficiencies, the entropy generation in the Carnot pulse is lower than that of the unchirped comparator. It is also evident that the chirped pulse exceeds the unchirped pulse in the heat absorbed per driving cycle.

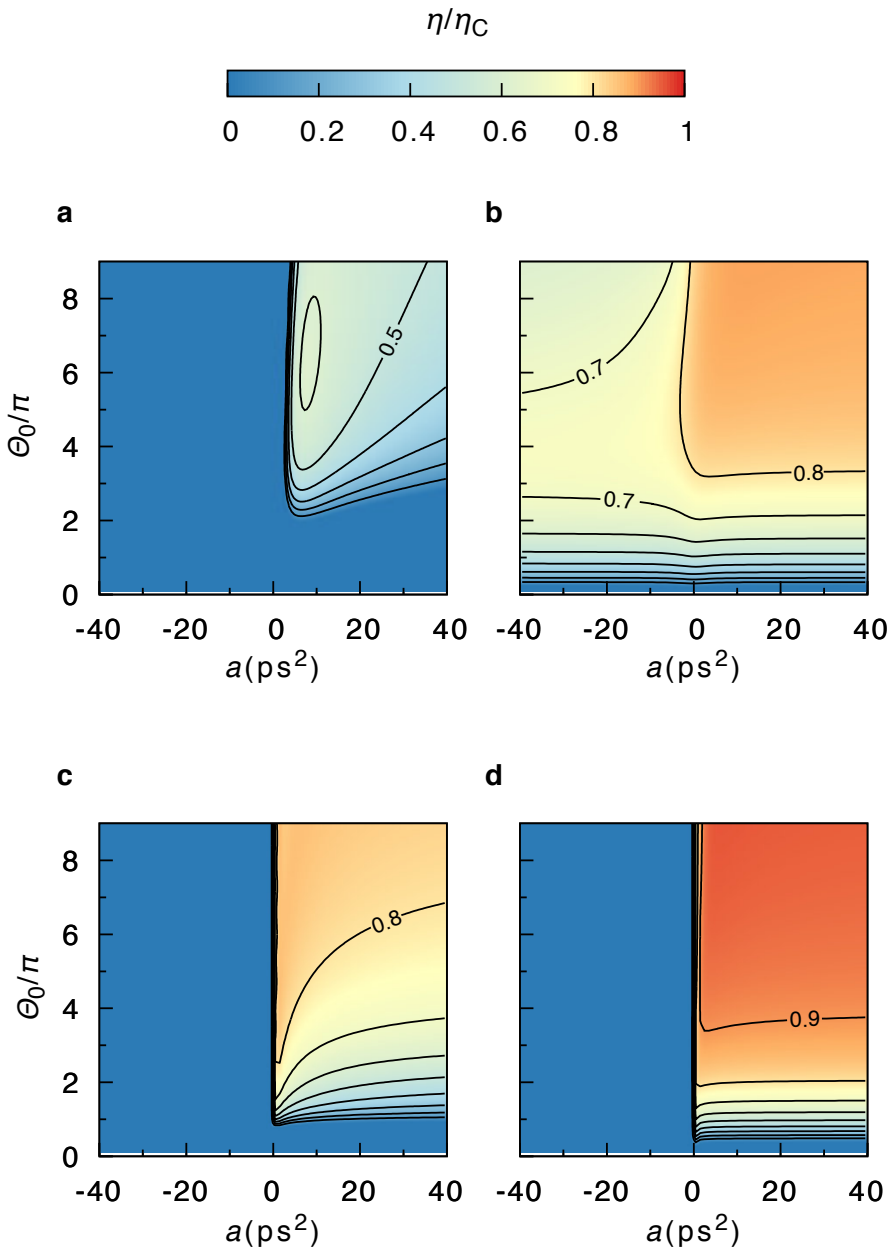

Figure 2.5: Efficiency as a fraction of the Carnot efficiency for an exciton heat engine. Results are shown as functions of the spectral chirp (a, horizontal axes) and the pulse area (Θ_0, vertical axes) of the driving pulse used for the heat absorption stroke. The panels correspond to different values of the detuning, δ, and unchirped pulse duration, τ_0. (a) 0 ps^{-1} and 2 ps, (b) +2.5 ps^{-1} and 2 ps, (c) 0 ps^{-1} and 0.5 ps, (d) 2.5 ps^{-1} and 0.5 ps.

2.2.4 Effective Temperature

To understand the reduced entropy production in the case of a chirped pulse relative to an unchirped pulse, we can examine the effective temperature of the quantum dot exciton as a function of time. Driven systems are by definition out of equilibrium and cannot be described by a Gibbs state of the form $\hat{\rho} = e^{-\beta \hat{H}}$, but in our model it is clear from the master equation that governs the time local dynamics of the system density matrix, that the interaction between the system and the bath tends to thermalise

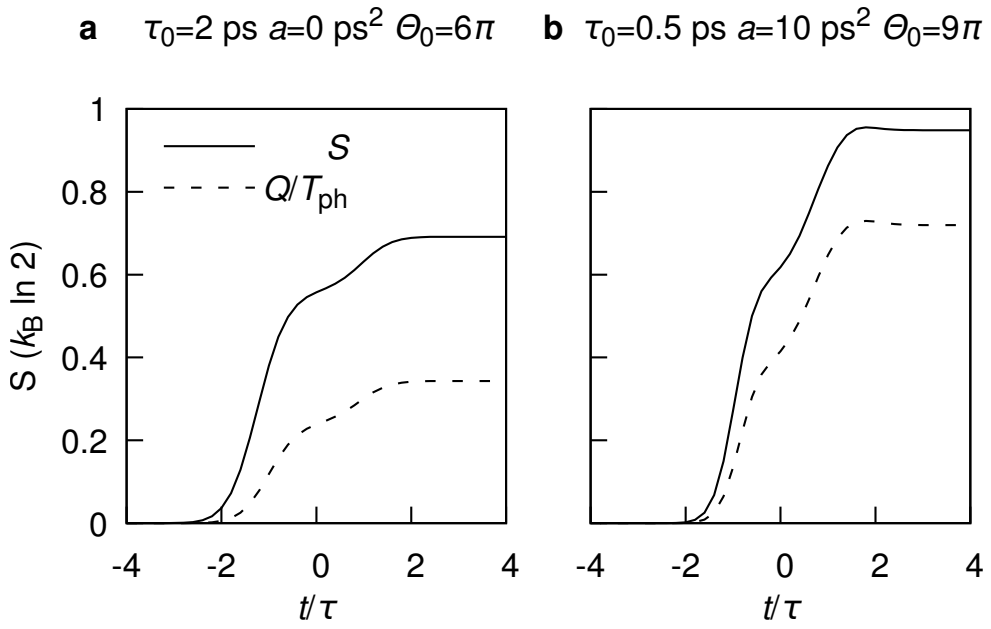

Figure 2.6: Entropy gained by the quantum dot (solid) and entropy lost by the phonon reservoir (dashed) as functions of time for two different driving pulses. **a** Unchirped pulse with $\delta = 2.5\text{ps}^{-1}$ and other parameters as indicated. **b** Chirped pulse with $\delta = 2.5\text{ps}^{-1}$ and other parameters as indicated. Time is given in units of the pulse duration, τ, in each case.

excitonic degrees of freedom in the basis of laser dressed states with the phonons; as in [47], where it was shown that a quantum dot driven by a constant laser field reaches a steady state well described a by a thermal occupation of the dot-laser dressed states. This is due to the transition rates in the master equation obeying the detailed balance relation $\gamma_a/\gamma_e = e^{-\hbar\Lambda/k_B T_h}$. This implies that the dressed state population, p_+ and p_- can be used to define a temperature of the QD, T_{eff}, which is defined by

$$\frac{p_+}{p_-} = e^{-\hbar\Lambda/k_B T_{\text{eff}}}. \tag{2.40}$$

Fig. 2.7a shows the temperature of the dot, as a function of time, for the chirped Carnot pulse and the unchirped comparator pulse. We also show, in fig. 2.7b, the corresponding heat absorption currents. For the unchirped pulse the temperature of the exciton, which varies during the pulse, is significantly different from that of the bath while the heat is flowing, leading to irreversible entropy generation. For the chirped Carnot pulse, however, there is an interval of time during which heat flows and the temperature of the dot is relatively constant. During this interval, any heat absorbed from the bath, is absorbed isothermally. Moreover, this isothermal heat absorption occurs when the temperature of the exciton is close to that of the bath, $T = 20$ K. This isothermal heat absorption at the bath temperature produces little entropy and is

quasi-reversible. This isothermal part of the heat absorption process can also be seen on the temperature-entropy plots in fig. 2.4, where the solid lines are results obtained for the chirped Carnot pulse.

It may be noted that the duration of the chirped Carnot pulse, $\tau = 20$ ps, is significantly greater than that of the unchirped comparator, $\tau = 2$ ps. However, we have calculated the maximum efficiency for an unchirped pulse of these two durations, and find in both cases the same value ($0.82\ \eta_C$). Thus, the increased duration associated with the chirping does not account for the change in efficiency.

The reversible isothermal part of the heat absorption process is made possible by the time-dependence of the dressed-state energies, which are shown for both pulses in fig. 2.7c. For the chirped Carnot pulse, the energy splitting is reducing during the heat transfer. This would, for an adiabatic process, reduce the temperature in line with eqn. 2.40. Here, it compensates for the increase in temperature that would be expected as heat flows from the phonons to the exciton. The result is an isothermal heat transfer, which can occur at the bath temperature and hence be reversible. An alternative view is in terms of the scattering rates: reducing the splitting increases the ratio between phonon absorption and emission, moving the detailed-balance equilibrium for the dressed-state populations, and driving a heat flow over a negligible temperature difference.

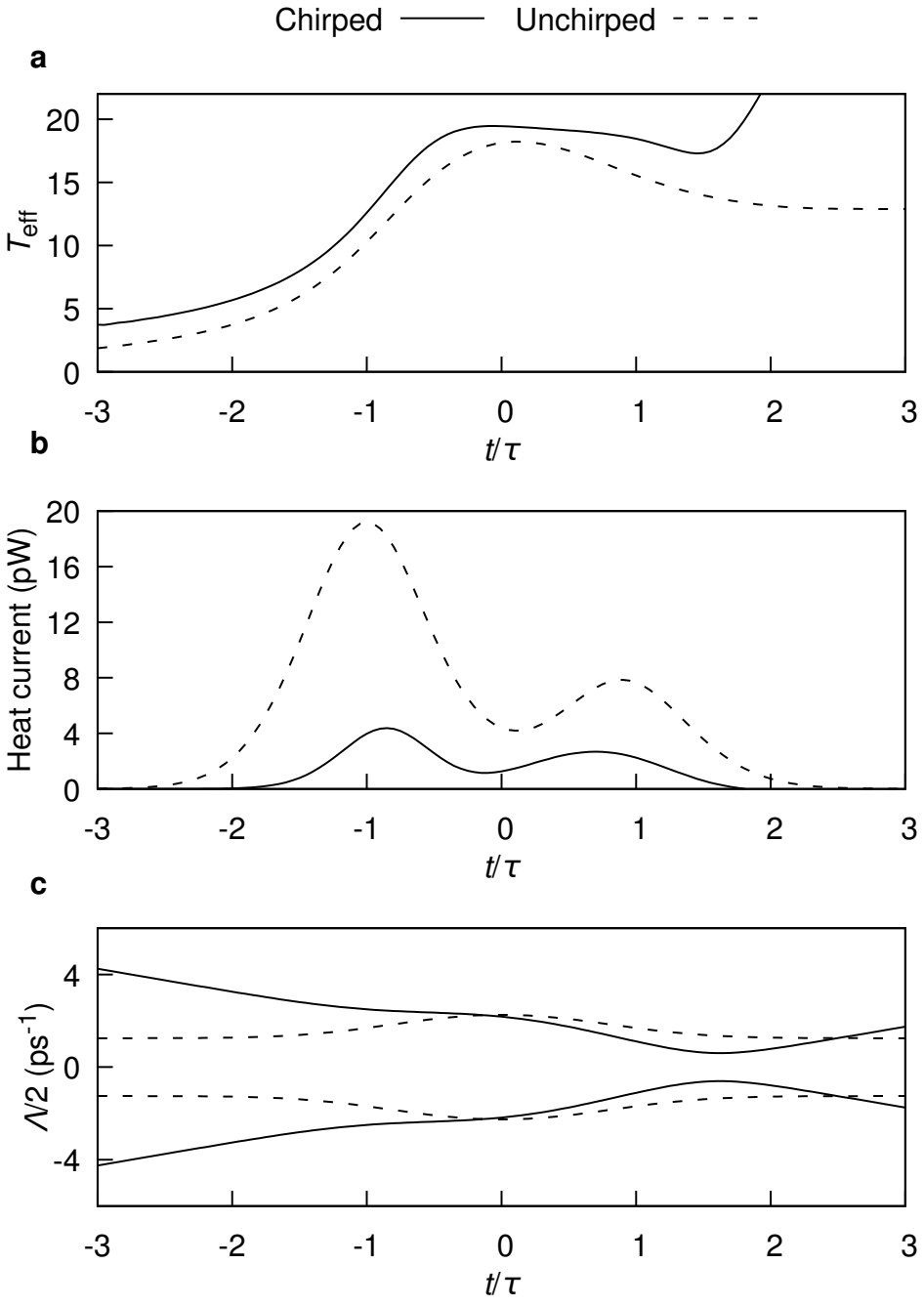

Figure 2.7: Results showing how chirping of the driving pulse leads to a reversible heat transfer. (a) Effective temperature of the dot as a function of time for the chirped Carnot pulse (solid) and unchirped comparator pulse (dashed). (b) Corresponding heat currents as a function of time. (c) Corresponding dressed-state frequencies, $\Lambda/2$, as a function of time. Time is given in units of the pulse duration, τ, in each case

2.2.5 Probability Distributions For Heat and Work

For the sake of convenience in analysing the heat and work distributions together, we change convention here and regard Q as the heat emitted by the exciton into the phonons, such that $Q < 0$ is interpreted as heat absorbed from the phonons. With this in mind, the probability distribution for the heat absorbed after the driving sequence is shown in fig. 2.8, for both the Carnot pulse and the unchirped comparator pulse we introduced above. The key differences between the two distributions are the behaviour at $Q = 0$, and the total weight in the $Q < 0$ sector. The corresponding work distributions are shown in fig. 2.9.

Before analysing these distributions, we note that the heat and work distributions are related. it is easiest to consider these distributions from the point of view of the set of possible trajectories which the system can take, evolving throughout the driving protocol. These trajectories generally involve the system evolving along the lower dressed state, with possible jumps between the dressed states occurring with the associated emission or absorption of phonons. Naturally, we can partition the trajectories into the set which take the exciton state from $|0\rangle$ to $|1\rangle$, and the set which takes the exciton from $|0\rangle$ to $|0\rangle$. Partitioning the set of trajectories like this also results in partitioning the distribution functions similarly.

The work distribution is essentially generated by shifting the portion of the heat distribution function corresponding to the set of trajectories $|0\rangle \to |1\rangle$ by an amount E_G. The portion of the heat distribution corresponding to the set of trajectories $|0\rangle \to |0\rangle$, is shifted by 0, i.e., unchanged. This is seen clearly from the plots, but is easily understood from the eqn. 2.33 for the characteristic function of work. The characteristic function for work and heat only differed in the projective measurement $e^{+iuE_G|1\rangle\langle 1|}$ on the state at time $t = -\infty$ and $e^{-iuE_G|1\rangle\langle 1|}$ on the state at $t = +\infty$. The initial measurement, at the start of the protocol, always returns a phase factor e^0, since $\rho(-\infty) = |0\rangle\langle 0|$. The final measurement, after the protocol, then adds a phase factor $e^{+iE_G u}$ in the characteristic function for all trajectories which end with the exciton in the state $|1\rangle$. Taking the Fourier transform to get $P(W)$, this results in a shifting of this portion of the distribution.

Unchirped Pulse Heat Distribution

Looking first at the comparator pulse, the peak at $Q = 0$ in the heat distribution function indicates a high probability that there is no heat exchange with the environment. In terms of the dressed state trajectories, this would correspond to a perfect adiabatic evolution along the lower dressed state, with no transitions between the dressed states. We also see shoulders either side of this $Q = 0$ peak in the distribution. These fluctuations around $Q = 0$ come from trajectories where the exciton begins and ends in $|-\rangle$, but which include transitions between the dressed states during the driving sequence.

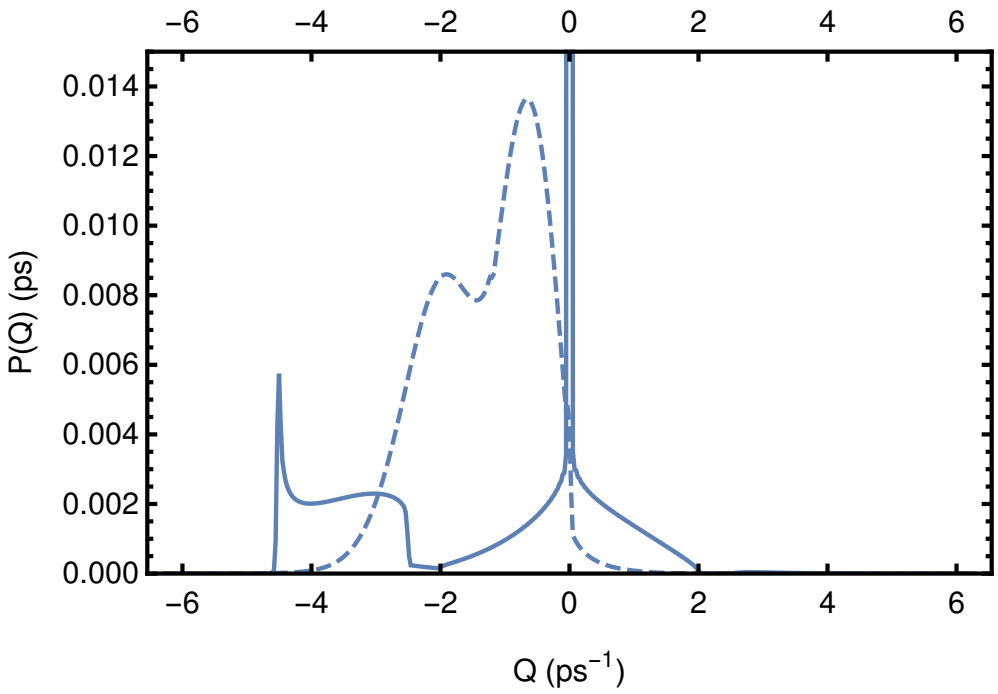

Figure 2.8: Probability distribution function for the heat transferred from the quantum dot to the phonon reservoir for the Carnot pulse (dashed) and the unchirped comparator pulse.

Crucially, an even number of transitions are needed, such that the exciton ends back in the lower dressed state, $|-\rangle$. The fluctuations of the energies of emitted/absorbed phonons, due to the time-dependent dressed state splitting $\Lambda(t)$, result in some small net heat emitted or absorbed by the exciton.

For the comparator pulse, we see a portion of the distribution weighted in a finite region in the $Q < 0$ sector. This portion of the distribution is due to the set of trajectories which leave the state of the dot as $|+\rangle$, at the end of the driving sequence. Such trajectories necessarily involve the net absorption of phonons. This follows as the system is initially in $|0\rangle$, corresponding to $|-\rangle$ for this chirpless, red detuned pulse. From the distribution, we can see that this region is bounded such that there is a maximum amount of heat that can be absorbed. This maximum heat that can be absorbed is simply the maximum of the dressed state splitting, as seen in fig. 2.7(c) as the splitting at $t = 0$ ps. for a trajectory for which there is only a single jump, the minimum heat absorption is simply the fixed detuning of the laser pulse 2.5ps^{-1}. Smaller quantities of heat can be absorbed through trajectories with more jumps. For example, a phonon can be absorbed at some intermediate dressed state splitting, with a subsequent phonon emission at the maximum dressed state splitting and a final phonon absorption at the minimum splitting. This can be seen in the distribution, where the probability of absorbing a quantity of heat smaller than the fixed detuning drops off rapidly due to the need for multiple exciton-phonon scattering events.

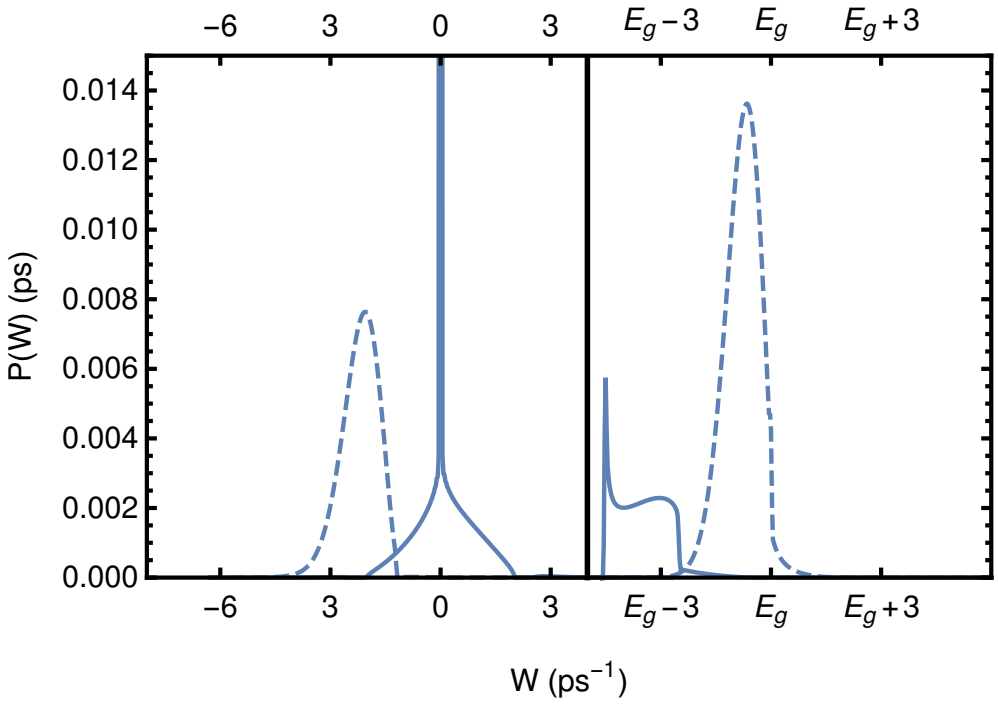

Figure 2.9: Probability distribution function for the work done on the quantum dot by the Carnot pulse (dashed) and the unchirped comparator pulse. Left of the vertical line is the distribution from -6 ps^{-1} to $+3$ ps^{-1} and right of the line is the portion of the distribution from $E_G - 3$ ps^{-1} to $E_G + 6$ ps^{-1}.

Chirped Pulse Heat distribution

For the distribution function of the Carnot driving sequence, we see that most of the distribution is weighted in the $Q < 0$ sector. There is no discernable peak at $Q = 0$. The dominant structure in the distribution is the presence of two broad peaks. We can get more of an insight into the heat distribution of the Carnot pulse, by first examining the probability distribution for work, as the heat distribution is not so easily partitioned as it was for the comparator pulse.

Chirped Pulse Work distribution

To unpack the work distributions, it is best to again treat the unchirped pulse and chirped pulse separately. Starting with the chirped Carnot pulse, if we take a trajectory where 0 jumps occur, and the system adiabatically follows along $|-\rangle$, ending in $|1\rangle$, this would contribute to the heat distribution function as some weight at $Q = 0$. This weight would then be shifted to E_G in the work distribution, through the phase factor in the characteristic function. We can intuitively regard this as the laser performing E_G worth of work on the excitonic degrees of freedom. If we now include trajectories which have jumps, but still leave the QD in $|-\rangle$, any deviations from $W = E_G$ arise from the phonon absorption and emission events during the driving protocol, with the deviation being equal to the heat absorbed or emitted. This is seen in the distribution, which has a large weight centred slightly left of E_G. This portion of the distribution suggests

that the majority of such trajectories actually involve the absorption of heat, such that $W < E_G$. This can be understood from the temporal structure of the dressed state splitting for Carnot pulse, as seen in fig. 2.7 (c). The splitting has a general tendency to decrease, at least while the heat flow is significant, seen in panel (b) of the same figure. Any phonon absorption jump which takes the system from $|-\rangle$ to $|+\rangle$, can only be followed by a phonon emission jump from $|+\rangle$ to $|-\rangle$, with the emitted phonon then having less energy than the absorbed phonon, resulting in a net heat absorption. However, it is not impossible for $W > E_G$, which would arise through the absorption of a phonon at the minimum $\Lambda(t)$, and subsequent emission of a phonon with a greater energy, such that heat is emitted into the phonons, rendering $W > E_G$.

The portion of the heat distribution which is attributed to measuring the dot in the $|0\rangle$ state after the pulse, does not acquire this phase factor and so is not shifted, and remains the same in the work distribution. To measure $|0\rangle$ at the end of the protocol, a jump from $|-\rangle$ to $|+\rangle$ with phonon absorption is required. In such trajectories, we can use the first law, $\Delta E = 0 = \Delta W + \Delta Q$, to say negative work is performed in a sense, by an amount equal to the heat transferred from phonons to exciton, as seen in the work distribution, where the weight of the distribution is supported over negative values. This portion of the distribution is peaked, and has a sharp cutoff suggesting that there is a minimum amount of work done, or in terms of heat, a minimum amount of heat that is absorbed from the phonons. This is due to the minimum possible energy that an absorbed phonon can have, as seen in the dressed state splitting structure in fig. 2.7(c), much like the case of the unchirped pulse. In principle, there is no strict maximum amount of heat absorbed, where we see a soft decay in the probability distribution. Increasingly large values of $\Lambda(t)$ for the phonon energies, become decreasingly likely, as these values occur when $\Omega(t)$ tends to 0, i.e., as $t \to -\infty$, where the scattering rates also tend to 0.

Unchirped Work Distribution

For the unchirped pulse, $|-\rangle_{t\to-\infty} = |-\rangle_{t\to+\infty} = |0\rangle$, and so any trajectories which have no jumps but simply involve the system adiabaticaly evolving along $|-\rangle$, will contribute weight to $Q = 0$ and to $W = 0$. Fluctuations around $W = 0$ in this case, again correspond to trajectories which contain a set of jumps between the dressed states but which overall return the system to $|-\rangle$. We see this in the work distribution, with a large peak at $W = 0$, which has shoulders either side. The work distribution only has finite values close to $W = E_G$ for trajectories which take the system from $|-\rangle$ to $|+\rangle$. Such trajectories necessarily involve the absorption of a phonon. This is clearly seen in the distribution, which satisfies $W < E_g$.

2.3 Conclusions

We have shown that a theory of open quantum systems [122] can be extended to allow the calculation of quantum thermodynamic quantities. Unlike previous work [101] our theory applies to time-dependent Hamiltonians and, therefore, quantum-control experiments. Using this approach we have studied the thermodynamics of a quantum-dot exciton driven by a chirped laser pulse, and evaluated the exciton-phonon heat flow, entropy generation, and effective exciton temperature during the pulse. We have predicted that certain pulses, which are readily accessible experimentally, induce heat transfers from the phonons to the excitons, and that, in some cases, this heat transfer approaches the ideal reversible limit. In the context of a heat engine, such a process gives an efficiency close to the Carnot limit.

More generally, our results show that shaped laser pulses can be used to implement controlled thermodynamic processes for a single exciton transition interacting with the heat bath of phonons. The laser pulse amplitude allows for modulation of the heat flow, a feature which is essential for the implementation of thermodynamic cycles, yet is lacking in physical implementations of quantum thermodynamic machines. The pulse profile also allows simultaneous, yet independent, control over the effective temperature of the dressed-exciton system.

3 Optimal Heat Transfer in Quantum Dots

In the previous chapter, we developed a theory of controllable heat transfer between a laser driven quantum dot and the phonon modes of the host environment. We saw the benefit of the effect of the linear chirp on the temporal structure of the dressed state splitting, which was to effectively perform a compression stroke and an expansion stroke resulting in isothermal heat transfer. It stands to reason, then, that by shaping the temporal structure of the dressed state splitting beyond that of a simple linear chirp, it should be possible to increase the efficiency of the heat stroke. We simply need to ensure that the dynamics of the level splitting is such that the effective temperature of the system in the basis of the dressed states always remains close to the bath temperature. Although this requirement is simple to state and intuitive, finding such a dressed state structure is tricky. Changing the dressed state splitting to compensate for changes in the populations involves changing the structure of the dressed states themselves. This in turn will further affect the dynamics of the populations. In order to solve this problem, we can make use of numerical optimisation methods. We can maximise the efficiency in the space of dressed state splitting temporal profiles. This allows us to probe how close to the Carnot efficiency this model can get to, in a finite time. The results presented in this chapter are a proof of principle, and lay the foundation for a more rigorous and in depth analysis on the topic.

3.1 Pulse Shaping

The dressed state splitting, $\Lambda(t)$, is a function of both the detuning, $\Delta(t)$ and the Rabi frequency $\Omega(t)$. To explore the space of possible dressed state splitting profiles, we must first define these quantities. For a completely general shaped laser pulse, we would optimise over the shape of both the Rabi frequency (electric field amplitude) and the detuning. This can lead to unphysical laser profiles. In order to simplify the problem, we restrict our analysis to that of a Gaussian laser pulse, with a shaped

detuning profile. We take the Rabi frequency to be of the form

$$\Omega(t) = \Omega_0 e^{-t^2/\left(2\tau^2\right)} \tag{3.1}$$

with two parameters, the amplitude Ω_0 and pulse duration τ. We define the detuning as a linear interpolation between N points, $(\Delta_1, \Delta_2, ..., \Delta_N)$, defined on the time interval $t \in [-4\tau, 4\tau]$. We vary the shape of the detuning profile by varying the values of the points on this time interval. By shaping the detuning, we can control the shape of the dressed state splitting structure. We can then maximise the value of any quantity with respect to the shape of the detuning and the parameters of the Gaussian pulse using a local optimisation algorithm. In this work, we perform the optimisation using an unconstrained principle axis local optimisation algorithm. Specifically, we use the in-built "FindMaximum" function in Mathematica.

This algorithm requires a seed value for the detuning profile and pulse parameters. For this seed, we use the Rabi frequency $\Omega(t)$ and detuning $\Delta(t)$ of a linearly chirped Gaussian laser pulse, which maximises the quantity of interest. The linearly chirped pulse here is defined through

$$\Delta(t) = \alpha t + \delta, \tag{3.2}$$

$$\Omega(t) = \Omega_0 e^{-t^2/\left(2\tau^2\right)}. \tag{3.3}$$

We note that the coefficient α is known as the temporal chirp, which we wrote explicitly as a function of the spectral chirp a in the previous chapter. We use the same optimisation algorithm to optimise the efficiency over a, Ω_0 and δ. We use $\alpha = -0.004$ ps^{-2} and $\Omega_0 = 6$ps^{-1} as seed values, for a range of values of τ. Doing this, we generate a set of starting values for the shape optimisation, for a set of pulses with increasing values of τ.

3.2 Optimised Efficiency

We are interested in maximising the reversibility of the heat absorption. To achieve this, we can maximise the efficiency of the model heat engine described in the previous chapter. Fig. 3.1 shows maximised efficiencies, relative to the Carnot efficiency, for both the optimised linearly chirped pulse and the shaped pulse as a function of the laser pulse duration τ. These results were generated using $N = 15$ points to define the temporal profile of the detuning. We note, that these results were generated, with the initial condition $\rho(-\infty) = 0.001\,|1\rangle\langle 1| + 0.999\,|0\rangle\langle 0|$. We add a small occupation to the $|1\rangle$ state, so that the optimiser can always define a finite positive temperature for the exciton in the dressed state basis. Immediately from the results, we can state that it is always possible to improve the efficiency, by using a shaped laser pulse over a linearly

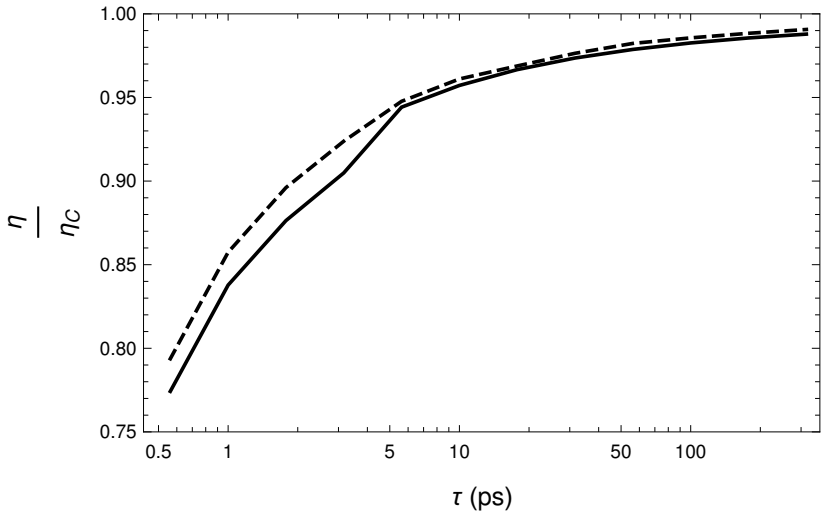

Figure 3.1: Efficiency for optimised linearly chirped pulse (solid) and optimised shaped pulse (dashed) as a function of the pulse duration τ.

chirped laser pulse. Moreover, we can see that simply increasing the duration of the laser pulse has the largest effect on improving the efficiency, with longer linearly chirped pulses achieving high efficiencies. For both the optimised linearly chirped pulse and the optimised shaped pulse, increasing τ results in efficiencies which are arbitrarily close to the Carnot efficiency, which for this set of parameters is $\eta_C = 1 - 2.7/20 = 0.865$. The relative improvement in the efficiency due to the shaping is much greater for shorter pulses, with a decreasing benefit as we increase the pulse duration, however for shorter pulses, the overall efficiencies are furthest from the Carnot efficiency.

For the longest pulse, $\tau \approx 300$ ps we reach 99.1% of the Carnot efficiency, an unsurprising result. Basic thermodynamics tells us that each stroke in a Carnot engine needs to be performed adiabatically, which can only be achieved in the infinite time limit. Surprisingly, we achieve such efficiencies without a reduction in the total amount of heat absorbed. Fig. 3.2 shows the heat absorbed for both the optimised linearly chirped pulse and the shaped pulse, as a function of pulse duration τ. We see that the heat absorption increased with increased pulse duration. One would expect that, in principle, one could maximise the efficiency by moving to a regime where almost no heat is exchanged between the system and the bath, reducing the entropy production to zero. This is obviously problematic in the limit where no heat is absorbed, in which case the efficiency is defined as 0/0. We would however expect the optimiser to at least approach this solution. That we find these increasing optimised efficiencies with increasing heat absorption is almost certainly a feature of the optimisation algorithm finding local maxima. We start each run with a linearly chirped seed. It is likely the optimiser is then finding a locally optimal solution, close to that of the linear chirped seed.

In principle, the limit of zero heat absorption can be reached by either choosing Ω_0 to be small such that the rates $\gamma_{a/e}$ are negligible, or by choosing Ω_0 to be so large that

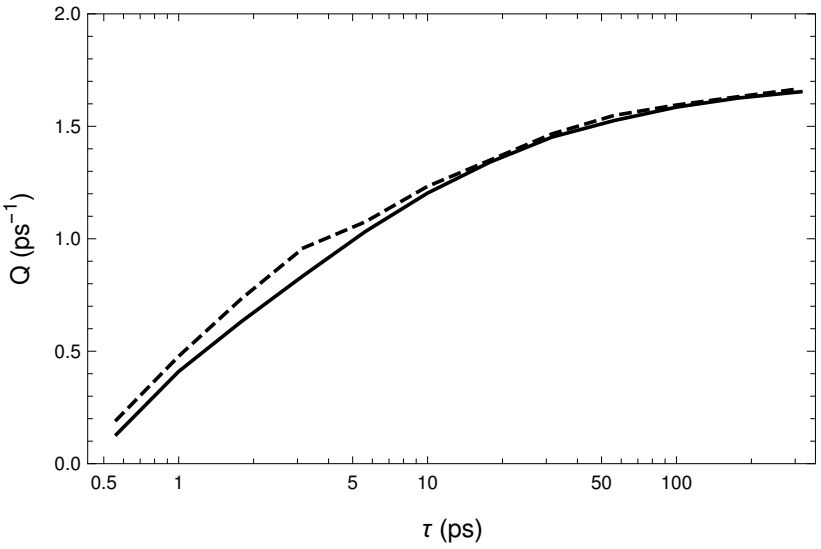

Figure 3.2: Heat absorption for optimised linearly chirped pulse (dashed) and optimised shaped pulse (solid) as a function of the pulse duration τ.

the dressed state splitting lies beyond the peak of the spectral density and the rates are again negligible.

3.3 Optimised Detuning Profile

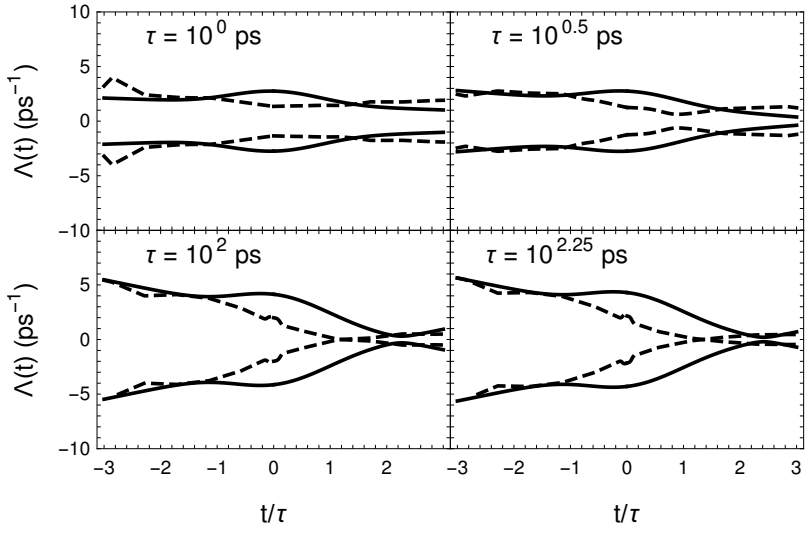

Figure 3.3: The optimal detuning shape for the case of the linear chirped pulse (solid) and shaped pulse (dashed) for four different values of pulse length

We now compare the detuning of the linearly chirped pulse and the shaped pulses along with the resulting dressed state splitting, we can get a sense of what shapes the optimization algorithm is finding. Fig. 3.3 compares the detuning for two short pulses and two longer pulses, with the associated dressed state splitting plotted in fig. 3.4. We see that the optimised detuning shape has different characteristic features for the short and long pulses. For the short pulses, the linear detuning is modified such that before

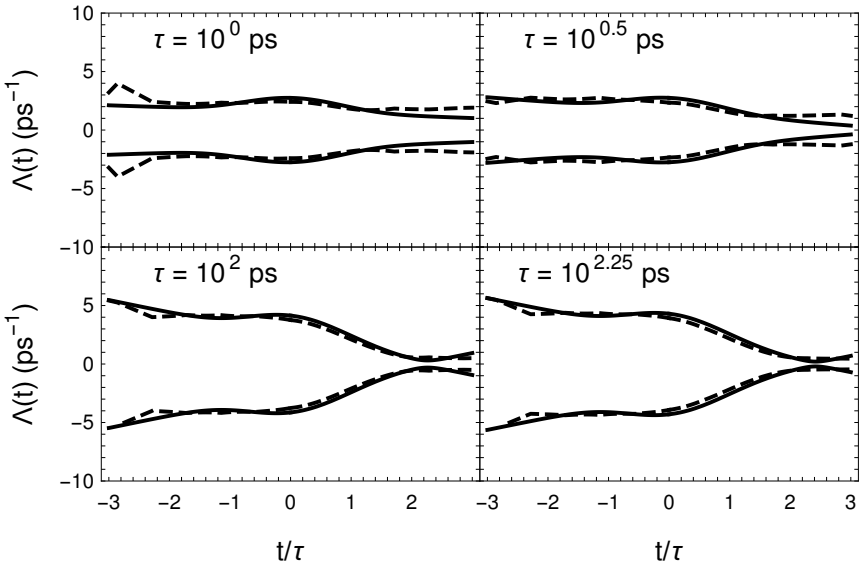

Figure 3.4: The optimal dressed state splitting for the case of the linear chirped pulse (solid) and shaped pulse (dashed) for four different values of pulse length

the peak of the pulse amplitude, the system reduces the detuning, then increasing after the peak of the pulse. The result in the dressed state splitting profile is slightly lower splitting at close to the centre of the pulse (the equivalent of an expansion of a gas), with the levels expanding towards the tail end of the pulse (compression).

In contrast, for the longer pulses, we typically only see this accelerated reduction of the dressed state splitting, an expansion stroke, resulting in an overall reduction in the dressed state splitting compared to the case of the linearly chirped pulse. As time progresses, the rate of this expansion decreases and the detuning reaches a fixed value, with the dressed state splitting also remaining constant, in comparison to the linearly chirped case, which has diverging levels in the tail end of the pulse.

3.4 Effective Temperature

To understand the effects of these shaped detunings on the efficiency, we can examine the corresponding effective temperature plots. As in the previous chapter, we define the effective temperature of the system through the ratio of the dressed state populations.

$$\frac{p_+}{p_-} = e^{-\Lambda(t)/k_B T_{\mathrm{Eff}}}. \tag{3.4}$$

Fig. 3.5 shows the effective temperature of the system as function of time. The common feature of all four shaped pulses is a plateau in the effective temperature at times $t > 0$, in contrast to the linearly chirped case. Here the system is exchanging heat with the phonons, at a constant temperature, an isothermal heat transfer. The plateau of the temperature is different for the short and long pulses. For short pulses, we see the isothermal heat exchange at about $T = 15$ K, and a value of $T = 20$ K for the

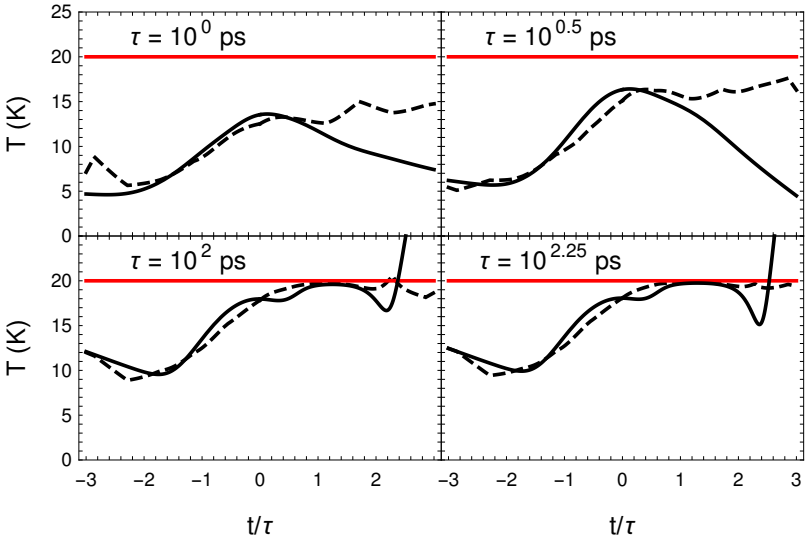

Figure 3.5: The resulting effective temperature of the exciton as function of time for the case of the linear chirped pulse (solid) and shaped pulse (dashed) for four different values of pulse length. The bath temperature at $T = 20$ K is indicated in red.

longer pulses. This explains the difference in efficiency between the long and short pulses.

Although these shorter pulses are producing isothermal heat transfer, the temperature gap between the system and bath is always finite, leading to an increased entropy production. Comparing the temperature profile of the linearly chirped pulse and the longer shaped pulse, we note that the system reaches $T = 20$ K more quickly and stays at 20 K for longer. This is a result of the decreasing expansion rate we saw in the detuning structure (slowing down of the reduction of the level reduction). As it stands, the linear chirped pulse is quite good. Where the temperature differs from 20 K at late times, $\Omega(t)$ is sufficiently small such that the heat absorption powers are negligible. Any heat transfer occurring here, at this point of high temperature difference, is small, and has a minor contribution to the entropy production. This explains the small increase in efficiency we see when we shape the detuning of longer laser pulses.

3.5 Conclusions

We have shown that it is possible to increase the control of thermodynamic processes through shaping of the temporal profile of the frequency of driving laser. In the quantum dot exciton model we investigate, this increased control lead to increased efficiencies for a heat engine cycle, compared with the case of a simple linearly chirped Gaussian pulse. These locally optimal shapes resulted in an increase in the duration of the isothermal heat absorption from the phonon bath, which increased the overall efficiency of the cycle. Moreover, these increasingly efficient pulses also lead to an increase in the heat absorbed per pulse. This work is a proof of principle, and lays the

foundation for a more thorough examination of optimised thermodynamic processes in laser controlled quantum dots.

Part II

Steady State Heat Pumping

4 Steady State Heat Pumping with Quantum Dots

In chapter 2 we developed a theory to capture the thermodynamic properties of laser induced heat flows when driving a quantum dot exciton with linearly chirped Gaussian pulses. The steady state equivalent of this model was considered by Gauger and Wabnig [121], where the authors considered the potential to use semiconductor quantum dots as a platform for optical refrigeration. In this chapter we treat the same steady state problem, extending the work by writing an analytical expression for the heat absorption power, as a function of the laser parameters and solving for the full probability distribution of both the number of phonons absorbed, and the excess excitation emitted into the photon reservoir. To do this, we write a master equation for the quantum dot exciton coupled to two reservoirs, the phonon bath already considered, and now also the electromagnetic environment. The coupling to the electromagnetic environment captures the spontaneous emission of photons by the exciton, in effect, closing the cycle. From this model we are able to write down the steady state solution, by treating the spontaneous emission in the basis of laser dressed states. The analytical solution for the steady state of the system then quickly leads to an analytical expression for the heat power. We use insights from this simple two level case to build a theory of laser cooling of the silicon vacancy centre in diamond, which we predict to be much more achievable, albeit more complicated. This is outlined in chapter 5.

Beyond the treatment of mean heat power, we again consider the full probability distribution for the heat exchange. In this problem, we now have heat exchange between the QD exciton and two baths, typically heat absorbed from the phonons and heat spontaneously emitted as photons. We write a counting field master equation, for the steady state two bath problem, now with two counting fields, each keeping track of the heat exchanged with either bath.

4.1 Analytical Theory of Heat Pumping

4.1.1 Laser Driven Exciton-Phonon-Photon Model

To implement a laser cooling protocol, we need two baths. The bath to be cooled, the phonons, and the bath into which we pump heat, the electromagnetic environment. In our model, spontaneous emission of photons by the quantum dot exciton will act as the channel for emitting the absorbed heat. We discard the time dependent driving due to a chirped laser pulse, and now consider a constant frequency constant amplitude laser field. We will again make use of a secularised Bloch Redfield master equation in Lindblad form, and use an almost identical derivation to that used in chapter 2. The only differences arise from the extra terms in the Hamiltonian describing the exciton-photon scattering, $H_{x-\text{photon}} = \sum_k f_k s^+ a_k + f_k^* s^- a_k^\dagger$, and the photon bath Hamiltonian, $\sum_k \omega_k a_k a_k^\dagger$. The full Hamiltonian for the laser driven exciton-phonon-photon system is then

$$\begin{aligned} H &= \Delta s_z - \Omega s_x \\ &+ s_z \sum_k \left(g_k b_k + g_k^* b_k^\dagger \right) + \sum_k \nu_k b_k b_k^\dagger \\ &+ \sum_k f_k e^{+i\omega_l t} s^+ a_k + g_k^* s^- e^{-i\omega_l t} f_k^\dagger + \sum_k \omega_k a_k a_k^\dagger \\ &= H_S + H_I^1 + H_B^1 + H_I^2 + H_B^2, \end{aligned} \tag{4.1}$$

in the rotating frame, having performed the RWA. Note the phase factors on s^+ and s^-, originating from the unitary transformation to the rotating frame. Again, $\Delta = E_g - \omega_l$ and $\Omega = E_0 \langle 0| \vec{\hat{d}} \cdot \vec{e} |1\rangle$, as in the previous chapter.

In this instance, the eigenstates of the system Hamiltonian, $|+\rangle$ and $|-\rangle$, no longer have time dependent coefficients, when expanded in the set of exciton basis states. This is due to the constant amplitude, constant frequency laser driving. Using the same pseudo spin operator notation, $R_z = 1/2 \left(|+\rangle \langle +| - |-\rangle \langle -| \right)$ and $R_+ = |+\rangle \langle -|$, we can expand the lab frame pseudo-spin operators as

$$\begin{aligned} s_z &= \frac{\Delta}{\Lambda} R_z + \frac{\Omega}{\Lambda} \left(R_+ + R_- \right) \\ ,s^+ &= \frac{\Omega}{\Lambda} R_z + \left(\frac{\Delta + \Lambda}{2\Lambda} \right) R_+ + \left(\frac{\Delta - \Lambda}{2\Lambda} \right) R_- \\ ,s^- &= \frac{\Omega}{\Lambda} R_z + \left(\frac{\Delta - \Lambda}{2\Lambda} \right) R_+ + \left(\frac{\Delta + \Lambda}{2\Lambda} \right) R_- \ . \end{aligned}$$

We transform to the interaction picture to derive the master equation. $\tilde{H}_I = U^\dagger H_I U$

with $U = e^{-i\left(H_s+H_B^1+H_B^2\right)}$, so that $a^{\pm} \to a^{\pm}e^{\mp i\omega_k t}$ and $b^{\pm} \to b^{\pm}e^{\mp i\nu_k t}$. The lab frame system pseudo spin operators transform accordingly as

$$\tilde{s}_z = \frac{\Delta}{\Lambda}R_z + \frac{\Omega}{\Lambda}\left(R_+e^{+i\Lambda t} + R_-e^{-i\Lambda t}\right) \tag{4.2}$$

$$,\tilde{s}^+ = \frac{\Omega}{\Lambda}R_z + \left(\frac{\Delta-\Lambda}{2\Lambda}\right)R_+e^{+i\Lambda t} + \left(\frac{\Delta+\Lambda}{2\Lambda}\right)R_-e^{-i\Lambda t} \tag{4.3}$$

$$,\tilde{s}^- = \frac{\Omega}{\Lambda}R_z + \left(\frac{\Delta+\Lambda}{2\Lambda}\right)R_+e^{+i\Lambda t} + \left(\frac{\Delta-\Lambda}{2\Lambda}\right)R_-e^{-i\Lambda t}\ . \tag{4.4}$$

The interaction Hamiltonian in the interaction picture becomes.

$$\begin{aligned}\tilde{H}_I =& \tilde{s}_z\sum_k g_k b_k e^{+i\nu_k t} + g_k^* b_k^\dagger e^{-i\nu_k t} + \\ & \sum_k f_k\tilde{s}^+e^{+i\omega_l t}a_k e^{-i\omega_k t} + f_k^*\tilde{s}_-e^{-i\omega_l t}a_k^\dagger e^{+i\omega_k t}\end{aligned} \tag{4.5}$$

Making the Born-Markov approximations and the secular approximation, we find the Born-Markov master equation for the driven exciton-phonon-photon problem,

$$\begin{aligned}\dot{\rho}_S =& -i\left[H_S,\rho\right] \\ & -\pi\left(\frac{\Omega}{2\Lambda}\right)^2 J^{\text{phon}}(\Lambda)\left(n(\Lambda)+1\right)\mathcal{D}\left[R_-\right]\rho_S \\ & -\pi\left(\frac{\Omega}{2\Lambda}\right)^2 J^{\text{phon}}(\Lambda)n(\Lambda)\mathcal{D}\left[R_+\right]\rho_S \\ & -\pi\left(\frac{\Delta}{\Lambda}\right)^2 J^{\text{phon}}(0)\left(n(0)+1\right)\mathcal{D}\left[R_z\right]\rho_S \\ & -\pi\left(\frac{\Delta+\Lambda}{2\Lambda}\right)^2 J^{\text{phot}}(\omega_l+\Lambda)n(\omega_l+\Lambda)\mathcal{D}\left[R_+\right]\rho_S \\ & -\pi\left(\frac{\Delta+\Lambda}{2\Lambda}\right)^2 J^{\text{phot}}(\omega_l+\Lambda)\left(n(\omega_l+\Lambda)+1\right)\mathcal{D}\left[R_-\right]\rho_S \\ & -\pi\left(\frac{\Delta-\Lambda}{2\Lambda}\right)^2 J^{\text{phot}}(\omega_l-\Lambda)n(\omega_l-\Lambda)\mathcal{D}\left[R_-\right]\rho_S \\ & -\pi\left(\frac{\Delta-\Lambda}{2\Lambda}\right)^2 J^{\text{phot}}(\omega_l-\Lambda)\left(n(\omega_l-\Lambda)+1\right)\mathcal{D}\left[R_+\right]\rho_S \\ & -\pi\left(\frac{\Omega}{\Lambda}\right)^2 J^{\text{phot}}(\omega_l)n(\omega_l)\mathcal{D}\left[R_z\right]\rho_S \\ & -\pi\left(\frac{\Omega}{\Lambda}\right)^2 J^{\text{phot}}(\omega_l)\left(n(\omega_l)+1\right)\mathcal{D}\left[R_z\right]\rho_S,\end{aligned} \tag{4.6}$$

with $\mathcal{D}\left[A\right]\rho(t) = \left(A^\dagger A\rho + \rho A^\dagger A - 2A\rho A^\dagger\right)\rho(t)$ and where we have introduced the spectral density function characterising the interaction between the exciton and each bath, $J^{\text{phon}}(\omega) = \sum_k |g_k|^2\delta\left(\omega-\omega_k\right)$ and $J^{\text{phot}}(\omega) = \sum_k |f_k|^2\delta\left(\omega-\nu_k\right)$. For the phonon spectral density we again take $J^{\text{phon}}(\omega) = \frac{A\hbar}{k_B\pi}\omega^3 e^{-\omega^3/\omega_c^3}$, with $\hbar\omega_c$ (cutoff frequency)

= 2 meV, $A = 11.2$ fs K^{-1} [123]. We will discuss the spectral density of the photons shortly. The first line of eqn. 4.6 captures the coherent evolution of the excitonic degrees of freedom under the action of the driving laser. The next three lines capture the effects of the dissipation due to the phonons as before. The final six, capture the photonic contributions to the dissipation. The spectral density and occupation functions in the photonic contribution are sampled at frequencies ω_l and $\omega_l \pm \Lambda$, not Λ, as is the case for the phonons. Mathematically this is due to the $e^{\pm i\omega_l t}$ phase factors we introduced in the rotating frame, but physically, these frequencies are the Mollow triplet seen in the emission spectrum of a driven two level emitter [126].

A similar master equation could have been found by simply adding in a phenomenological dissipator, $\gamma D\left[|0\rangle\langle 1|\right]$, which captures a simple spontaneous emission process from $|1\rangle$ to $|0\rangle$ at some rate γ. However, in doing this, the effect of the dissipation in the basis of laser dressed states isn't immediately clear. Writing all dissipators with jump operators in the basis of the laser dressed states allows us to write down an analytical expression for the steady state of the system, as well as the steady state heat power.

At room temperature, the Bose occupation function of the photons at energy scales of $\hbar\omega_l \sim 1$ eV is negligible, and we have

$$\begin{aligned}\dot{\rho}_S = &-i\left[H_S, \rho\right] \\ &- \left[\left(\frac{\Omega}{2\Lambda}\right)^2 \gamma_0(\Lambda)\left(n(\Lambda)+1\right) + \left(\frac{\Delta+\Lambda}{2\Lambda}\right)^2 \gamma_0'\right] \mathcal{D}\left[R_-\right]\rho_S \\ &- \left[\left(\frac{\Omega}{2\Lambda}\right)^2 \gamma_0(\Lambda) n(\Lambda) + \left(\frac{\Delta-\Lambda}{2\Lambda}\right)^2 \gamma_0'\right] \mathcal{D}\left[R_+\right]\rho_S \\ &- \left(\frac{\Omega}{\Lambda}\right)^2 \gamma_0' \mathcal{D}\left[R_z\right]\rho_S \end{aligned} \tag{4.7}$$

with $\gamma_0(\Lambda) = \pi J^{\text{phon}}(\Lambda)$ and $\gamma_0' = \pi J^{\text{phot}}(\omega_l)$. We have made the approximation that $J^{\text{phot}}(\omega \pm \Lambda) \approx J^{\text{phot}}(\omega)$, which is valid given the dressed state splitting is on the order of $\sim$ meV and ω_L is on the order of $\sim$ eV, and the spectral density for the photons is of the form $J(\omega) \propto \omega^3$ [92]. $\gamma_0(\Lambda)$ and γ_0' capture the fundamental times scales set by the scattering rates between the exciton and either bath at $T = 0$ K, without the dressed state prefactors, which we write explicitly in the master equation. In fact, γ_0' is simply the rate of spontaneous emission of photons from $|1\rangle$ to $|0\rangle$, the same quantity we would have used for the rate in the phenomenological model mentioned above. For the spontaneous emission rate, we take $\gamma_0' = 0.001$ ps^{-1} [124].

4.1.2 Steady State Solution

The effect of the combined phonon and photon dissipation results in a total rate $\Gamma_a^T = \Gamma_a + \Gamma_a'$, for transitions $|-\rangle \rightarrow |+\rangle$, and a total rate $\Gamma_e^T = \Gamma_e + \Gamma_e'$ for the rate of transitions $|+\rangle \rightarrow |-\rangle$. In this notation Γ_e and Γ_a are the phonon emission and absorption rates and Γ_e' and Γ_a' are the rates of transitions from upper to lower dressed states, and lower to upper dressed state, respectively, through the emission of photons, with

$$\Gamma_e = \pi \left(\frac{\Omega}{2\Lambda}\right)^2 J^{\text{phon}}(\Lambda)\left(n(+\Lambda)+1\right) \tag{4.8}$$

$$\Gamma_a = \pi \left(\frac{\Omega}{2\Lambda}\right)^2 J^{\text{phon}}(\Lambda) n(+\Lambda) \tag{4.9}$$

$$\Gamma_e' = \left(\frac{\Delta+\Lambda}{2\Lambda}\right)^2 \pi J^{\text{phot}}(\omega_l) \tag{4.10}$$

$$\Gamma_a' = \left(\frac{\Delta-\Lambda}{2\Lambda}\right)^2 \pi J^{\text{phot}}(\omega_l). \tag{4.11}$$

Note, although we associate transitions $|-\rangle \rightarrow |+\rangle$ with the absorption of phonons, it cannot be associated with the absorption of photons. We only capture photon emission, and the difference between transitions $|-\rangle \rightarrow |+\rangle$ and $|+\rangle \rightarrow |-\rangle$ arise in the energies of the emitted photons, namely, $\omega_l \pm \Lambda$. We expand on these differences when we consider the full counting statistics.

Since we are considering steady state driving, such that $\dot{\Delta} = \dot{\Omega} = 0$, we can analytically solve for both the state of the system and for the steady state heat pumping power. For the dynamics of the populations of the dressed states, we have

$$\dot{p}_+ = \frac{d}{dt}\langle +|\,\rho\,|+\rangle = \Gamma_a^T p_- - \Gamma_e^T p_+ \tag{4.12}$$

$$,\dot{p}_- = -\dot{p}_+ \tag{4.13}$$

$$,p_- + p_+ = 1. \tag{4.14}$$

Imposing the steady state condition, $\dot{p}_\pm = 0$, we find

$$p_+^{ss} = \frac{\Gamma_a^T}{\Gamma_e^T + \Gamma_a^T} \tag{4.15}$$

$$,p_-^{ss} = \frac{\Gamma_e^T}{\Gamma_e^T + \Gamma_a^T}. \tag{4.16}$$

We can calculate the power of heat absorption from the phonon reservoir to the using

$$\dot{Q} = \Lambda \dot{n} = \Lambda\left(p_- \Gamma_a - p_+ \Gamma_e\right), \tag{4.17}$$

which we derived from the theory of full counting statistics in chapter 2. This leads to

$$\dot{Q}_{ss} = \Lambda \left(\frac{\Gamma_a \Gamma'_e - \Gamma_e \Gamma'_a}{\Gamma_a + \Gamma'_a + \Gamma_e + \Gamma'_e} \right). \tag{4.18}$$

Substituting in eqns. 4.8, 4.9, 4.10 and 4.11, the heat power can be expressed as a function of the dressed state splitting and the detuning as

$$\dot{Q}_{\rm ss} = \Lambda \dot{n}_{\rm ss} = \Lambda \frac{\left\{ e^{-\beta\Lambda} - \left(\frac{\Lambda-\Delta}{\Lambda+\Delta}\right)^2 \right\} \left(\frac{\Lambda+\Delta}{2\Lambda}\right)^2 \gamma_0(\Lambda)\gamma'_0 \left(n(\Lambda)+1\right)}{\gamma_0(\Lambda)\coth\left(\beta\Lambda/2\right) + 2\gamma'_0 \left(\frac{\Lambda^2+\Delta^2}{\Lambda^2-\Delta^2}\right)}. \tag{4.19}$$

4.1.3 Heat Power Analysis

Intuitively we would expect that heat can only be pumped from the phonons to the photons, when the effective temperature of the photons, defined through

$$e^{-\Lambda/k_B T_{\rm phot}} = \frac{\Gamma'_a}{\Gamma'_e} = \left(\frac{\Lambda - \Delta}{\Lambda + \Delta} \right)^2, \tag{4.20}$$

is below that of the lattice, $T_{\rm phot} < T$. Note, the temperature $T_{\rm phot}$ we define here is not the real temperature of the photon bath. This is simply the effective temperature that describes the dissipation of the exciton due to the photons, when the dissipator is written in the basis of laser dressed states. Conversely, we would expect to see heating for $T_{\rm phot} > T$.

From eqn. 4.20, it is clear we have control over the effective temperature of the photon dissipation, through the laser parameters Δ and Ω. The first factor in eqn. 4.19, $e^{-\beta\Lambda} - \left(\frac{\Lambda-\Delta}{\Lambda+\Delta}\right)^2$, captures the temperature requirement for cooling, and the control of the effective temperature of the photons. Substituting eqn. 4.20 into this expression, this factor becomes

$$e^{-\beta\Lambda} - e^{-\beta_{\rm phot}\Lambda}. \tag{4.21}$$

For heat absorption from the phonons, $e^{-\beta\Lambda} > e^{-\beta_{\rm phot}\Lambda}$, or $T_{\rm phot} < T_{\rm L}$, as expected.

In terms of the driving parameters, for laser cooling we have

$$e^{-\beta\Lambda} > \left(\frac{\Lambda - \Delta}{\Lambda + \Delta} \right)^2. \tag{4.22}$$

For positive finite values of β and Λ, this condition can only be satisfied for positive values of detuning Δ, such the frequency of the laser tuned below the exciton transition frequency. In fig. 4.1, plot the region in the space of Δ and Ω, as well as in the space of the Δ and Λ, where the cooling condition is satisfied, for different lattice temperatures. We see there is a small region close to the $\Lambda = \Delta$ line that will sustain heat absorption

from the phonon reservoir. As the temperature of the phonon bath is increased, this region grows, but is always finite.

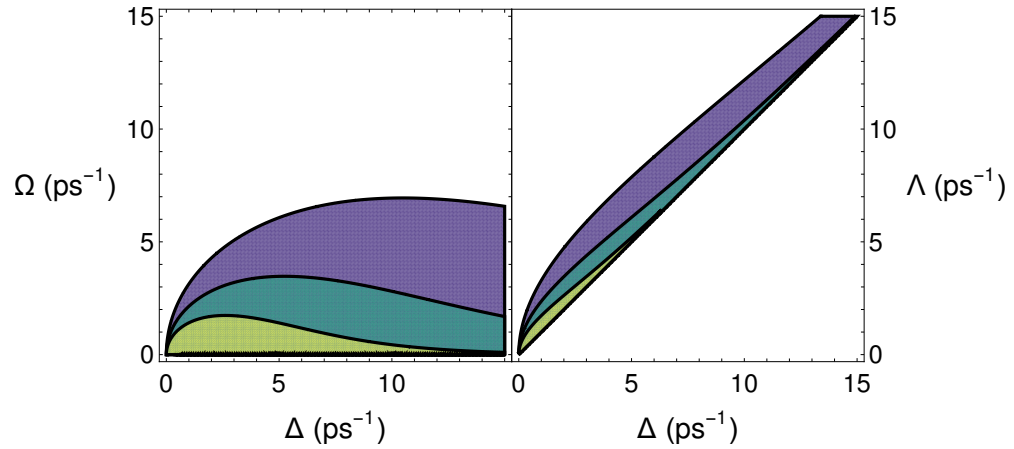

Figure 4.1: Laser cooling region for $T = 5$ K (yellow), 10 K (green) and 20 K (blue) in the space of Δ and Ω (a) and in the space of Δ and Λ (b).

In fig. 4.2 and fig. 4.3, we plot the steady state rate of phonon absorption, $\dot{n}_{\rm ss}$ and the steady state heat current, $\dot{Q}_{\rm ss}$, as a function of Δ and Ω. Both figures show a maximum value of the steady state rate of phonon absorption and heat absorption. The difference in the position of the peaks in these plots is due to the dependence of the energy of the absorbed phonons, Λ, on Δ and Ω. For weak driving strengths, we see that the steady state cooling power drops to 0, as expected. In this regime, the eigenstates of the driven QD Hamiltonian are the exciton basis states, $|0\rangle$ and $|1\rangle$. The exciton-phonon interaction Hamiltonian has no matrix elements connecting these two states. Once the driving strength is increased to have dressed states that are sufficiently mixed, the cooling power increases. As the driving strength is further increased, the cooling quickly decreases before the system begins to heat the phonon reservoir.

We see two key features in the heat absorption. The first is the strong dependence of the power on the driving strength, initially growing with increasing driving strength, before rapidly dropping to zero. The second is the broadening of the cooling region in Δ, as the driving strength is increased. The dependence of the cooling power on the driving strength is straightforward to see. The cooling power in eqn. 4.18 is proportional to $A^2 J^{\rm phon}(\Lambda) = (\Omega/2\Lambda)^2 J^{\rm phon}(\Lambda)$. Taking first $\Delta = 0$, this factor is then simply the spectral density $J^{\rm phon}$, which increases as Ω^3, before decreasing to zero due to a combination of the exponential cut-off in the spectral density and a depletion in the thermal occupation of higher energy phonon modes. For finite values of detuning, this simply results in $A < 1$ for increasingly large magnitudes of Δ, but with the general increase and subsequent rapid decrease, with increasing driving strength, the same, as can be seen in fig. 4.4.

In fig. 4.5 we plot the heat power as a function of detuning for different driving strengths. We now see more clearly this broadening of the heat absorption with in-

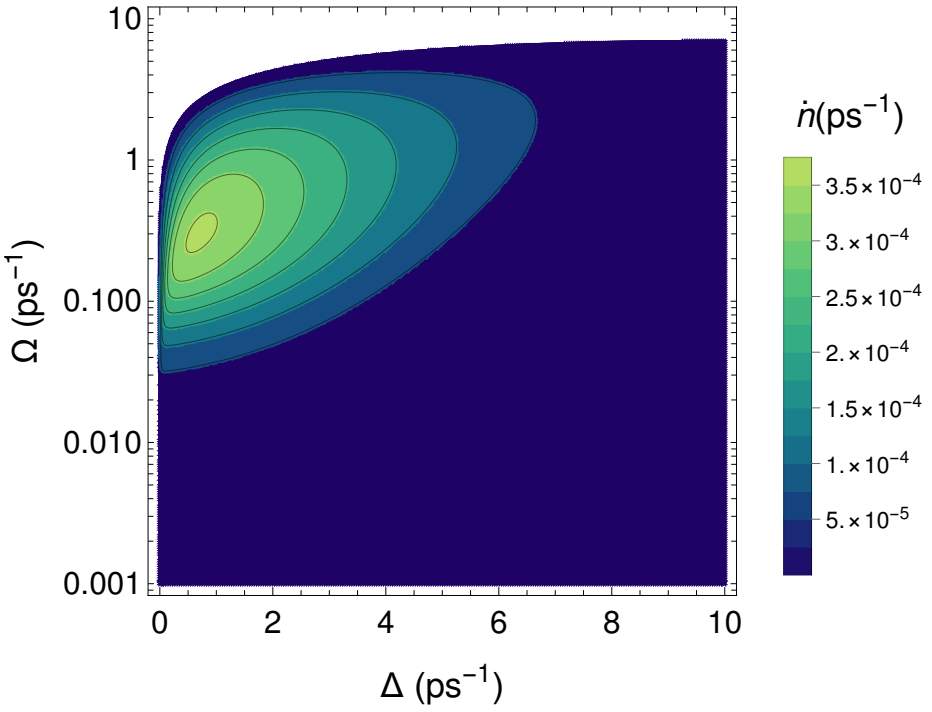

Figure 4.2: Phonon absorption rate as a function of both detuning Δ and Rabi frequency Ω.

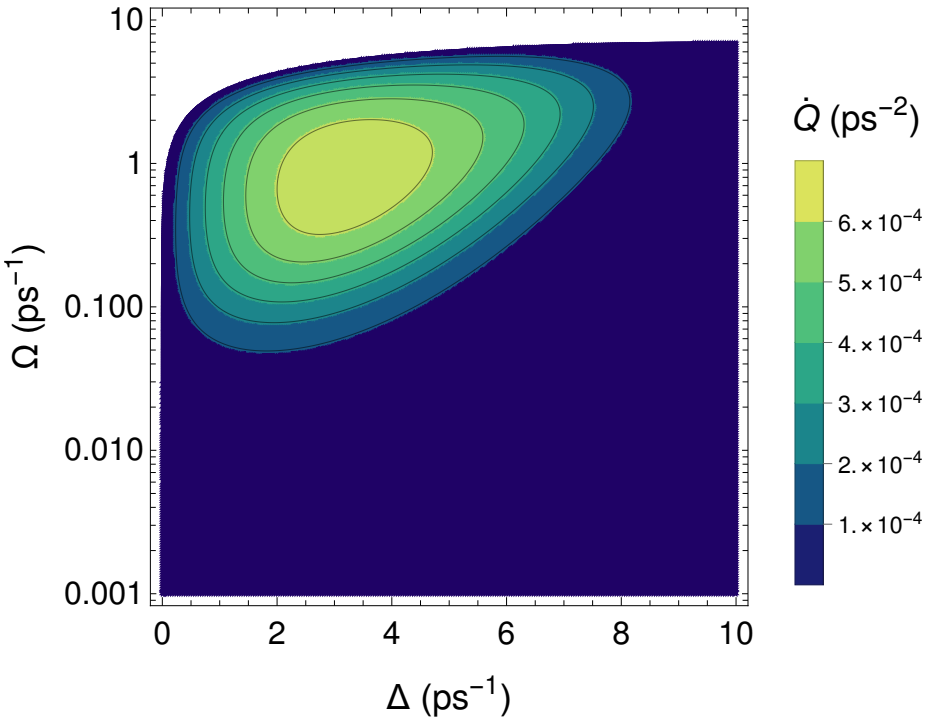

Figure 4.3: Heat absorption rate as a function of both detuning Δ and Rabi frequency Ω.

creasing driving strength. Also seen in this plot is the corresponding heating effect, for negative detuning, as is expected for blue detuned laser driving. This broadening is a consequence of the difference between the rate of transitions $|+\rangle \rightarrow |-\rangle$ and transitions $|-\rangle \rightarrow |+\rangle$, induced by the photon emission. In eqn. 4.18, the numerator can be

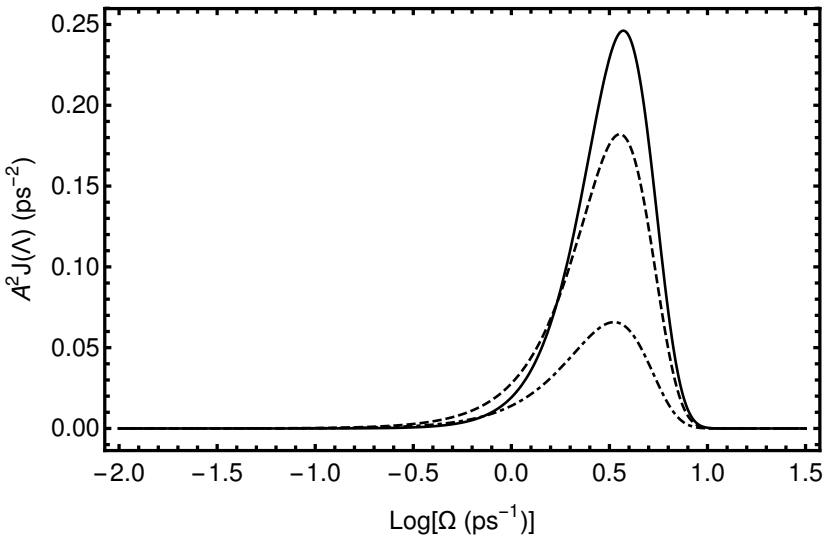

Figure 4.4: $A^2J(\Lambda)$ as a function of Rabi frequency, Ω, for $\Delta = 0$ ps^{-1} (solid), ± 2 ps^{-1} (dashed) and ± 4 ps^{-1} (dot-dashed)

written as

$$\pi A^2 J^{\text{phon}}(\Lambda)\gamma_0' \left(B_+(n(\Lambda)) - B_-(n(\Lambda)+1)\right). \tag{4.23}$$

The phonon scattering rates are proportional to $A = (\Omega/2\Lambda)^2$. As the driving strength is increased, this factor is significant over a greater range of detunings, as can be seen from fig. 4.6(a). The photon scattering rates are proportional to $B_\pm = ((\Delta \pm \Lambda)/2\Lambda)$, for the transition from upper to lower/lower to upper dressed state. These factors are asymmetric and identical, differing only by a reflection about the y-axis, as seen in fig. 4.6(b). Plotting $A^2J(\Lambda)B_\pm$ in fig. 4.6(b), we can see the result is finite heat power, either side of $\Delta = 0$. The role of the Bose occupation factors then introduces some asymmetry, with the maximum heating rate larger than the maximum cooling rate. We emphasise these features here, where they are easier to understand in this simple two level model. We will again see these same features in chapter 5, when we consider the more complicated heat absorption due to a driven SiV center.

We plot the maximum heat current as a function of the temperature of the phonon reservoir in fig. 4.7. The cooling power increases monotonically with increasing phonon temperature, and reduces to a current of 0 ps^{-2} as the phonon temperature approaches 0 K.

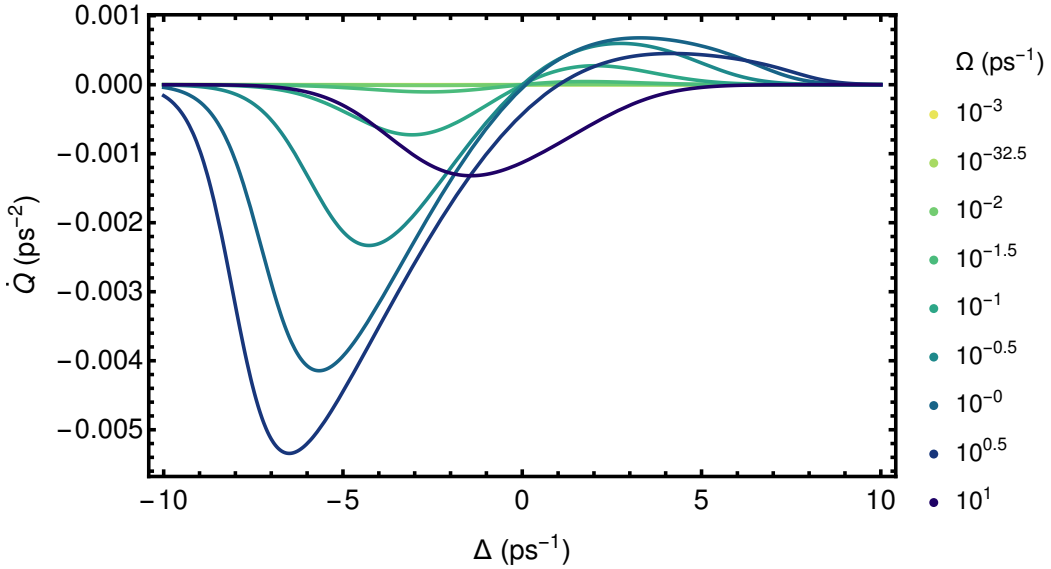

Figure 4.5: Heat absorption spectrum for the driven quantum dot

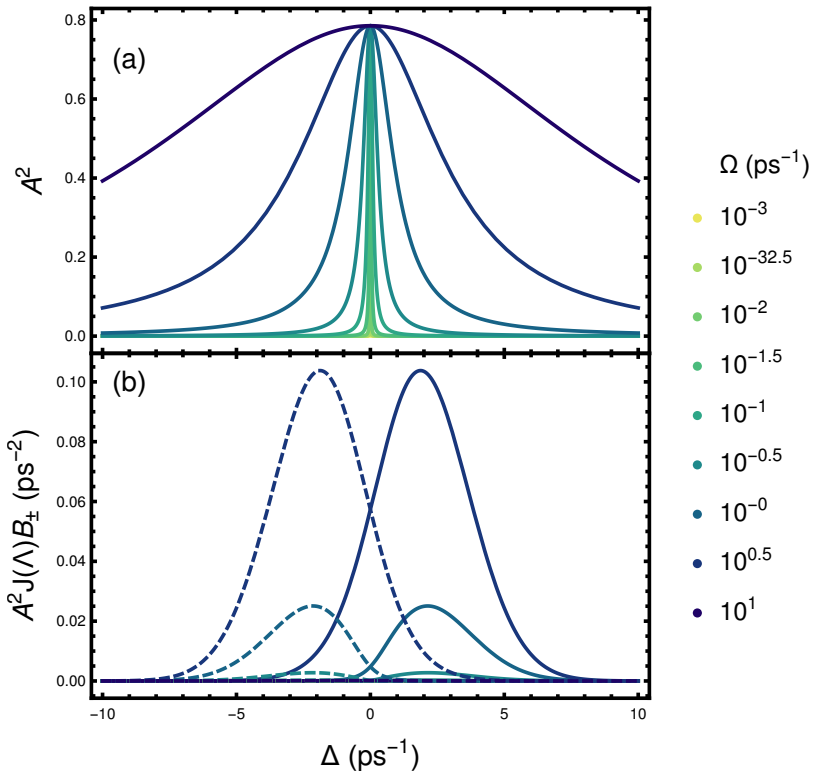

Figure 4.6: (a)$A^2 = (\Omega/2\Lambda)^2$ as a function of Δ for increasing Rabi frequencies. (b) $A^2 J(\Lambda) B_+$ (solid) and $A^2 J(\Lambda) B_-$ (dashed) as functions of Δ for increasing Rabi frequencies.

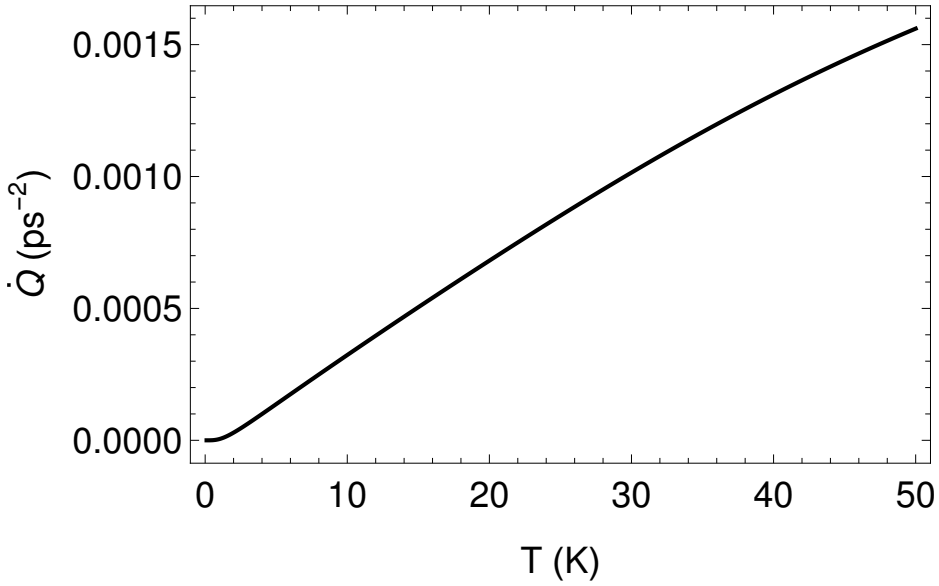

Figure 4.7: Maximum heat absorption power as a function of the phonon temperature

4.2 Statistics of the Steady State Driving model

4.2.1 Full Counting Statistics

Using the method of full counting statistics, we can calculate the probability distribution for the heat transferred between the exciton and each bath. In this case, the probability distribution is a function of two heat variables, one for each bath. This involves repeating the derivation for the counting field master equation, however we now introduce two counting field phase factors, $e^{iuH_B^{\text{phon}}}$ and $e^{ivH_B^{\text{phot}}}$. The exact same derivation can in principle be carried out, however a simpler approach can be used in the steady state model. With a constant dressed state splitting, we can instead count for the number of jumps between the dressed states that are induced by the coupling between the system and each bath, a discrete quantity. For the case of phonons, the net number of jumps from lower to upper dressed state is then simply the number of phonons absorbed. The corresponding heat absorption from the phonons is $\Lambda\langle n\rangle$, where n is the number of phonons absorbed by the exciton.

The heat emitted as photons is a little more subtle. Since we neglected terms proportional to $n(\omega_l)$ in the dissipator, in reality only photon emission occurs, and no photon absorption ever takes place. However, as we saw in the master equation, when the dissipation due to the phonons is written in the basis of laser dressed states, the photon emission can lead to jumps $|+\rangle \to |-\rangle$ and to jumps $|-\rangle \to |+\rangle$. A jump from $|+\rangle$ to $|-\rangle$ involves the net emission of an amount of heat equal to $\omega_l + \Lambda$, with a jump $|-\rangle$ to $|+\rangle$ involving the emission of an amount of heat equal to $\omega_l - \Lambda$. For a total number of photons emitted N, we can decompose this into $N = N_+ + N_-$, with $N_\pm$ denoting the number of emission event associated with a jump up/down in the dressed state basis. The total heat emitted into the photon bath is then

$$Q = N_-(\omega_l + \Lambda) + N_+(\omega_l - \Lambda) = N\omega_l + (N_- - N_+)\,\Lambda.$$

This quantity $(N_- - N_+)\,\Lambda$ is the excess heat emitted into the photons, that was absorbed from the phonon reservoir. Counting the number of net number of jumps from upper to lower dressed state due to the scattering with the photons does not in fact count the number of photons emitted, but instead counts this excess heat that is emitted into the photon bath, which is the quantity we are looking to quantify.

To count such jumps between the dressed states, we partition that state of the dot as

$$\hat{\rho}(t) = \sum_{n,m} \hat{\rho}_{n,m}(t) \tag{4.24}$$

with $\hat{\rho}_{n,m}(t)$ the state of the dot in the subspace where there have been n phonons absorbed (n net upwards jumps in the basis of dressed states) and there has been m

net downward jumps induced by the photon emission. The master equation can be written by inspection as

$$\begin{aligned}
\dot{\rho}_{n,m}(t) = &- i\left[H_S, \rho_{n,m}(t)\right] \\
&- \left(\frac{\Omega}{2\Lambda}\right)^2 \gamma_0(\Lambda)\left(n(\Lambda)+1\right)\left[R_+R_-\rho_{n,m}(t) + \rho_{n,m}(t)R_+R_- - 2R_-\rho_{n-1,m}(t)R_+\right] \\
&- \left(\frac{\Omega}{2\Lambda}\right)^2 \gamma_0(\Lambda)n(\Lambda)\left[R_-R_+\rho_{n,m}(t) + \rho_{n,m}(t)R_-R_+ - 2R_+\rho_{n+1,m}(t)R_-\right] \\
&- \left(\frac{\Delta+\Lambda}{2\Lambda}\right)^2 \gamma_0'\left[R_+R_-\rho_{n,m}(t) + \rho_{n,m}(t)R_+R_- - 2R_-\rho_{n,m+1}(t)R_+\right] \\
&- \left(\frac{\Delta-\Lambda}{2\Lambda}\right)^2 \gamma_0'\left[R_-R_+\rho_{n,m}(t) + \rho_{n,m}(t)R_-R_+ - 2R_+\rho_{n,m-1}(t)R_-\right] \\
&- \left(\frac{\Omega}{\Lambda}\right)^2 \gamma_0'\left[R_zR_z\rho_{n,m}(t) + \rho_{n,m}(t)R_zR_z - 2R_z\rho_{n,m}(t)R_z\right]. \qquad (4.25)
\end{aligned}$$

The initial condition is $\rho(0)_{n,m} = \delta_{n,0}\delta_{m,0}\left|0\right\rangle\left\langle 0\right|$. A similar master equation was considered in [121], where only the phonons were counted.

These coupled master equations have a simple interpretation. The state is taken from $\rho_{n,m}$ to $\rho_{n+1,m}$ when a phonon is absorbed and to $\rho_{n-1,m}$ when a phonon is emitted. Similarly, for the photons, the state is taken from $\rho_{n,m}$ to $\rho_{n,m+1}$ when a transition from $\left|-\right\rangle \rightarrow \left|+\right\rangle$ occurs due to the emission of a photon, and to $\rho_{n,m+1}$ when a transition from $\left|+\right\rangle \rightarrow \left|-\right\rangle$ occurs due to the emission of a photon.

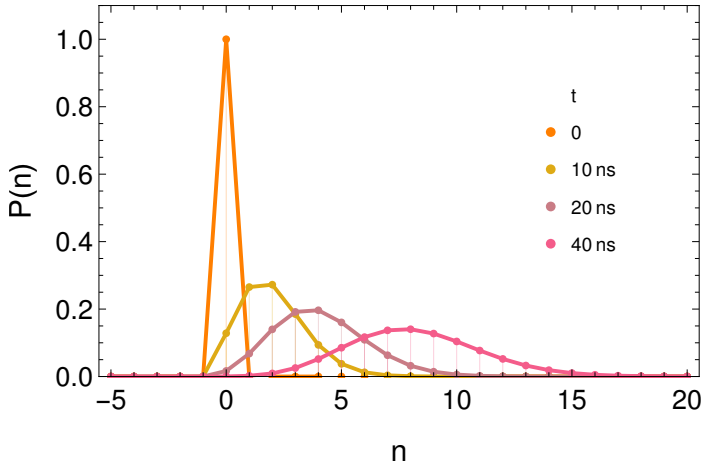

Figure 4.8: Probability distribution for absorbing n phonons after a time t has elapsed, with $\Delta = 3.22\ \mathrm{ps}^{-1}$ and $\Omega = 0.84\ \mathrm{ps}^{-1}$.

We first consider only the probability distribution for absorbing n phonons. This distribution is plotted for a set of times in fig. 4.8. This distribution appears to be Gaussian at the later times shown, with a mean shifting in time.

We now consider the full probability distribution $P(n,m)$, for absorbing n phonons and for m net photon induced downward transitions. Fig. 4.9 is a plot of this distribution

with $\Delta = 3.22$ ps^{-1} and $\Omega = 0.84$ ps^{-1} (the values for which the heat absorption power is maximal) after a time $t = 40$ ns has elapsed. This distribution is supported over a small region close to $m = n$. In fact, this distribution is entirely supported over the three lines $m = n$, $m = n + 1$ and $m = n - 1$. We can define a weight $A_i = \sum_n P(n, n+i)$, the total weight of the distribution along the subspace $m = n+i$. Fig. 4.10 is a plot of the distribution function over these three lines, $m = n$, $m = n+1$ and $m = n-1$, at the same point in time, $t = 40$ ns. Most of the weight is retained in $m = n$ subspace, with the least amount of weight in $m = n + 1$ subspace. In fig. 4.11, we plot the weight of the distribution in each of these subspaces and the rate of change of these weights as functions of time. The distribution spreads to these three lines quickly, before settling at a steady value after about 150 ps, where the weights remain constant.

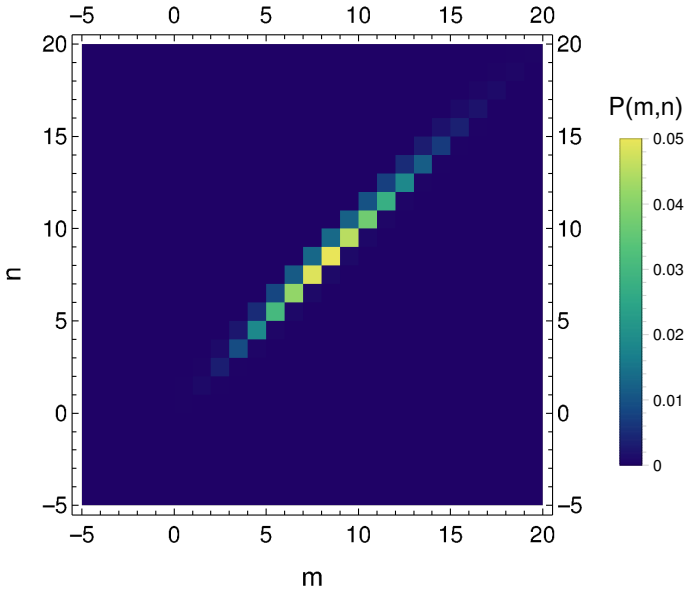

Figure 4.9: Probability distribution for absorbing n phonons and for m net photon induced downward transitions after a time $t = 40$ ns for $\Delta = 3.22$ ps^{-1} and $\Omega = 0.84$ ps^{-1}.

In fig. 4.12 (b) we plot the mean phonon absorption rate and the mean rate of photon induced downward transitions. Immediately, as the system is pumped, the phonon absorption rate is high, dropping quickly to its steady state value. This high initial phonon absorption rate is due to the initial heating of the exciton to its steady state. After $\sim$ 150 ps, the system reaches its steady state heat pumping rate. Plotting the mean number of phonons absorbed and the mean number of net photon induced downward transitions in fig. 4.12 (a), the heating energy is clear here. We see a finite gap between the curves, which remains constant once the system enters the steady state heat pumping regime. This value of heat is simply $Q = \mathrm{Tr}\left[H_S\left(\rho_{ss} - \rho_0\right)\right]$.

In fig. 4.12 (c) we plot the rate of change of the variance of the number of phonons absorbed, and the rate of change of the variance of the number of photon induced net

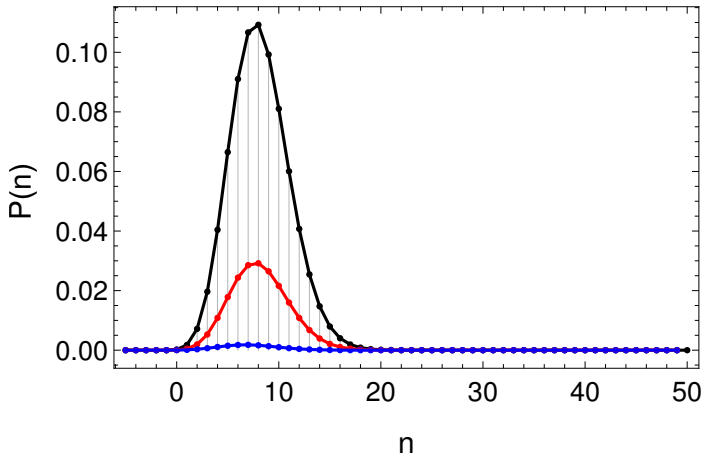

Figure 4.10: The probability distribution for absorbing n phonons and for m net photon induced downward transitions, for $m = n$ (black), $m = n + 1$ (blue) and $m = n - 1$ (red), for $\Delta = 3.22$ ps^{-1} and $\Omega = 0.84$ ps^{-1}.

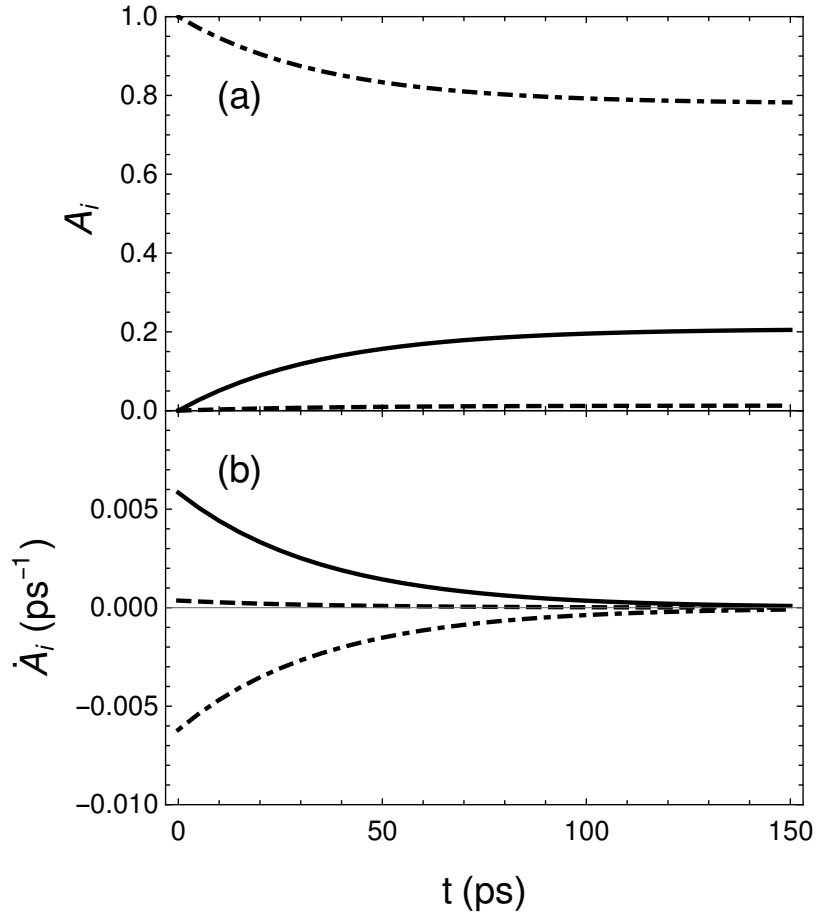

Figure 4.11: (a) The total weights A_i in the subspace $n = m$ (dot-dashed), $n = m + 1$ and $m = n + 1$ (dashed) (solid) for driving parameters $\Delta = 3.22$ ps^{-1} and $\Omega = 0.84$ ps^{-1}. (b) The rate of change of these weights A_i.

downward transitions. We see that in both cases, the variance varies linearly with time, indicating normal diffusive behaviour for the heat pumping statistics. We also plot the

covariance, in 4.12 (d). Here we see that the covariance function also increases linearly in time at steady state, as expected.

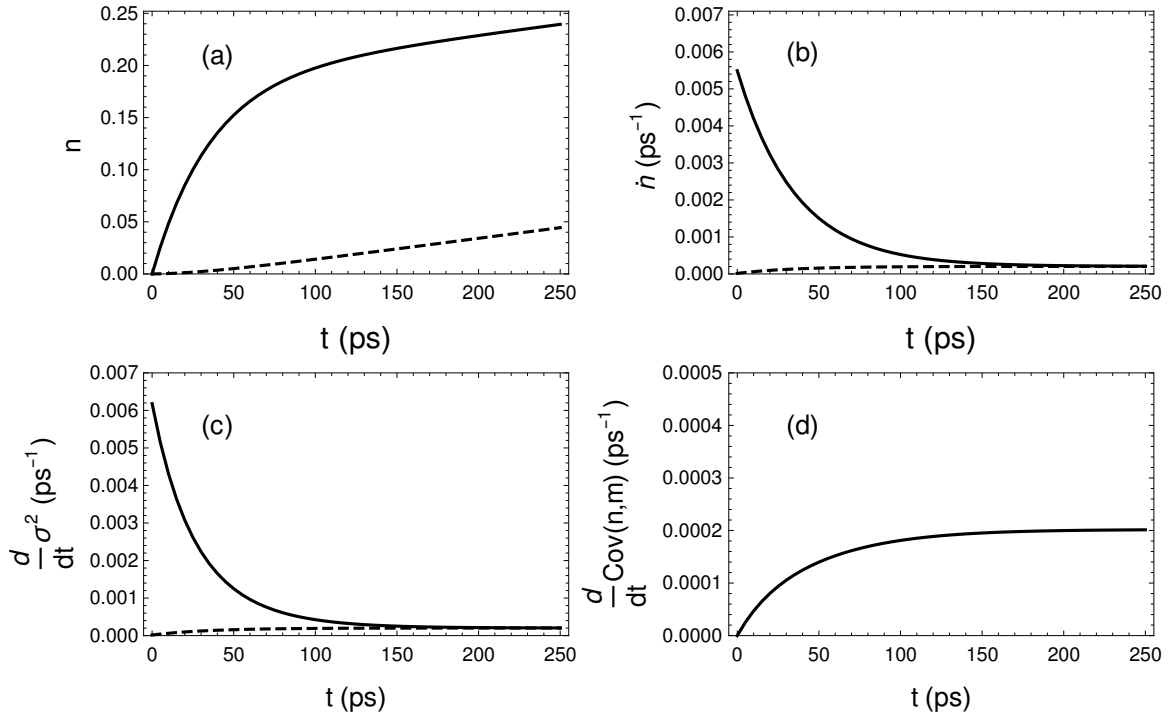

Figure 4.12: (a) The mean number of phonons absorbed (solid) and photon induced downward transitions (dashed). (b) The rate of phonons absorbed (solid) and photon induced downward transitions (dashed). (c) The rate of change of the variance of the number of phonons absorbed (solid) and photon induced downward transitions emitted (dashed). (d) The rate of change of the covariance of the probability distribution $P_{n,m}$.

4.3 Conclusions

Simplifying the laser to that of a steady state continuous wave optical excitation of a quantum dot exciton, we examined the steady state heat pumping from the phonons as considered in [121]. Writing a master equation for the exciton-phonon-photon system, with both exciton-phonon and exciton-photon scattering written in the basis of laser dressed state, we were able to analytically solve for the steady state of the exciton. From these expressions, it was trivial to write down an analytical expression for the power of the heat absorption from the phonon reservoir. These expressions clearly explained the basic requirements on the driving parameters that need to be satisfied in order for cooling to be sustained.

Moving beyond the mean heat exchanged between the exciton and the phonons, we use the method of full counting statistics to compute the full probability distribution for the number of phonons absorbed and the net number of photon induced transitions from upper to lower dressed state, a quantity which we related to the excess heat pumped into the photon reservoir. This distribution quickly seemed to converge to a Gaussian structure, with a mean which shifted linearly in time, with higher order moments also displaying a linear dependence on time.

5 Laser Cooling of Silicon Vacancy Centres in Diamond

In this chapter, we extend the theory of steady state heat absorption of a laser driven quantum dot exciton, to a laser driven silicon vacancy (SiV) centre in diamond. Although pumping heat from the phonons into the electromagnetic environment was indeed possible, background absorption of the laser by the host medium will result in a heating effect which will offset any potential cooling [121]. To implement a similar heat pumping protocol which realises practical laser cooling of a solid and that can sustain robust and powerful cooling, we then need to consider systems which don't suffer from the high background absorption effects. Optically active defects in diamond offer the perfect platform to implement such a protocol. The absorption coefficient in diamond is less than 0.1 cm^{-1} [127] for the energy scales considered in this chapter. Such a small absorption coefficient results in minimal background heating due to the background laser, which is crucial when we consider the competing effects of the heat absorption from the phonons and the background heating due to the driving laser. The atomic scale extent of the defects allows for high densities of optically active centres, increasing the net cooling power per vacancy.

Unlike quantum dot excitons we have considered so far, these optically active defects typically have a more complicated level structure. In this chapter, we specifically discuss the use of silicon vacancy centres, formed from an interstitial silicon impurity and two carbon vacancies. This system typically has eight relevant electronic states [128], with four states in an excited state manifold, and four states in a ground state manifold. This is already more complicated than the two level approximation used for modelling quantum dot excitons, without yet considering the coupling of the charge to the phonons. The electronic degrees of freedom are coupled to the phonons through the same deformation potential coupling, but also through an intra-manifold coupling mechanism.

We will first introduce the silicon vacancy centre and the Hamiltonian describing the laser driven electronic degrees of freedom, before introducing the coupling to the phonons. We once again discuss in detail the master equation we use to describe this system, discussing the role of the secular approximation in such cooling proto-

cols, and write down a counting field variant for the non-secular Born-Markov master equation.

Using these tools, we will analyse the cooling spectra, discussing the changes we see as we cross over from weak driving to strong driving. We again interpret these results using the concept of laser dressed states, and identify the mechanisms which lead to more robust cooling protocols in the strong driving regime. Lastly, we will compare the cooling spectra for the non-secular Born-Markov model, the secular Born-Markov model and a simple phenomenological model. We will show that the non-secular Born-Markov theory accurately models the cooling spectra in the weak driving limit where it agrees with the phenomenological Lindblad model, and in the strong driving regime where it agrees with the secular Born-Markov theory.

5.1 Silicon Vacancy Centre Defects in Diamond

Silicon vacancy centres in diamond are defects composed of an interstitial silicon atom, two neighbouring carbon vacancies and a further six carbon atoms, as depicted in fig. 5.1. In the absence of any interaction with that host lattice or the electromagnetic environment, the undriven SiV centre has twelve electronic levels, filled with eleven electrons, and so it is best modelled as a single hole system. Of these twelve levels, eight are relevant for the cooling protocol considered here, with a set of four states in a ground state manifold, typically denoted

$$|g_x,\uparrow\rangle\,,|g_x,\downarrow\rangle\,,|g_y,\uparrow\rangle\,,|g_y,\downarrow\rangle\,,$$

and a set of four states which form the excited state manifold, denoted

$$|u_x,\uparrow\rangle\,,|u_x,\downarrow\rangle\,,|u_y,\uparrow\rangle\,,|u_y,\downarrow\rangle\,.$$

The ground and excited state manifolds are split by an energy $E_G = 1.68$ eV [128].

Within each manifold, the levels are split due to a spin orbit coupling effect. The overall result of the spin-orbit coupling results in a set of states in the excited manifold,

$$|g_+,\uparrow\rangle\,,|g_-,\downarrow\rangle\,,|g_-,\uparrow\rangle\,,|g_+,\downarrow\rangle$$

and states

$$|u_+,\uparrow\rangle\,,|u_-,\downarrow\rangle\,,|u_-,\uparrow\rangle\,,|u_+,\downarrow\rangle\,.$$

in the ground state manifold, with $|u_+\rangle = -\left(|u_x\rangle + i\,|u_y\rangle\right)$ and $|u_-\rangle = |u_x\rangle - i\,|u_y\rangle$, with the same decomposition for $|g_+\rangle$ and $|g_-\rangle$. Fig. 5.2 depicts the energy level structure for both the spin up subspace and spin down subspace, with the spin orbit splitting in each manifold indicated. Note, the scale of the splitting between the upper and lower

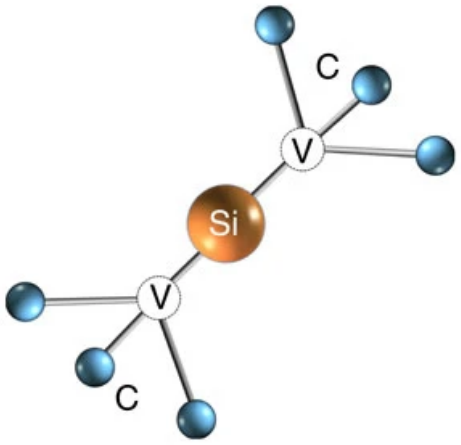

Figure 5.1: Schematic of the silicon vacancy centre atomic structure from [129]. Six carbon atoms (blue), two carbon vacancies and an interstitial silicon atom (yellow).

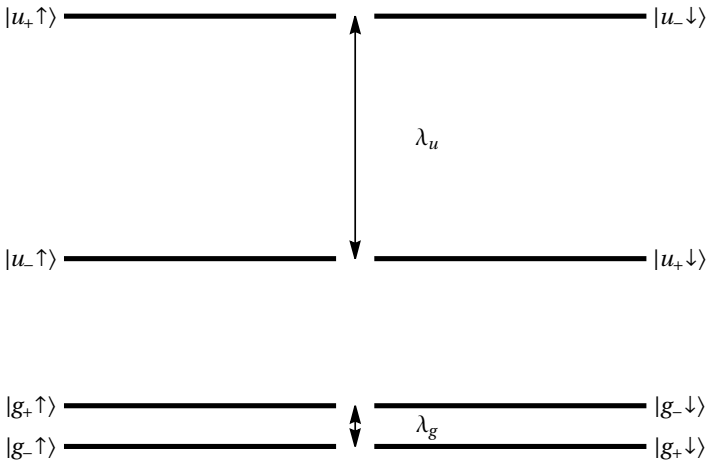

Figure 5.2: Eight level structure for of the SiV centre. Each manifold is split by a spin-orbit coupling constant $\lambda_{u/g}$.

manifold is shrunk for clarity in the schematic. Both level structures are identical, with a spin orbit splitting in the excited state manifold given by $\lambda_u = 260$ GHZ and a spin orbit splitting in the ground state manifold of $\lambda_g = 50$ GHZ [128]. The only difference between the level structure in each subspace is the ordering of the levels within a manifold. Note, we neglect a dynamic Jahn-Teller perturbation in the Hamiltonian for the SiV. This term has coupling constants of order 4% of the spin-orbit coupling, and so does not have any significant effect on the physics of the cooling protocol we present [128]. Since we do not consider any spin flipping interactions or external magnetic fields, it is best at this point to work in the spin up subspace, where we now have a simpler four level structure. Later, we discuss how the cooling in one spin sector is identical to the cooling in the other, through a simple change in the polarisation of the driving laser.

The Hamiltonian for this undriven system in the spin up subspace is then of the

form

$$\begin{aligned}\hat{H}_0 = \frac{1}{2}\Big[&+ (E_G + \lambda_u)\,|u_+\rangle\langle u_+| \\ &+ (E_G - \lambda_u)\,|u_-\rangle\langle u_-| \\ &- (E_G - \lambda_g)\,|g_+\rangle\langle g_+| \\ &- (E_G + \lambda_g)\,|g_+\rangle\langle g_+|\Big]. \end{aligned} \tag{5.1}$$

We can perform a unitary transformation to a frame rotating at the laser frequency, using $U = \exp\big(+i\omega_l t/2\big[\,|u_+\rangle\langle u_+| + |u_-\rangle\langle u_-| - |g_+\rangle\langle g_+| - |g_-\rangle\langle g_-|\,\big]\big)$. In this frame, the Hamiltonian becomes

$$\begin{aligned}\hat{H}_0 = \frac{1}{2}\Big[&+ (\Delta + \lambda_u)\,|u_+\rangle\langle u_+| \\ &+ (\Delta - \lambda_u)\,|u_-\rangle\langle u_-| \\ &- (\Delta - \lambda_g)\,|g_+\rangle\langle g_+| \\ &- (\Delta + \lambda_g)\,|g_+\rangle\langle g_+|\Big], \end{aligned} \tag{5.2}$$

where again we define the detuning, $\Delta = E_G - \omega_l$.

We include the effect of the driving laser, by adding a term $-\vec{d}.\vec{E}$ to the Hamiltonian. With the dipole operators $\hat{d}_x$, $\hat{d}_y$ and $\hat{d}_z$ given in the basis of $\big|(u/g)_{(x/y)}\big\rangle$ in [128], we instead use the dipole operators $\hat{d}_+$, $\hat{d}_-$ and $\hat{d}_z$, where $\hat{d}_\pm$ is the dipole operator for right/left circularly polarised light, defined as $\hat{d}_\pm = \frac{1}{2}\left(\hat{d}_x \pm i\hat{d}_y\right)$. We can expand these dipole operators in the basis of the spin-orbit states as

$$\hat{d}_+ = \langle g_+|\,\hat{d}_+\,|u_-\rangle\,|g_+\rangle\langle u_-| + \text{h.c} \tag{5.3}$$

$$\hat{d}_- = \langle g_-|\,\hat{d}_-\,|u_+\rangle\,|g_-\rangle\langle u_+| + \text{h.c} \tag{5.4}$$

$$\hat{d}_z = \langle g_-|\,\hat{d}_z\,|u_-\rangle\,|g_-\rangle\langle u_-| + \langle u_+|\,\hat{d}_z\,|g_+\rangle\,|u_+\rangle\langle g_+| + \text{h.c} \tag{5.5}$$

Fig. 5.3 shows the level structure for each spin sector, with the optical driving for each polarisation indicated by arrows. It is clear from this schematic that driving with σ_- polarised light in one spin sector, at some frequency ω, has the same effect as driving with σ_+ polarised light in the other spin sector, and vice versa. We can take advantage of this fact later in the proposed cooling protocol, developing the theory in one spin sector and porting the results over to the other spin sector with the appropriate change of polarisation for the driving. Pumping with σ_z polarised light has the same effect in both spin sectors.

In the spin up subspace, we can write the Hamiltonian in the rotating frame and with the rotating wave approximation as

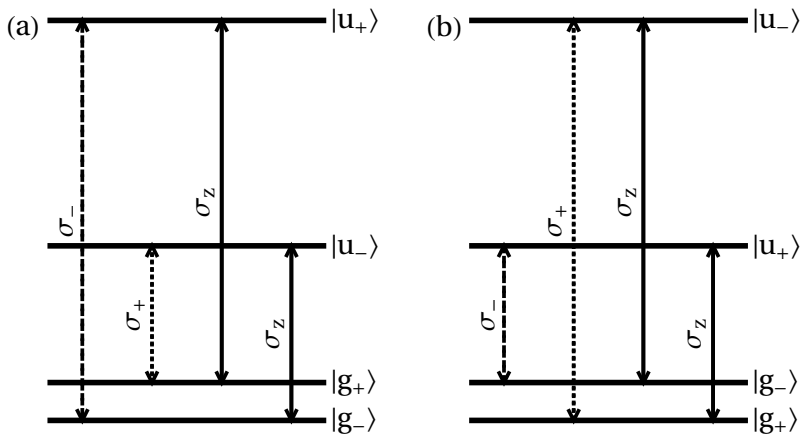

Figure 5.3: SiV level scheme, indicating the pairs of levels which each driving polarisation couples together in the (a) spin up and (b) spin down sector.

$$\hat{H}_{\mathrm{SiV}} = \frac{1}{2}\begin{pmatrix} \Delta+\lambda^u & \Omega_z & \Omega_- & 0 \\ \Omega_z & -\Delta-\lambda^g & 0 & \Omega_+ \\ \Omega_- & 0 & -\Delta+\lambda^g & \Omega_z \\ 0 & \Omega_+ & \Omega_z & \Delta-\lambda^u \end{pmatrix}, \tag{5.6}$$

where the Rabi frequencies are expressed as $\Omega_i = \langle g_\pm | \, \hat{d}_i \cdot \vec{E} \, | u_\pm \rangle$, with $i \in (+,-,z)$, and levels are ordered as

$$a\,|u_+\rangle + b\,|g_+\rangle + c\,|g_-\rangle + d\,|u_-\rangle = \begin{pmatrix} a \\ b \\ c \\ d \end{pmatrix}. \tag{5.7}$$

The electronic degrees of freedom of the SiV centre couple to the acoustic phonon modes of the lattice through two mechanisms, an intramanifold coupling mechanism [130]

$$\hat{H}_I^{\mathrm{intra}} = \sum_k \left(f_k^u \, |u_+\rangle \langle u_-| + f_k^g \, |g_+\rangle \langle g_-| \right) \otimes a_k + \mathrm{h.c}, \tag{5.8}$$

and through a deformation potential coupling mechanism [131, 132],

$$\begin{aligned} \hat{H}_I^{\mathrm{def}} = \sum_k g_k \big(&|u_+\rangle \langle u_+| + |u_-\rangle \langle u_-| - \\ &|g_+\rangle \langle g_+| - |g_-\rangle \langle g_-| \big) \otimes \left(a_k + a_k^\dagger \right). \end{aligned} \tag{5.9}$$

The intramanifold phonon interaction term describes transitions between the states in a given manifold, along with the associated emission or absorption of phonons. The deformation potential coupling term describes a local deformation of the lattice when the SiV centre is in an excited state. Together with the driven system Hamiltonian,

this Hamiltonian describes, in full, the dynamics of the electronic degrees of freedom and the phononic modes.

We use a spectral density of the form $J(\omega) = 2A\omega_c^{-2}\omega^3 e^{-\omega/\omega_c}$, with $A = 0.0275$ and $\omega_c = 2\pi \text{ps}^{-1}$, for the deformation potential coupling term [131, 132]. It is important to note here that in the spectral density, we only use the bulk phonon contribution. There are also higher energy local phonon modes, which results in a peaked structure in the spectral density [131]. These peaks lie at higher energies than considered in this work, and as such will not affect our results. For the intramanifold interaction, we use a spectral density $A\omega^3 e^{-\omega/\omega_c}$, as used in [130], with $A = 0.0037$ ps^2 and with the same cut off frequency as above. For simplicity, we make the assumption that the $f_k^u = f_k^g$, i.e., that the intramanifold interaction strengths are identical in each manifold.

5.2 Driven SiV centre Master Equation

With the added levels in the system Hamiltonian, and the addition of new system bath interaction mechanisms as compared to the work on quantum dot excitons, it is more tedious and less instructive to derive a master equation by hand. Here, we outline the method we use to generate the master equation numerically. We will show how to use this method to derive both the corresponding secular Bloch-Redfield master equation, as well as the non-secular Bloch-Redfield master equation, which is needed in the case of a driven system with degenerate or nearly degenerate states.

Standard master equation

Our approach follows the standard method, detailed for example in [92]. We begin by treating the Hamiltonian for the full system plus bath in the usual partition into free and coupling Hamiltonian terms,

$$\hat{H} = \hat{H}_S + \hat{H}_B + \hat{H}_{SB} \tag{5.10}$$

$$, \hat{H}_{SB} = \sum_k g_k \hat{O}(\hat{b}_k + \hat{b}_k^\dagger), \tag{5.11}$$

where $\hat{O}$ here is the system operator of the total system bath coupling Hamiltonian. Working in the interaction picture with regard to $\hat{H}_S + \hat{H}_B$, we have an interaction picture Hamiltonian,

$$\tilde{H}_{SB}(t) = \sum_k g_k \tilde{O}(t)(\hat{b}_k e^{-i\omega_k t} + \hat{b}_k^\dagger e^{i\omega_k t}), \tag{5.12}$$

with $\tilde{O}(t) = e^{i\hat{H}_S t}\hat{O}e^{-i\hat{H}_S t}$. We perform the usual iteration of the von Neumann equation, which gives the second-order form

$$\frac{d\rho(t)}{dt} = -\int^t dt'[\tilde{H}_{SB}(t), [\tilde{H}_{SB}(t'), \rho_S(t)\otimes\rho_B]]. \tag{5.13}$$

In this step, we have made the Markov approximation by replacing $\rho(t')$ with $\rho_S(t)\otimes\rho_B$ in the final term, where $\rho_S(t)$ is the reduced density matrix of the system. Expanding this and taking the trace over bath modes gives

$$\begin{aligned}\frac{d\rho}{dt} = -\sum_k g_k^2\big\{&[(n+1)e^{i\omega(t'-t)} + ne^{-i\omega(t'-t)}][\tilde{O}(t)\tilde{O}(t')\rho_S(t) - \tilde{O}(t')\rho_S(t)\tilde{O}(t)] \\ &+[(n+1)e^{-i\omega(t'-t)} + ne^{i\omega(t'-t)}][\rho_S(t)\tilde{O}(t')\tilde{O}(t) - \tilde{O}(t)\rho_S(t)\tilde{O}(t')]\big\}.\end{aligned} \tag{5.14}$$

From here it is useful to expand the system operator $\hat{O}$ in terms of the eigenstates of the driven system Hamiltonian, $\hat{H}_S$, $|i\rangle$ with energies E_i,

$$\hat{O} = \sum_{ij} \langle i|\hat{O}|j\rangle |i\rangle\langle j| = \sum_{ij}\hat{O}_{j\to i}, \tag{5.15}$$

$$\implies \tilde{O}(t) = \sum_{ij} e^{i(E_i-E_j)t}\langle i|\hat{O}|j\rangle |i\rangle\langle j| = \sum_{ij}\tilde{O}_{j\to i}(t). \tag{5.16}$$

The operators $\hat{O}_{j\to i}$ and $\tilde{O}_{j\to i}(t)$ are simply the parts of the operator $\hat{O}$ which cause a transition from j to i when they act to the right.

Using this representation in eqn. (5.16) allows us to do the integrals over t' in (5.14). Picking out the relevant terms, we have

$$\int^t dt' e^{\pm i\omega t' + i(E_i-E_j)t'} = \frac{e^{\pm i\omega t + i(E_i-E_j)t}}{\pm i\omega + i(E_i-E_j) + \epsilon}, \tag{5.17}$$

where ϵ is an infinitesimal whose sign we decide later. Inserting these integrals in eqn. (5.14) gives

$$\begin{aligned}\frac{d\rho}{dt} = -\sum_k\sum_{ij} g_k^2\Bigg\{&\left[\frac{n+1}{i\omega + i(E_i-E_j)+\epsilon} + \frac{n}{-i\omega + i(E_i-E_j)+\epsilon}\right] \\ &\times\left[\tilde{O}(t)\tilde{O}_{j\to i}(t)\rho_S(t) - \tilde{O}_{j\to i}(t)\rho_S(t)\tilde{O}(t)\right] \\ &+\left[\frac{n+1}{-i\omega + i(E_i-E_j)+\epsilon} + \frac{n}{i\omega + i(E_i-E_j)+\epsilon}\right] \\ &\times\left[\rho_S(t)\tilde{O}_{j\to i}(t)\tilde{O}(t) - \tilde{O}(t)\rho_S(t)\tilde{O}_{j\to i}(t)\right]\Bigg\}.\end{aligned} \tag{5.18}$$

Replacing the sum over bath modes with an integral over a spectral density, $J(\omega) =$

$\sum_k g_k^2 \delta(\omega - \omega_k)$, and using the identity

$$\lim_{\epsilon \to 0^+} \frac{1}{ix \mp \epsilon} = \mp \pi \delta(x) - i\mathcal{P}\frac{1}{x},$$

we can perform the integral. The principal value term gives rise to a Hamiltonian term in the dynamics. It results in a Lamb shift renormalisation of the unperturbed levels of the system due to the system-bath coupling [92]. The other part gives the dissipative terms, which we write

$$\begin{aligned}\frac{d\rho}{dt} = -\pi \sum_{ij} \Big\{ &[(n+1)J(E_j - E_i) + nJ(E_i - E_j)] \left[\tilde{O}(t)\tilde{O}_{j\to i}(t)\rho_S(t) - \tilde{O}_{j\to i}(t)\rho_S(t)\tilde{O}(t)\right] \\ &+ [(n+1)J(E_i - E_j) + nJ(E_j - E_i)] \left[\rho_S(t)\tilde{O}_{j\to i}(t)\tilde{O}(t) - \tilde{O}(t)\rho_S(t)\tilde{O}_{j\to i}(t)\right] \Big\}\end{aligned} \tag{5.19}$$

The sign of ϵ is chosen such that we get back the correct dissipator, in particular one in which the jump terms $O\rho O$ have a positive prefactor. This master equation, as it stands, is non-secular.

Substituting in eqn. 5.16 for $\tilde{O}(t)$, terms in eqn. 5.19 will contain terms of the form

$$\begin{aligned}\frac{d\rho}{dt} = -\pi \sum_{ij} \sum_{mn} \Big\{ &[(n+1)J(E_j - E_i) + nJ(E_i - E_j)] \times \\ &\left[\tilde{O}_{m\to n}(t)\tilde{O}_{j\to i}(t)\rho_S(t) - \tilde{O}_{j\to i}(t)\rho_S(t)\tilde{O}_{m\to n}(t)\right] \\ &+ [(n+1)J(E_i - E_j) + nJ(E_j - E_i)] \times \\ &\left[\rho_S(t)\tilde{O}_{j\to i}(t)\tilde{O}_{m\to n}(t) - \tilde{O}_{m\to n}(t)\rho_S(t)\tilde{O}_{j\to i}(t)\right] \Big\}\end{aligned}$$

The product of operators $\tilde{O}_{j\to i}(t)\tilde{O}_{m\to n}(t)$ will have a phase factor $e^{i(E_i - E_j)t}e^{i(E_n - E_m)t}$. The secular approximation amounts to discarding all such terms for which the oscillating phase factors do not cancel out. In a system without degenerate states, this simply amounts to taking the operators $\tilde{O}(t)$ in eqn. 5.19 to be the Hermitian conjugate of the operators $\tilde{O}_{i\to j}(t)$.

To generate SiV-phonon dissipation terms in the master equation, we simply substitute in the relevant system operator from the SiV-phonon coupling Hamiltonian,

$$\hat{O} = \kappa \hat{H}_I^{\mathrm{Def}} + \hat{H}_I^{\mathrm{Intra}}, \tag{5.20}$$

into 5.19 and use the spectral density $J(\omega) = J^{\mathrm{intra}}(\omega)$. We introduce the dimensionless quantity $\kappa = J^{\mathrm{Def}}(\omega)/J^{\mathrm{Intra}}(\omega)$, into eqn. 5.20, to account for the differing interaction strengths for the deformation potential and intramanifold coupling.

To capture the spontaneous emission of photons, we add in a set of phenomenological Lindblad dissipators, rather than deriving them from first principles. We add in the

dissipators,

$$-\gamma_0\mathcal{D}\left[|g_-\rangle\langle u_+|\right]\rho(t) \tag{5.21}$$

$$-\gamma_0\mathcal{D}\left[|g_+\rangle\langle u_-|\right]\rho(t) \tag{5.22}$$

$$-\gamma_0\mathcal{D}\left[|g_-\rangle\langle u_-| + |g_+\rangle\langle u_+|\right]\rho(t), \tag{5.23}$$

with $\mathcal{D}\left[A\right]\rho(t) = \frac{1}{2}\left(A^\dagger A\rho(t) + \rho(t)A^\dagger A - 2A\rho(t)A^\dagger\right)$ and with $\gamma_0 = 0.001\text{ps}^{-1}$ [133, 134].

In the weak driving limit, when driving the system at resonance, or close to resonance, we encounter scenarios where the spectrum of the Hamiltonian of the system has degeneracies or near degeneracies in the rotating frame. In these cases, the secular approximation is no longer valid. Terms which would typically be discarded due to rapidly oscillating amplitudes in the strong driving limit, now either oscillate much less rapidly, or in the case of a degeneracy, do not oscillate at all. These terms must not be discarded. The result of keeping these terms is that we are left with a master equation which is not of Lindblad form. Such a master equation does not guarantee positivity of the density matrix, however in all results presented here where a non-secular master equation is used, there is no violation of the positivity requirement of the density matrix.

Adding counting fields

Here we perform the same steps as we did in the quantum dot counting field master equations to write down the corresponding equation for this system. The time-evolution of the counting field density matrix ρ_u is

$$\rho_u(t) = U_{u/2}\rho_u(0)U^\dagger_{-u/2},$$

with annotated time-evolution operator $U_u = e^{iu\hat{H}_b}Ue^{-iu\hat{H}_b}$. For any operator $\hat{O}$ that we wish to write in this counting field framework, we perform the same transformation, which results in the operator obeying the Heisenberg like equation

$$i\frac{d\hat{O}_u}{du} = [\hat{O}_u, \hat{H}_B].$$

This implies bosonic bath operators take the form $b_{u,k} = e^{-i\omega_k u}b_{0,k}$. The time-evolution operators $U_{\pm u/2}$ are given by the usual expressions with the Hamiltonians $\hat{H}^\pm_{SB} = \sum g_k\hat{O}(b_k e^{\mp i\omega u/2} + b_k^\dagger e^{\pm i\omega u/2})$. Instead of the von Neumann equation, we solve

$$\frac{d\rho_u(t)}{dt} = -i(\hat{H}^+\rho_u(t) - \rho_u(t)\hat{H}^-) = -i[[\hat{H}, \rho_u(t)]], \tag{5.24}$$

where $[[A,B]] = A^+B - BA^-$. This results in terms in the master equation of the form $O\rho O$ acquiring phase factors, which, as we saw before, keep track of the heat flow.

$$\begin{aligned}\frac{d\rho}{dt} = -\pi \sum_{ij} \Big\{ & [(n+1)J(E_j - E_i) + nJ(E_i - E_j)] \\ & \times \Big[\tilde{O}(t)\tilde{O}_{j\to i}(t)\rho_S(t) - e^{iu(E_j-E_i)}\tilde{O}_{j\to i}(t)\rho_S(t)\tilde{O}(t)\Big] \\ & + [(n+1)J(E_i - E_j) + nJ(E_j - E_i)] \\ & \times \Big[\rho_S(t)\tilde{O}_{j\to i}(t)\tilde{O}(t) - e^{iu(E_i-E_j)}\tilde{O}(t)\rho_S(t)\tilde{O}_{j\to i}(t)\Big] \Big\}\end{aligned} \tag{5.25}$$

Swapping the dummy indices i, j in one of the lines, we have

$$\begin{aligned}\frac{d\rho}{dt} = \pi \sum_{ij} \Big\{ & [(n+1)J(E_i - E_j) + nJ(E_j - E_i)] \\ & \times [e^{iu(E_i-E_j)}(\tilde{O}_{i\to j}(t)\rho_S(t)\tilde{O}(t) + \tilde{O}(t)\rho_S(t)\tilde{O}_{j\to i}(t)) \\ & - \tilde{O}(t)\tilde{O}_{i\to j}(t)\rho_S(t) - \rho_S(t)\tilde{O}_{j\to i}(t)\tilde{O}(t)]\Big\}.\end{aligned} \tag{5.26}$$

We can also get the mean heat transfer, $\langle Q\rangle = -i\mathrm{Tr}\frac{d\rho_u}{du}|_{u=0}$, so

$$\begin{aligned}\frac{d\langle Q\rangle}{dt} = \pi \sum_{ij} & [(n+1)J(E_i - E_j) + nJ(E_j - E_i)] \\ & \times (E_i - E_j)\mathrm{Tr}[\tilde{O}_{i\to j}(t)\rho_S(t)\tilde{O}(t) + \tilde{O}(t)\rho_S(t)\tilde{O}_{j\to i}(t)]\end{aligned} \tag{5.27}$$

As above, this is all non-secular. To make the secular approximation, we again take the operators $\tilde{O}(t)$ to be the Hermitian conjugate of the operators $\tilde{O}_{i\to j}(t)$.

5.3 Results

5.3.1 Cooling Spectra

In fig. 5.4 we plot the steady state heat current, calculated from the non-secular master equation, eqn. 5.27, as a function of the detuning of the laser from E_G and for different driving strengths, with equal driving strength in all three polarisations, denoted σ_+, σ_- and σ_z in panel (a) and with pumping only σ_z in panel (b). The temperature of the phonons is set to 20 K in all results presented, unless explicitly stated otherwise. In the spectra, we see a clear change in the cooling power as the driving strength is increased from the weak driving regime to the strong driving regime. Note, beyond $\Omega = 1$ ps^{-1}, the cooling power decreases, before net heating of the phonons occurs.

For weak resonant driving, the cooling spectra exhibits four peaks. These peaks are centred around the four distinct resonant optical driving frequencies, $\Delta = \pm(\lambda_u \pm \lambda_g)/2$. Of these four peaks, two peaks show cooling, and lie in the $\Delta > 0$ sector, and two peaks

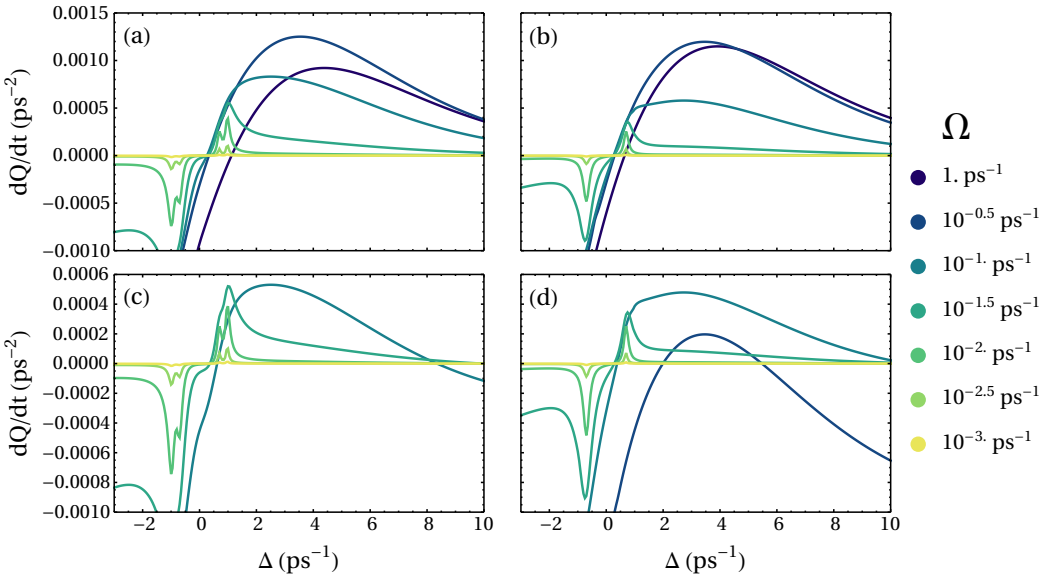

Figure 5.4: Plots of the cooling spectra when driving with all three polarisations at equal driving strengths (a) and with just σ_z (b). (c) and (d) show the net cooling power when we account for the background heating due to the driving laser, for the case of driving all three polarisations, and only σ_z respectively.

show heating, lying in the $\Delta < 0$ sector. In the spin up subspace, the cooling peaks correspond to the σ_+ pumping, when the levels $|g_+\rangle$ and $|u_-\rangle$ are resonant, and σ_z pumping when the levels $|g_-\rangle$ and $|u_-\rangle$ are resonant. The heating peaks result from σ_- pumping, when the levels $|g_-\rangle$ and $|u_+\rangle$ are resonant, and σ_z pumping when the levels $|g_+\rangle$ and $|u_+\rangle$ are resonant. In this regime, the cooling follows the conventional four level laser cooling theory outlined in the introduction.

As the driving strength is increased, laser dressed states which are composed of a significant mixture of the bare spin-orbit state $|u_\pm\rangle$ and $|g_\pm\rangle$ are formed. There are two noticeable effects as we increase the driving strength. The first is the increase in the gross cooling power. The second is the significant broadening we see in the cooling spectra. The resonance between levels is no longer required for cooling, and cooling is sustained over a much larger range of frequencies of the driving laser. These effects are not only seen when pumping with all three polarisations, but also when pumping with any one or any two of them, as seen in fig. 5.4, where the cooling spectrum when pumping with only σ_z is shown.

As in the quantum dot model, the initial increase in cooling power is due to the dependence of the phonon scattering rates on the driving strength, through the spectral density. Moreover, we see the same increasing width in the cooling spectrum, as the driving strength is increased. The eventual decrease in the cooling power with a sufficiently large driving strength is due to the sampling of the spectral density at frequencies beyond its peak, into the exponential cut-off phase. In this model, the cut-off is much larger, and instead the decrease is mostly due to the decreasing thermal

occupation at the energies that the spectral density is being sampled at.

5.3.2 Background Heating

So far, we have discussed the absorption of heat from the phonon reservoir, without considering the heating effect due to background absorption of the driving laser by the material. Any potential laser cooling will then be competing against this heating. Given the heat pumping discussed in this chapter is made possible through the formation of dressed states due to the strong coherent driving of the silicon vacancy, the background heating is certainly not negligible.

We can make an estimate of the effect of this heating by writing the heating rate per vacancy as,

$$\dot{Q}_h = I\alpha/\rho,$$

where α is the absorption coefficient of the diamond at the driving frequency and ρ is the density of defects in the sample. We write the intensity as

$$I = \frac{1}{2}c\epsilon_0 n E_0^2,$$

with n the refractive index of the material. The Rabi frequency can be expressed as

$$\hbar\Omega = dE_0,$$

with d the dipole moment of the transition.

Together these result in

$$\dot{Q}_h = [c\epsilon_0 n\hbar^2/(2d^2)](\alpha/\rho)\Omega^2,$$

for the rate of heating. We take a conservative estimate of the absorption coefficient of diamond, $\alpha = 0.1$ cm^{-1} [127], 14.3 Debye [135] for the dipole moment and we assume a value of $\rho/\alpha = 1.47 \times 10^{22}$ m^{-2}, which corresponds to an emitter density of 10^{23} m^{-3}, which is on the order of one silicon vacancy per million carbon atoms.

Fig. 5.4 (c) and (d) show the net cooling spectra, accounting for the induced background heating. The net increase in cooling power as the driving strength is increased is reduced and net heating of the phonons occurs sooner as the driving strength increases, compared to the case where background heating is not considered. The broadening of the cooling peak in the spectra is unchanged, however.

5.3.3 Level Structure

Fig. 5.5 (a) and (b) depict the eigenvalues of the SiV centre when pumped with only σ_+ polarised light. This polarisation couples the states $|u_-\rangle$ and $|g_+\rangle$, in the spin up subspace, this corresponds to coupling the top of the ground state manifold and the

bottom of the excited state manifold. The arrows indicate the net phonon induced transitions between pairs of levels. The driving parameters for these two level schemes are $\Delta = \Delta_0 + 0.5$ ps^{-1} and $\Omega = 0.3$ ps^{-1}, and $\Delta = \Delta_0$ and $\Omega = 10^{-2.5}$ ps^{-1} for the strong and weak driving respectively, where $\Delta_0 = (\lambda_u + \lambda_g)/2$, the required detuning to bring $|u_-\rangle$ and $|g_+\rangle$ into resonance. Note, the driving parameters for the strong driving case are chosen for clarity in the level structure, and do not correspond to the maximum cooling. Included in the figure is the expansion of the dressed states into the basis of the original states, with $\alpha = 0.424$ and $\beta = 0.905$.

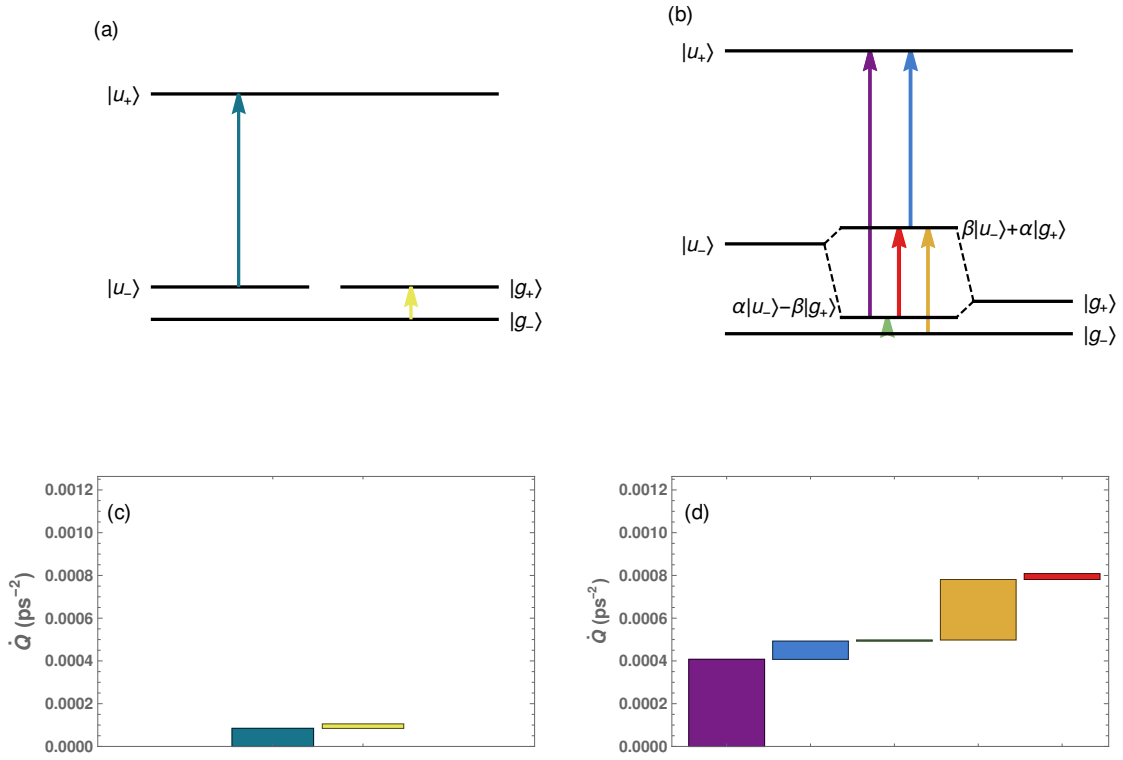

Figure 5.5: The resulting level structure of the driven SiV centre with the associated phonon absorption transitions for (a) weak driving and (b) strong driving. The magnitude of heat absorption between each pair of levels for (c) weak driving and (d) strong driving.

In the case of the weak driving, phonon absorption only takes place due to intramanifold transitions. This is due to the intramanifold coupling, which acts to thermalise the population in each manifold to a temperature equal to the lattice temperature. This intramanifold phonon absorption is seen in the cooling spectra, through the resonant peaks at weak driving.

For strong driving, we see that the dressed states formed from the laser driving result in mixed states. These mixed states result in two new mechanisms for phonon absorption. The first is that the deformation potential coupling can now be exploited to absorb phonons between states from different manifolds, through the dressed state formation.

The second effect is that phonon scattering through the intramanifold coupling can now occur between almost all pairs of levels, with the exception of the transition between the lowest and highest lying states in this example (scattering between these levels is easily achieved by simply pumping with all three polarisations such that all states are mixed to some degree).

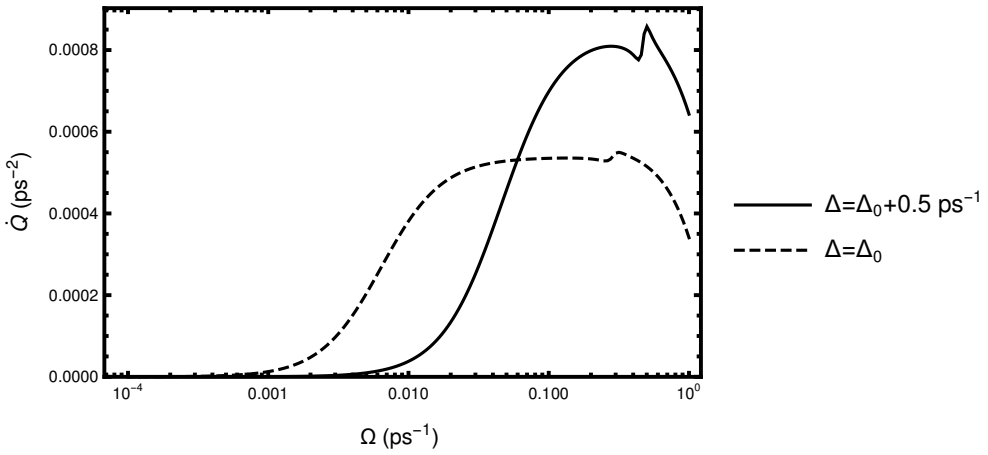

Figure 5.6: The cooling power as a function of Rabi frequency, when pumping with σ_+ for two values of detuning, as indicated.

Fig. 5.5 (c) and (d) show the heat pumping rates, between each pair of levels for the weak driving and strong driving respectively. We see that not only are more phonon absorption channels opened up, but the individual rates of heat absorption between each pair of levels are significantly enhanced. This overall enhancement is a consequence of the dependence of the phonon scattering rates on the driving strength, as discussed in chapter 4, and above. In fig. 5.6 we plot the cooling power on resonance, and just off resonance, as a function of driving strength. We clearly see the increasing heat absorption rate with increasing driving strength, with a subsequent decrease for sufficiently large Ω. We plot $J(\omega)n(\omega)$ in fig 5.7, where it is evident that the scattering rates are strongly dependent on the energy the bath is sampled at. We also plot the level spacings, for which there is an associated heat flow, for both weak and strong driving. In the case of strong driving, we see that the bath is sampled at higher energies, where the scattering rates are higher. Moreover, with larger energy gaps in the spectrum of the system, the energy of the absorbed phonons is also increased. Together, these effects result in the overall increase in power we observe. This simple analysis doesn't take into account the occupation of each level, which will further impact the overall cooling rate.

To understand why the cooling peak broadens as the driving strength increases, we again consider driving only the lowest energy optically active transition with a single polarisation, σ^+ for the spin up subspace, coupling $|u_-\rangle$ and $|g_+\rangle$. The dressed states are of the form $|\psi_+\rangle = \sqrt{1-\epsilon^2}\,|u_-\rangle + \epsilon\,|g_+\rangle$ and $|\psi_-\rangle = \epsilon\,|u_-\rangle - \sqrt{1-\epsilon^2}\,|g_+\rangle$ with $0 < \epsilon < 1$. The laser driving only pumps population between the coupled states, when

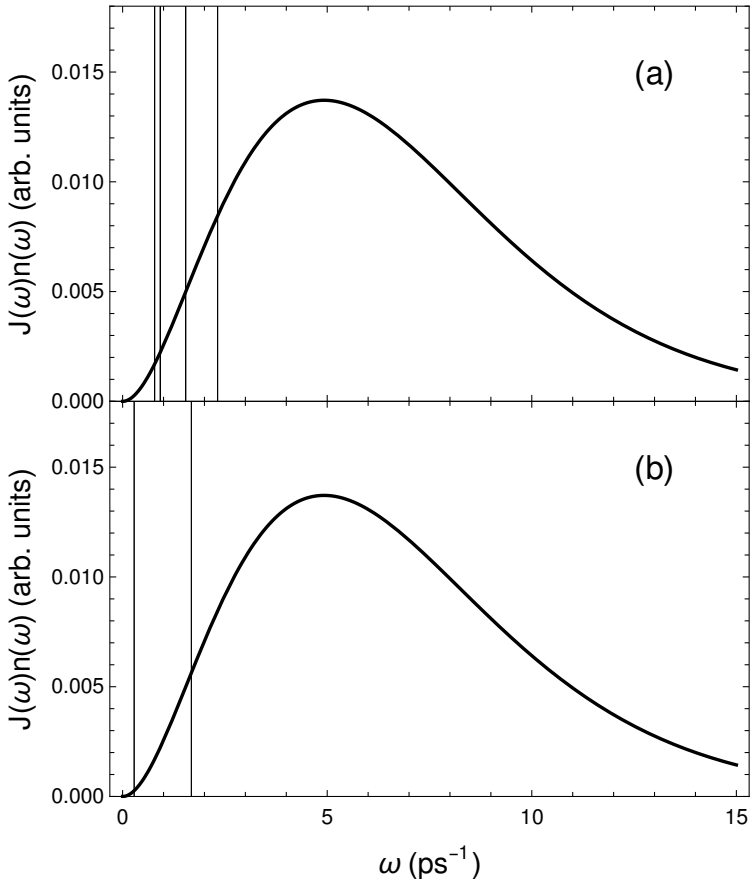

Figure 5.7: Product of spectral density and Bose occupation factor, at a lattice temperature of 20K with lines showing the energy gaps in the spectrum of the SiV centre for (a) strong driving ($\Delta = \Delta_0 + 0.5$ ps^{-1}, $\Omega = 0.3$ ps^{-1}) and (b) weak driving ($\Delta = \Delta_0$, $\Omega = 10^{-2.5}$ ps^{-1}).

$\epsilon \neq 1$ and $\epsilon \neq 0$, i.e. when the dressed states are superpositions of the spin-orbit basis sates. Fundamentally, the cooling protocol relies upon the laser coupling these states and pumping the population between these two levels. Fig. 5.8 is a plot of this mixing parameter as a function of Δ, for different driving strengths. We can clearly see that for weak driving, there is only a very narrow region about $\Delta = \Delta_0$, i.e. resonant driving, for which $\epsilon \neq 1$ or $\epsilon \neq 0$. This region increases significantly with increasing driving strength.

In a realistic diamond sample, there will be an ensemble of SiV centres. These defects will be in a mixture of spin states. In order to have identical cooling from all centres, it is important to drive with both σ^- and σ^+, or with all three of σ^-, σ^+ and σ^z, The effect of driving with σ^+ on an SiV centre in a spin up configuration, is identical to the effect of driving a spin down defect with σ^-. Similarly, driving with σ_z polarised light has the same cooling effect for all spin configurations. In order to maximise the cooling power in an ensemble of SiV centres in a host diamond lattice, it is then crucial to drive with at least both σ^+ ad σ^- polarised light.

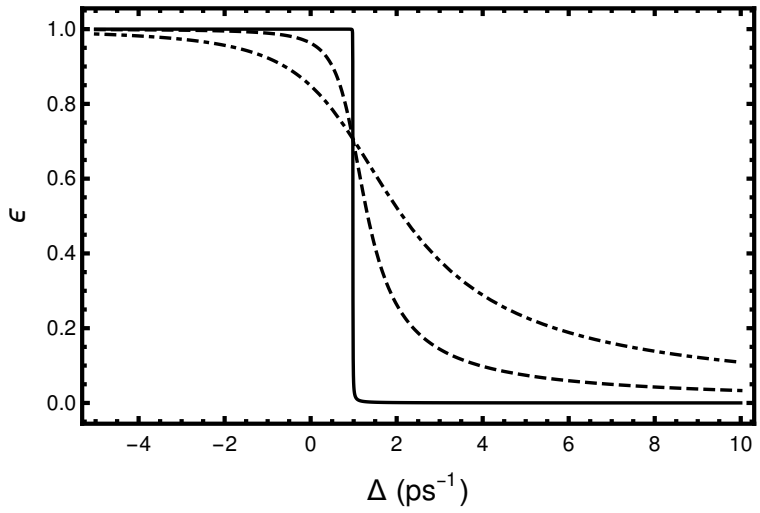

Figure 5.8: The dressed state mixing parameter ϵ as a function of detuning for increasing driving strength $\Omega = 10^{-3}$ ps^{-1} (solid), $\Omega = 0.3$ ps^{-1} (dashed) and $\Omega = 1$ ps^{-1} (dot dashed)

5.4 Secular Born-Markov vs Non-Secular Born-Markov

In the weak driving regime, when driving the system such that two states are at or close to resonance, the system Hamiltonian exhibits degeneracies or closely spaced eigenvalues. Such closely spaced eigenvalues indicate a timescale of the system $\tau \propto (E_1 - E_2)^{-1}$, which may well be longer than the supposedly slowest timescale set by the interaction between the system and bath. Here, the secular approximation breaks down. In section 5.2 we discussed the derivation of the master equation without making the secular approximation. The secular master equation is clearly inappropriate when modelling the laser cooling in the weak driving regime, where we claim that the non-secular master equation is the correct approach. Note, when using such a non-secular model, the positivity of the density matrix is no longer guaranteed, and as such it is important to check that this is not violated for any results. For results presented here, positivity is not violated.

To understand the validity of each master equation in the strong and weak driving limits, we compare the cooling spectra that result from the secular and non-secular master equations, as well as a phenomenological Lindblad master equation. For the phenomenological model, we use a dissipator

$$\gamma D(A) = -\gamma/2 \left(AA^\dagger \rho + \rho AA^\dagger - 2A^\dagger \rho A \right),$$

for a transition caused by a jump operator $A^\dagger$. For the intramanifold phonon transitions in the SiV center, this is achieved by adding in the dissipators

$$\gamma_-^u(\lambda_u) D\left(|u_-\rangle \langle u_+| \right),$$

$$\gamma_+^u(\lambda_u) D\left(|u_+\rangle\langle u_-|\right),$$

$$\gamma_-^g(\lambda_g) D\left(|u_-\rangle\langle u_+|\right),$$

$$\gamma_+^g(\lambda_g) D\left(|u_+\rangle\langle u_-|\right).$$

For the scattering rates, we take $\gamma_+^{u/g} = \pi J(\lambda^{u/g}) n(\lambda^{u/g})$ and $\gamma_-^{u/g} = \pi J(\lambda^{u/g}) \left(n(\lambda^{u/g}) + 1\right)$. Such a phenomenological master equation ignores the effect of the dressed states on the phonon scattering, and is only applicable in the weak driving limit.

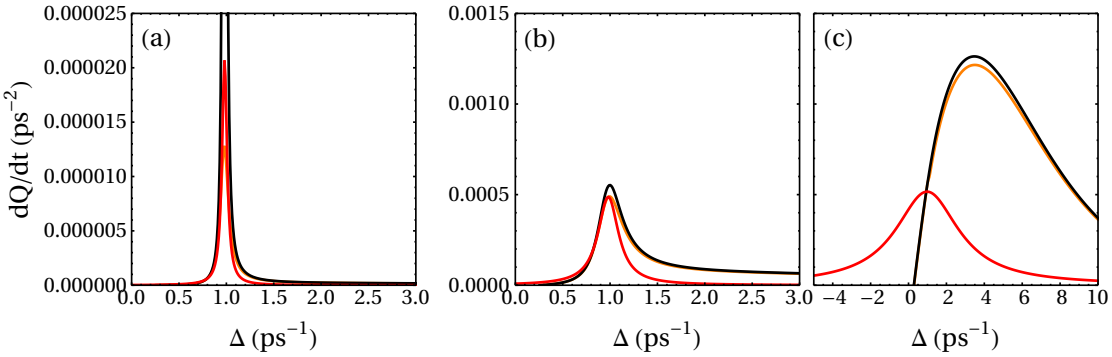

Figure 5.9: Comparison of the cooling spectra resulting from the secular (black), non-secular (orange) and Lindblad (red) models for $\Omega = 10^{-3}$ ps^{-1} (a), $10^{-1.7}$ ps^{-1} (b) and $10^{-0.5}$ ps^{-1}(c).

In Fig. 5.9 we plot the cooling spectra in the weak, intermediate and strong driving regime, computed using each of the three methods outlined above, driving only the σ_- transition. This pumping corresponds to bringing the levels $|g_+\rangle$ and $|u_-\rangle$ into resonance, i.e. the top of the ground state manifold and the bottom of the excited state manifold. This is achieved for $\Delta = (\lambda_u + \lambda_g)/2$, the smallest resonant optical driving frequency. For weak driving, the secular and non-secular Born-Markov master equations agree when the laser is tuned just off resonance. On resonance, however, the secular master equation leads to unphysical cooling powers. The non-secular master equation and the phenomenological approach, give cooling powers that are of the same order of magnitude, with both spectra exhibiting a sharp peak.

Increasing the driving strength into the intermediate pumping regime, we see all three approaches now agree quite well, with the secular and non-secular master equation displaying more structure in the cooling profile, which is absent in the simpler phenomenological approach, featuring only a Lorentzian cooling profile. In this regime, the effect of the dressed states is non-negligible, as we can see the broadening effect leading to finite cooling powers for driving frequencies detuned from the transition.

In the strong driving regime, the secular and non-secular master equations agree, with a small mismatch in the cooling powers at the peak of the cooling spectra. In this regime the phenomenological model completely fails, as expected, due to its inability to capture the effects of the dressed states on the phonon absorption. This model fails to

predict the heating effect that is seen when the laser is tuned such that $\Delta < \Delta 0$.

In fig 5.10, the resonant cooling power as a function of driving strength is plotted, for each method. For strong driving, only the secular and non-secular theories predict the crossover from cooling to heating. Before this transition, all three methods predict similar cooling powers. As the driving strength is lowered, the Lindblad theory and the non-secular Born-Markov theory correctly predict a decreasing cooling power. In this regime, the cooling power is no longer limited by the phonon scattering rates as it is in the strong driving regime, but is instead limited by the pumping of the population between the resonant levels. The secular Born-Markov theory predicts an unphysical result of constant resonant cooling power.

Varying the temperature of the bath, in fig. 5.11 we plot the cooling power on resonance as the bath temperature is reduced from 10 K to 0 K. Here we see that the secular Born-Markov model predicts higher cooling powers for all lattice temperatures considered. All theories predict the cooling rapidly drops to zero as the bath temperature is lowered below $\lambda_g/k_B \approx 2.15$ K. This is physically reasonable, and expected in a discrete level structure, where the occupation of the phonons at λ_g vanishes at temperatures less than λ_g/k_B.

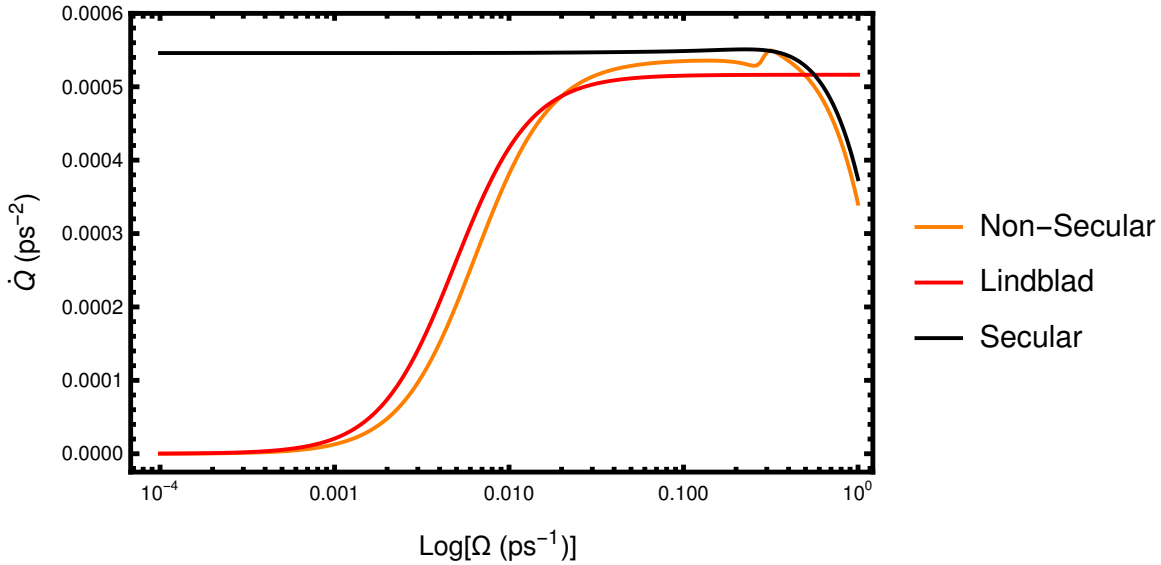

Figure 5.10: Resonant cooling power as a function of Rabi frequency for the secular (black), non-secular (orange) and Lindblad (red) models.

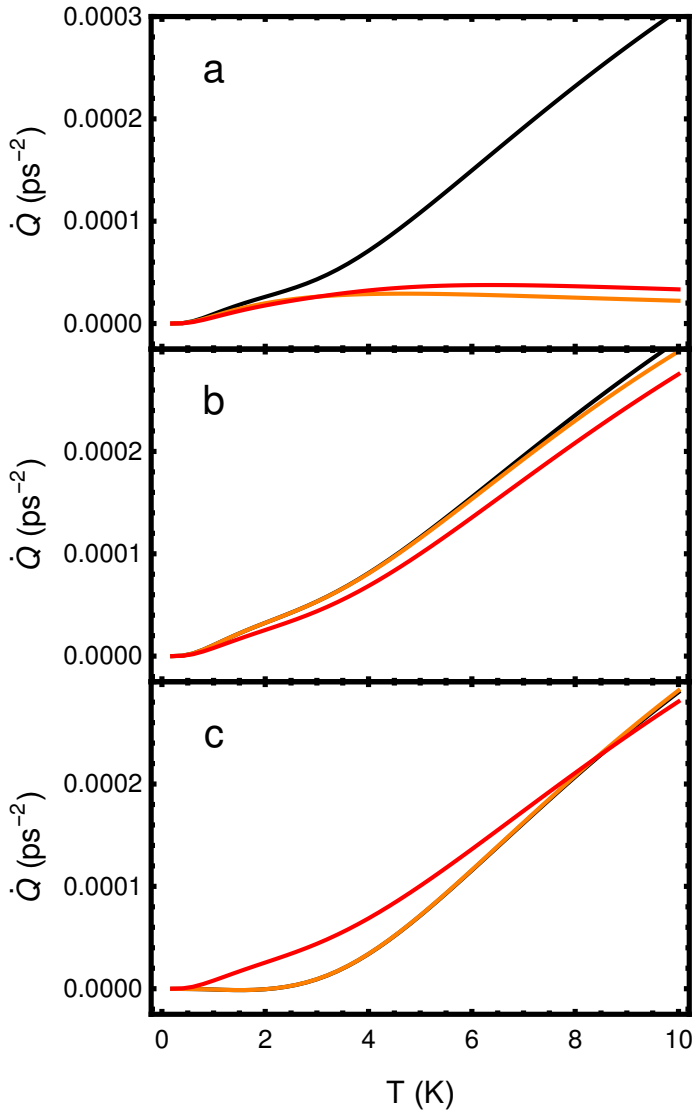

Figure 5.11: The resonant cooling power for $\Omega = 10^{-3}$ ps^{-1} (a), $10^{-1.7}$ ps^{-1} (b) and $10^{-0.5}$ ps^{-1}(c) as a function of the temperature of the phonons.

5.5 Conclusions

We have proposed a theory of optical refrigeration of solids using laser driven silicon vacancy centres in diamond. Using a non-secular master equation along with full counting statistics, we have computed the cooling spectra across a range of driving strengths. Interestingly, we observed both an increase in the cooling power and increase in the range of driving frequencies for which cooling is sustained, when the driving strength was increased. These benefits were attributed to the strong-field dressed state formation, with such coherent effects generally not considered in conventional laser cooling models [114, 117, 118, 120]. Including the background absorption of the laser driving only moderately reduced the overall cooling power, with an increase in both net cooling and the cooling region over the detuning still observed as the driving strength was increased.

Comparing the cooling spectra that result from the use of a secular, non-secular and phenomenological Lindblad maser equation to model the cooling protocol, we claim that in a weakly driven system, the secular theory is inappropriate. Such a theory resulted in unphysical cooling when driven weakly at resonance, which can be attributed to the near degenerate states in the system Hamiltonian, which render the secular approximation invalid. This result is not specific to the model considered here, but can be applied to a general class of laser cooling protocols which involve coherently driving an emitter. Generally, the secular and phenomenological Lindblad models both have a limited range of validity in the weak and strong driving regime respectively, where the non-secular theory provides more accurate results. These results support the use of Bloch-Redfield equations in quantum thermal machines, in spite of their potential to give unphysical results. This conclusion is similar to previous conclusions on the dynamics and thermodynamics of other open quantum systems, where the Bloch-Redfield equation has similarly been argued to provide the most accurate description [136, 137, 138, 139, 140].

6 Concluding Remarks

In this thesis, we have discussed the thermodynamic features of laser induced heat flows between solid state optical emitters and the phonon modes of the host medium. Here, we provide a brief summary of the work, and discuss possible future directions to be explored.

We have shown that strong coherent driving of solid state emitters can be used to implement controlled thermodynamic processes. In chapter 2, we present results which show that shaped laser pulses can be used to implement controlled thermodynamic processes for a single exciton transition interacting with the heat bath of phonons. The dressed state formation resulting from the coherent driving can be used to control the scattering rates between the system and the bath and the effective temperature of the system, allowing a significant degree of control in the transfer of heat between the exciton and phonon, which includes the control of the direction of the heat flow, and the degree of reversibility of this heat transfer. These effects allow for the implementation of any thermodynamic process in the single-qubit single-reservoir system. For example, adiabatic heating or cooling could be implemented using weak chirped pulses, for which the small pulse amplitude implies a small heat flow. These processes may be useful for high-efficiency photovoltaics, by allowing the hot excitons created by light to be cooled before they release heat. More broadly, implementing such reversible heat transfer is crucial in the design and realisation of efficient quantum thermal machines.

Photon counting of exciton luminescence under pulsed excitation [4, 28], or nanoscale current measurements [21, 26], provides direct access to the probability distribution of the exciton occupation, and hence thermodynamic quantities such as entropy. Our theory could be tested by comparison against such experiments. Some additional thermodynamic information could be obtained optically: spectrally-resolved luminescence, for example, could give the dressed-state occupations, and hence the effective temperature. A direct measurement of the heat based on thermal effects would not be possible due to their small size. One approach could be to determine the work done by the driving pulse from its absorption, and use the first law of thermodynamics to calculate the heat. Another would be to obtain the heat from theory, fitted and validated using its predictions for quantities such as luminescence. Overall, however, the quantum-dot exciton transition seems to be a promising system in which to study thermodynamic

processes at the quantum scale – given the possibility, predicted here, of using laser pulses to implement and control thermodynamic processes.

Extending the theory to include more complex shaped laser pulses, we optimise the efficiency over the shape of the detuning of a Gaussian laser pulse in chapter 3. Here, we show that departing from a simple linear chirping of the laser frequency allows for increased control of the thermodynamic properties of the heat absorption from the phonons.

This work is a proof of principle, and lays the foundation for a more thorough examination of optimised thermodynamic processes in laser controlled quantum dots. More advanced numerical optimisation techniques could be used, such as the adjoint-method [141], for example, to compute the gradient of the efficiency, or some other thermodynamic quantities of interest, with respect to the pulse shaping parameters, for both the temporal profile of the driving frequency and the pulse envelope. With such a tool, gradient based optimisation techniques could then be used to find optimal solutions for the pulse profile to maximise the performance of any thermodynamic protocol that involves driving a system with time dependent fields.

Finding globally optimal pulse shapes in order to maximise the efficiency is interesting, but a more practical goal would be to find pulse shapes which optimise the efficiency at maximum power, a quantity known as the Curzon-Ahlborn efficiency [125]. Moreover, by combing these advanced numerical optimisation techniques with more advanced numerical simulation techniques, such as time evolving matrix product operators [142, 143], one could probe the optimal pulse shapes for systems for which the Markov approximations are not justified. Combining non-Markovian dynamics, quantum thermodynamics and advanced numerical optimisation techniques would allow for the exploration of a rich class of possible thermal machines.

In chapter 4 we revisited the steady state quantum dot heat pumping model, as considered by Gauger et al. [121]. We derived an analytical expression for the steady state heat absorption rate, which clearly emphasises the role of the driving laser parameters on the requirements for cooling to be achieved, in terms of the effective temperature of the photon induced dissipation of the exciton. We compute the statistics of the heat transfer between the exciton and each bath, through the use of the counting field formalism.

From this investigation into the heat pumping that results from the steady state driving of quantum emitters, we show theoretically that strong coherent driving of silicon vacancy centres in diamond can be used as a platform for optical refrigeration of solids. Such active use of the dressed state formation for laser cooling processes is a novel concept, where conventional laser cooling protocols are typically modelled through classical rate equations which fail to capture the effects of coherent driving [114, 117, 118, 120].

We commented on the applicability of secular and non-secular master equations which can be used to model such cooling protocols, and conclude that only the non-secular Bloch-Redfield master equation is appropriate in both the weak driving and strong driving regime. Our theory sheds light on the benefits of the dressed state formation, and could be expanded to the use of laser dressed state based cooling protocol in other systems, rare-earth doped glasses, for example.

Bibliography

[1] Gregory S. Engel, Tessa R. Calhoun, Elizabeth L. Read, Tae-Kyu Ahn, Tomáš Mančal, Yuan-Chung Cheng, Robert E. Blankenship, and Graham R. Fleming. Evidence for wavelike energy transfer through quantum coherence in photosynthetic systems. *Nature*, 446(7137):782–786, April 2007.

[2] John A. Venables. *Introduction to Surface and Thin Film Processes*. Cambridge University Press, first edition, August 2000.

[3] J. Duan, H. Huang, D. Jung, Z. Zhang, J. Norman, J. E. Bowers, and F. Grillot. Semiconductor quantum dot lasers epitaxially grown on silicon with low linewidth enhancement factor. *Applied Physics Letters*, 112(25):251111, June 2018.

[4] Yu-Ming He, Yu He, Yu-Jia Wei, Dian Wu, Mete Atatüre, Christian Schneider, Sven Höfling, Martin Kamp, Chao-Yang Lu, and Jian-Wei Pan. On-demand semiconductor single-photon source with near-unity indistinguishability. *Nature Nanotechnology*, 8(3):213–217, March 2013.

[5] Yu-Jia Wei, Yu-Ming He, Ming-Cheng Chen, Yi-Nan Hu, Yu He, Dian Wu, Christian Schneider, Martin Kamp, Sven Höfling, Chao-Yang Lu, and Jian-Wei Pan. Deterministic and Robust Generation of Single Photons from a Single Quantum Dot with 99.5% Indistinguishability Using Adiabatic Rapid Passage. *Nano Letters*, 14(11):6515–6519, November 2014.

[6] Pochung Chen, C. Piermarocchi, and L. J. Sham. Control of Exciton Dynamics in Nanodots for Quantum Operations. *Physical Review Letters*, 87(6):067401, July 2001.

[7] T. Calarco, A. Datta, P. Fedichev, E. Pazy, and P. Zoller. Spin-based all-optical quantum computation with quantum dots: Understanding and suppressing decoherence. *Physical Review A*, 68(1), July 2003.

[8] H. Kamada and H. Gotoh. Quantum computation with quantum dot excitons. *Semiconductor Science and Technology*, 19(4):S392–S396, April 2004.

[9] Brendon W. Lovett, Ahsan Nazir, Ehoud Pazy, Sean D. Barrett, Timothy P. Spiller, and G. Andrew D. Briggs. Quantum computing with spin qubits interacting through delocalized excitons: Overcoming hole mixing. *Physical Review B*, 72(11), September 2005.

[10] Donald C. Reynolds and Thomas C. Collins. *Excitons: Their Properties and Uses*. Elsevier, 1981.

[11] S. B. Nam, D. C. Reynolds, C. W. Litton, R. J. Almassy, T. C. Collins, and C. M. Wolfe. Free-exciton energy spectrum in GaAs. *Physical Review B*, 13(2):761–767, January 1976.

[12] Sebastian Lüker and Doris E Reiter. A review on optical excitation of semiconductor quantum dots under the influence of phonons. *Semiconductor Science and Technology*, 34(6):063002, June 2019.

[13] A. Greilich, R. Oulton, E. A. Zhukov, I. A. Yugova, D. R. Yakovlev, M. Bayer, A. Shabaev, Al. L. Efros, I. A. Merkulov, V. Stavarache, D. Reuter, and A. Wieck. Optical Control of Spin Coherence in Singly Charged (In , Ga) As / GaAs Quantum Dots. *Physical Review Letters*, 96(22), June 2006.

[14] A J Ramsay. A review of the coherent optical control of the exciton and spin states of semiconductor quantum dots. *Semiconductor Science and Technology*, 25(10):103001, October 2010.

[15] Erik M. Gauger, Simon C. Benjamin, Ahsan Nazir, and Brendon W. Lovett. High-fidelity all-optical control of quantum dot spins: Detailed study of the adiabatic approach. *Physical Review B*, 77(11):115322, March 2008.

[16] Pieter Kok and Brendon W. Lovett. *Introduction to Optical Quantum Information Processing*. Cambridge University Press, Cambridge, 2010.

[17] Rodney Loudon. *The Quantum Theory of Light*. Oxford Science Publications. Oxford University Press, Oxford ; New York, 3rd ed edition, 2000.

[18] T. H. Stievater, Xiaoqin Li, D. G. Steel, D. Gammon, D. S. Katzer, D. Park, C. Piermarocchi, and L. J. Sham. Rabi Oscillations of Excitons in Single Quantum Dots. *Physical Review Letters*, 87(13), September 2001.

[19] H. Kamada, H. Gotoh, J. Temmyo, T. Takagahara, and H. Ando. Exciton Rabi Oscillation in a Single Quantum Dot. *Physical Review Letters*, 87(24):246401, November 2001.

[20] H. Htoon, T. Takagahara, D. Kulik, O. Baklenov, A. L. Holmes, and C. K. Shih. Interplay of Rabi Oscillations and Quantum Interference in Semiconductor Quantum Dots. *Physical Review Letters*, 88(8):087401, February 2002.

[21] A. Zrenner, E. Beham, S. Stufler, F. Findeis, M. Bichler, and G. Abstreiter. Coherent properties of a two-level system based on a quantum-dot photodiode. *Nature*, 418:612, August 2002.

[22] E. R. Schmidgall, P. R. Eastham, and R. T. Phillips. Population inversion in quantum dot ensembles via adiabatic rapid passage. *Physical Review B*, 81(19), May 2010.

[23] S. Hughes. Breakdown of the Area Theorem: Carrier-Wave Rabi Flopping of Femtosecond Optical Pulses. *Physical Review Letters*, 81(16):3363–3366, October 1998.

[24] Kevin A Fischer, Lukas Hanschke, Malte Kremser, Jonathan J Finley, Kai Müller, and Jelena Vučković. Pulsed Rabi oscillations in quantum two-level systems: Beyond the area theorem. *Quantum Science and Technology*, 3(1):014006, January 2018.

[25] V.S. Malinovsky and J.L. Krause. General theory of population transfer by adiabatic rapid passage with intense, chirped laser pulses. *The European Physical Journal D*, 14(2):147–155, May 2001.

[26] Yanwen Wu, I. M. Piper, M. Ediger, P. Brereton, E. R. Schmidgall, P. R. Eastham, M. Hugues, M. Hopkinson, and R. T. Phillips. Population Inversion in a Single InGaAs Quantum Dot Using the Method of Adiabatic Rapid Passage. *Physical Review Letters*, 106(6), February 2011.

[27] Timo Kaldewey, Sebastian Lüker, Andreas V. Kuhlmann, Sascha R. Valentin, Arne Ludwig, Andreas D. Wieck, Doris E. Reiter, Tilmann Kuhn, and Richard J. Warburton. Coherent and robust high-fidelity generation of a biexciton in a quantum dot by rapid adiabatic passage. *Physical Review B*, 95(16):161302, April 2017.

[28] C.-M. Simon, T. Belhadj, B. Chatel, T. Amand, P. Renucci, A. Lemaitre, O. Krebs, P. A. Dalgarno, R. J. Warburton, X. Marie, and B. Urbaszek. Robust Quantum Dot Exciton Generation via Adiabatic Passage with Frequency-Swept Optical Pulses. *Physical Review Letters*, 106(16):166801, April 2011.

[29] Reuble Mathew, Eric Dilcher, Angela Gamouras, Ajan Ramachandran, Hong Yi Shi Yang, Sabine Freisem, Dennis Deppe, and Kimberley C. Hall. Subpicosecond adiabatic rapid passage on a single semiconductor quantum dot: Phonon-mediated dephasing in the strong-driving regime. *Physical Review B*, 90(3), July 2014.

[30] Adrien Dousse, Jan Suffczyński, Alexios Beveratos, Olivier Krebs, Aristide Lemaître, Isabelle Sagnes, Jacqueline Bloch, Paul Voisin, and Pascale Senellart.

Ultrabright source of entangled photon pairs. *Nature*, 466(7303):217–220, July 2010.

[31] P. Michler. A Quantum Dot Single-Photon Turnstile Device. *Science*, 290(5500):2282–2285, December 2000.

[32] R. T. Brierley, C. Creatore, P. B. Littlewood, and P. R. Eastham. Adiabatic State Preparation of Interacting Two-Level Systems. *Physical Review Letters*, 109(4), July 2012.

[33] C. Creatore, R. T. Brierley, R. T. Phillips, P. B. Littlewood, and P. R. Eastham. Creation of entangled states in coupled quantum dots via adiabatic rapid passage. *Physical Review B*, 86(15), October 2012.

[34] P. R. Eastham and R. T. Phillips. Quantum condensation from a tailored exciton population in a microcavity. *Physical Review B*, 79(16), April 2009.

[35] E. Peter, J. Hours, P. Senellart, A. Vasanelli, A. Cavanna, J. Bloch, and J. M. Gérard. Phonon sidebands in exciton and biexciton emission from single GaAs quantum dots. *Physical Review B*, 69(4), January 2004.

[36] B. Krummheuer, V. M. Axt, and T. Kuhn. Theory of pure dephasing and the resulting absorption line shape in semiconductor quantum dots. *Physical Review B*, 65(19), May 2002.

[37] L. Besombes, K. Kheng, L. Marsal, and H. Mariette. Acoustic phonon broadening mechanism in single quantum dot emission. *Physical Review B*, 63(15), March 2001.

[38] F. Gindele, K. Hild, W. Langbein, and U. Woggon. Phonon interaction of single excitons and biexcitons. *Physical Review B*, 60(4):R2157–R2160, July 1999.

[39] T. Takagahara. Electron-phonon interactions and excitonic dephasing in semiconductor nanocrystals. *Physical Review Letters*, 71(21):3577–3580, November 1993.

[40] D. Sarkar, H. P. van der Meulen, J. M. Calleja, J. M. Meyer, R. J. Haug, and K. Pierz. Piezoelectric exciton acoustic-phonon coupling in single quantum dots. *Physical Review B*, 78(24), December 2008.

[41] A. J. Ramsay, Achanta Venu Gopal, E. M. Gauger, A. Nazir, B. W. Lovett, A. M. Fox, and M. S. Skolnick. Damping of Exciton Rabi Rotations by Acoustic Phonons in Optically Excited InGaAs / GaAs Quantum Dots. *Physical Review Letters*, 104(1):017402, January 2010.

[42] D E Reiter, T Kuhn, M Glässl, and V M Axt. The role of phonons for exciton and biexciton generation in an optically driven quantum dot. *Journal of Physics: Condensed Matter*, 26(42):423203, October 2014.

[43] S. Lüker, T. Kuhn, and D. E. Reiter. Phonon impact on optical control schemes of quantum dots: Role of quantum dot geometry and symmetry. *Physical Review B*, 96(24):245306, December 2017.

[44] D Wigger, S Lüker, D E Reiter, V M Axt, P Machnikowski, and T Kuhn. Energy transport and coherence properties of acoustic phonons generated by optical excitation of a quantum dot. *Journal of Physics: Condensed Matter*, 26(35):355802, September 2014.

[45] Timo Kaldewey, Sebastian Lüker, Andreas V. Kuhlmann, Sascha R. Valentin, Jean-Michel Chauveau, Arne Ludwig, Andreas D. Wieck, Doris E. Reiter, Tilmann Kuhn, and Richard J. Warburton. Demonstrating the decoupling regime of the electron-phonon interaction in a quantum dot using chirped optical excitation. *Physical Review B*, 95(24):241306, June 2017.

[46] M. Glässl, A. M. Barth, and V. M. Axt. Proposed Robust and High-Fidelity Preparation of Excitons and Biexcitons in Semiconductor Quantum Dots Making Active Use of Phonons. *Physical Review Letters*, 110(14), April 2013.

[47] M. Glässl, A. Vagov, S. Lüker, D. E. Reiter, M. D. Croitoru, P. Machnikowski, V. M. Axt, and T. Kuhn. Long-time dynamics and stationary nonequilibrium of an optically driven strongly confined quantum dot coupled to phonons. *Physical Review B*, 84(19), November 2011.

[48] Per-Lennart Ardelt, Lukas Hanschke, Kevin A. Fischer, Kai Müller, Alexander Kleinkauf, Manuel Koller, Alexander Bechtold, Tobias Simmet, Jakob Wierzbowski, Hubert Riedl, Gerhard Abstreiter, and Jonathan J. Finley. Dissipative preparation of the exciton and biexciton in self-assembled quantum dots on picosecond time scales. *Physical Review B*, 90(24), December 2014.

[49] J. H. Quilter, A. J. Brash, F. Liu, M. Glässl, A. M. Barth, V. M. Axt, A. J. Ramsay, M. S. Skolnick, and A. M. Fox. Phonon-assisted population inversion of a single InGaAs/GaAs quantum dot by pulsed laser excitation. *Physical Review Letters*, 114:137401, 2015.

[50] S. Bounouar, M. Müller, A. M. Barth, M. Glässl, V. M. Axt, and P. Michler. Phonon-assisted robust and deterministic two-photon biexciton preparation in a quantum dot. *Physical Review B*, 91(16), April 2015.

[51] A. J. Brash, L. M. P. P. Martins, A. M. Barth, F. Liu, J. H. Quilter, M. Glässl, V. M. Axt, A. J. Ramsay, M. S. Skolnick, and A. M. Fox. Dynamic vibronic

coupling in InGaAs quantum dots [Invited]. *Journal of the Optical Society of America B*, 33(7):C115, July 2016.

[52] F. Liu, L. M. P. Martins, A. J. Brash, A. M. Barth, J. H. Quilter, V. M. Axt, M. S. Skolnick, and A. M. Fox. Ultrafast depopulation of a quantum dot by LA-phonon-assisted stimulated emission. *Physical Review B*, 93(16), April 2016.

[53] A. Vagov, M. D. Croitoru, V. M. Axt, T. Kuhn, and F. M. Peeters. Nonmonotonic Field Dependence of Damping and Reappearance of Rabi Oscillations in Quantum Dots. *Physical Review Letters*, 98(22), June 2007.

[54] S. Lüker, K. Gawarecki, D. E. Reiter, A. Grodecka-Grad, V. M. Axt, P. Machnikowski, and T. Kuhn. Influence of acoustic phonons on the optical control of quantum dots driven by adiabatic rapid passage. *Physical Review B*, 85(12):121302, March 2012.

[55] R. Landauer. Irreversibility and Heat Generation in the Computing Process. *IBM Journal of Research and Development*, 5(3):183–191, July 1961.

[56] M. O. Scully. Extracting Work from a Single Heat Bath via Vanishing Quantum Coherence. *Science*, 299(5608):862–864, February 2003.

[57] Gianluca Francica, John Goold, Francesco Plastina, and Mauro Paternostro. Daemonic ergotropy: Enhanced work extraction from quantum correlations. *npj Quantum Information*, 3(1), December 2017.

[58] A. E Allahverdyan, R Balian, and Th. M Nieuwenhuizen. Maximal work extraction from finite quantum systems. *Europhysics Letters (EPL)*, 67(4):565–571, August 2004.

[59] R. Dillenschneider and E. Lutz. Energetics of quantum correlations. *EPL (Europhysics Letters)*, 88(5):50003, December 2009.

[60] M. O. Scully, K. R. Chapin, K. E. Dorfman, M. B. Kim, and A. Svidzinsky. Quantum heat engine power can be increased by noise-induced coherence. *Proceedings of the National Academy of Sciences*, 108(37):15097–15100, September 2011.

[61] Ceren Dağ, Wolfgang Niedenzu, Özgür Müstecaplıoğlu, and Gershon Kurizki. Multiatom Quantum Coherences in Micromasers as Fuel for Thermal and Nonthermal Machines. *Entropy*, 18(7):244, June 2016.

[62] J. Roßnagel, O. Abah, F. Schmidt-Kaler, K. Singer, and E. Lutz. Nanoscale Heat Engine Beyond the Carnot Limit. *Physical Review Letters*, 112(3):030602, January 2014.

[63] Gonzalo Manzano, Fernando Galve, Roberta Zambrini, and Juan M. R. Parrondo. Entropy production and thermodynamic power of the squeezed thermal reservoir. *Physical Review E*, 93(5):052120, May 2016.

[64] Wolfgang Niedenzu, Victor Mukherjee, Arnab Ghosh, Abraham G. Kofman, and Gershon Kurizki. Quantum engine efficiency bound beyond the second law of thermodynamics. *Nature Communications*, 9(1):165, December 2018.

[65] F. Plastina, A. Alecce, T. J. G. Apollaro, G. Falcone, G. Francica, F. Galve, N. Lo Gullo, and R. Zambrini. Irreversible Work and Inner Friction in Quantum Thermodynamic Processes. *Physical Review Letters*, 113(26):260601, December 2014.

[66] Kay Brandner and Udo Seifert. Periodic thermodynamics of open quantum systems. *Physical Review E*, 93(6):062134, June 2016.

[67] Kay Brandner, Michael Bauer, and Udo Seifert. Universal Coherence-Induced Power Losses of Quantum Heat Engines in Linear Response. *Physical Review Letters*, 119(17):170602, October 2017.

[68] Shujin Deng, Aurélia Chenu, Pengpeng Diao, Fang Li, Shi Yu, Ivan Coulamy, Adolfo del Campo, and Haibin Wu. Superadiabatic quantum friction suppression in finite-time thermodynamics. *Science Advances*, 4(4):eaar5909, April 2018.

[69] Ronnie Kosloff and Tova Feldmann. Discrete four-stroke quantum heat engine exploring the origin of friction. *Physical Review E*, 65(5):055102, May 2002.

[70] Tova Feldmann and Ronnie Kosloff. Quantum lubrication: Suppression of friction in a first-principles four-stroke heat engine. *Physical Review E*, 73(2):025107, February 2006.

[71] Raam Uzdin, Amikam Levy, and Ronnie Kosloff. Equivalence of Quantum Heat Machines, and Quantum-Thermodynamic Signatures. *Physical Review X*, 5(3), September 2015.

[72] James Klatzow, Jonas N. Becker, Patrick M. Ledingham, Christian Weinzetl, Krzysztof T. Kaczmarek, Dylan J. Saunders, Joshua Nunn, Ian A. Walmsley, Raam Uzdin, and Eilon Poem. Experimental Demonstration of Quantum Effects in the Operation of Microscopic Heat Engines. *Physical Review Letters*, 122(11):110601, March 2019.

[73] Johannes Roßnagel, Samuel T. Dawkins, Karl N. Tolazzi, Obinna Abah, Eric Lutz, Ferdinand Schmidt-Kaler, and Kilian Singer. A single-atom heat engine. *Science*, 352(6283):325–329, April 2016.

[74] D. Gelbwaser-Klimovsky and G. Kurizki. Work extraction from heat-powered quantized optomechanical setups. *Scientific Reports*, 5(1):7809, July 2015.

[75] Keye Zhang, Francesco Bariani, and Pierre Meystre. Quantum Optomechanical Heat Engine. *Physical Review Letters*, 112(15):150602, April 2014.

[76] Andreas Dechant, Nikolai Kiesel, and Eric Lutz. All-Optical Nanomechanical Heat Engine. *Physical Review Letters*, 114(18):183602, May 2015.

[77] I. Wilson-Rae, P. Zoller, and A. Imamoğlu. Laser Cooling of a Nanomechanical Resonator Mode to its Quantum Ground State. *Physical Review Letters*, 92(7):075507, February 2004.

[78] Mark T. Mitchison, Marcus Huber, Javier Prior, Mischa P. Woods, and Martin B. Plenio. Realising a quantum absorption refrigerator with an atom-cavity system. *Quantum Science and Technology*, 1(1):015001, March 2016.

[79] Gleb Maslennikov, Shiqian Ding, Roland Hablützel, Jaren Gan, Alexandre Roulet, Stefan Nimmrichter, Jibo Dai, Valerio Scarani, and Dzmitry Matsukevich. Quantum absorption refrigerator with trapped ions. *Nature Communications*, 10(1):202, December 2019.

[80] Michele Campisi, Jukka Pekola, and Rosario Fazio. Nonequilibrium fluctuations in quantum heat engines: Theory, example, and possible solid state experiments. *New Journal of Physics*, 17(3):035012, March 2015.

[81] A. O. Niskanen, Y. Nakamura, and J. P. Pekola. Information entropic superconducting microcooler. *Physical Review B*, 76(17):174523, November 2007.

[82] Giovanni Barontini and Mauro Paternostro. Ultra-cold single-atom quantum heat engines. *New Journal of Physics*, 21(6):063019, June 2019.

[83] Andrew N. Jordan, Björn Sothmann, Rafael Sánchez, and Markus Büttiker. Powerful and efficient energy harvester with resonant-tunneling quantum dots. *Physical Review B*, 87(7):075312, February 2013.

[84] Björn Sothmann and Markus Büttiker. Magnon-driven quantum-dot heat engine. *EPL (Europhysics Letters)*, 99(2):27001, July 2012.

[85] M. Esposito, K. Lindenberg, and C. Van den Broeck. Thermoelectric efficiency at maximum power in a quantum dot. *EPL (Europhysics Letters)*, 85(6):60010, March 2009.

[86] Y. S. Liu, X. F. Yang, X. K. Hong, M. S. Si, F. Chi, and Y. Guo. A high-efficiency double quantum dot heat engine. *Applied Physics Letters*, 103(9):093901, August 2013.

[87] A. Vikström, A. M. Eriksson, S. I. Kulinich, and L. Y. Gorelik. Nanoelectromechanical Heat Engine Based on Electron-Electron Interaction. *Physical Review Letters*, 117(24):247701, December 2016.

[88] T. E. Humphrey, R. Newbury, R. P. Taylor, and H. Linke. Reversible Quantum Brownian Heat Engines for Electrons. *Physical Review Letters*, 89(11), August 2002.

[89] Martin Josefsson, Artis Svilans, Adam M. Burke, Eric A. Hoffmann, Sofia Fahlvik, Claes Thelander, Martin Leijnse, and Heiner Linke. A quantum-dot heat engine operating close to the thermodynamic efficiency limits. *Nature Nanotechnology*, 13(10):920–924, October 2018.

[90] Nathanaël Cottet, Sébastien Jezouin, Landry Bretheau, Philippe Campagne-Ibarcq, Quentin Ficheux, Janet Anders, Alexia Auffèves, Rémi Azouit, Pierre Rouchon, and Benjamin Huard. Observing a quantum Maxwell demon at work. *Proceedings of the National Academy of Sciences*, 114(29):7561–7564, July 2017.

[91] H. E. D. Scovil and E. O. Schulz-DuBois. Three-Level Masers as Heat Engines. *Physical Review Letters*, 2(6):262–263, March 1959.

[92] Heinz-Peter Breuer and Francesco Petruccione. *The Theory of Open Quantum Systems*. Oxford University Press, January 2007.

[93] R Alicki. The quantum open system as a model of the heat engine. *Journal of Physics A: Mathematical and General*, 12(5):L103–L107, May 1979.

[94] L. Szilard. über die Entropieverminderung in einem thermodynamischen System bei Eingriffen intelligenter Wesen. *Zeitschrift fü r Physik*, 53(11-12):840–856, November 1929.

[95] Shoichi Toyabe, Takahiro Sagawa, Masahito Ueda, Eiro Muneyuki, and Masaki Sano. Experimental demonstration of information-to-energy conversion and validation of the generalized Jarzynski equality. *Nature Physics*, 6(12):988–992, December 2010.

[96] Udo Seifert. Entropy Production along a Stochastic Trajectory and an Integral Fluctuation Theorem. *Physical Review Letters*, 95(4):040602, July 2005.

[97] Udo Seifert. Stochastic thermodynamics, fluctuation theorems and molecular machines. *Reports on Progress in Physics*, 75(12):126001, December 2012.

[98] C. Jarzynski. Nonequilibrium Equality for Free Energy Differences. *Physical Review Letters*, 78(14):2690–2693, April 1997.

[99] Gavin E. Crooks. Entropy production fluctuation theorem and the nonequilibrium work relation for free energy differences. *Physical Review E*, 60(3):2721–2726, September 1999.

[100] S Gasparinetti, P Solinas, A Braggio, and M Sassetti. Heat-exchange statistics in driven open quantum systems. *New Journal of Physics*, 16(11):115001, October 2014.

[101] Mihail Silaev, Tero T. Heikkilä, and Pauli Virtanen. Lindblad-equation approach for the full counting statistics of work and heat in driven quantum systems. *Physical Review E*, 90(2):022103, August 2014.

[102] Peter Talkner, Michele Campisi, and Peter Hänggi. Fluctuation theorems in driven open quantum systems. *Journal of Statistical Mechanics: Theory and Experiment*, 2009(02):P02025, February 2009.

[103] M. Kindermann and S. Pilgram. Statistics of heat transfer in mesoscopic circuits. *Physical Review B*, 69(15), April 2004.

[104] D. J. Wineland, R. E. Drullinger, and F. L. Walls. Radiation-Pressure Cooling of Bound Resonant Absorbers. *Physical Review Letters*, 40(25):1639–1642, June 1978.

[105] A. Aspect, E. Arimondo, R. Kaiser, N. Vansteenkiste, and C. Cohen-Tannoudji. Laser Cooling below the One-Photon Recoil Energy by Velocity-Selective Coherent Population Trapping. *Physical Review Letters*, 61(7):826–829, August 1988.

[106] Peter Pringsheim. Zwei Bemerkungen ü ber den Unterschied von Lumineszenz- und Temperaturstrahlung. *Zeitschrift fü r Physik*, 57(11-12):739–746, November 1929.

[107] S. I. Vavilov. Photoluminescence and thermodynamics. *J. Phys. USSR*, 10:499–401, 1946.

[108] S. I. Vavilov. Some remarks on the Stokes of fluorescent liquids. *J. Phys. USSR,*, 9:68–73, 1945.

[109] L. D. Landau. On the thermodynamics of photoluminescence. *J. Phys. USSR*, 10:503–506, 1946.

[110] Alfred Kastler. Quelques suggestions concernant la production optique et la détection optique d'une inégalité de population des niveaux de quantifigation spatiale des atomes. Application à l'expérience de Stern et Gerlach et à la résonance magnétique. *Journal de Physique et le Radium*, 11(6):255–265, 1950.

[111] Richard I. Epstein, Melvin I. Buchwald, Bradley C. Edwards, Timothy R. Gosnell, and Carl E. Mungan. Observation of laser-induced fluorescent cooling of a solid. *Nature*, 377(6549):500–503, October 1995.

[112] Seth D. Melgaard, Alexander R. Albrecht, Markus P. Hehlen, and Mansoor Sheik-Bahae. Solid-state optical refrigeration to sub-100 Kelvin regime. *Scientific Reports*, 6(1):20380, April 2016.

[113] Yurii V. Morozov, Shubin Zhang, Anupum Pant, Boldizsár Jankó, Seth D. Melgaard, Daniel A. Bender, Peter J. Pauzauskie, and Masaru Kuno. Can lasers really refrigerate CdS nanobelts? *Nature*, 570(7762):E60–E61, June 2019.

[114] Denis V Seletskiy, Richard Epstein, and Mansoor Sheik-Bahae. Laser cooling in solids: Advances and prospects. *Reports on Progress in Physics*, 79(9):096401, September 2016.

[115] G. Rupper, N. H. Kwong, and R. Binder. Large Excitonic Enhancement of Optical Refrigeration in Semiconductors. *Physical Review Letters*, 97(11):117401, September 2006.

[116] Mansoor Sheik-Bahae and Richard I. Epstein. Can laser light cool semiconductors? *Physical Review Letters*, 92(24):247403, June 2004.

[117] Richard Epstein and Mansoor Sheik-Bahae. *Optical Refrigeration: Science and Applications of Laser Cooling of Solids*. Wiley-VCH, Weinheim, 2009.

[118] Sergej Valer'evič Petruškin and Vitalij Vladimirovič Samarcev. *Laser Cooling of Solids*. Woodhead Publishing in Materials. Woodhead publ, Oxford (GB), 2009.

[119] Galina Nemova and Raman Kashyap. Twenty Years of Laser Cooling of Solids. *Journal of Physics: Conference Series*, 619:012037, June 2015.

[120] Galina Nemova and Raman Kashyap. Laser cooling of solids. *Reports on Progress in Physics*, 73(8):086501, July 2010.

[121] Erik M. Gauger and Joachim Wabnig. Heat pumping with optically driven excitons. *Physical Review B*, 82(7):073301, August 2010.

[122] P. R. Eastham, A. O. Spracklen, and J. Keeling. Lindblad theory of dynamical decoherence of quantum-dot excitons. *Physical Review B*, 87(19), May 2013.

[123] A. J. Ramsay, T. M. Godden, S. J. Boyle, E. M. Gauger, A. Nazir, B. W. Lovett, A. M. Fox, and M. S. Skolnick. Phonon-Induced Rabi-Frequency Renormalization of Optically Driven Single InGaAs / GaAs Quantum Dots. *Physical Review Letters*, 105(17):177402, October 2010.

[124] Paul A. Dalgarno, Jason M. Smith, Jamie McFarlane, Brian D. Gerardot, Kahled Karrai, Antonio Badolato, Pierre M. Petroff, and Richard J. Warburton. Coulomb interactions in single charged self-assembled quantum dots: Radiative lifetime and recombination energy. *Physical Review B*, 77(24):245311, June 2008.

[125] F. L. Curzon and B. Ahlborn. Efficiency of a Carnot engine at maximum power output. *American Journal of Physics*, 43(1):22–24, January 1975.

[126] F Schuda, C R Stroud, and M Hercher. Observation of the resonant Stark effect at optical frequencies. *Journal of Physics B: Atomic and Molecular Physics*, 7(7):L198–L202, May 1974.

[127] Michael E. Thomas. Multiphonon model for absorption in diamond. In Paul Klocek, editor, *SPIE's 1994 International Symposium on Optics, Imaging, and Instrumentation*, pages 152–159, San Diego, CA, September 1994.

[128] Christian Hepp, Tina Müller, Victor Waselowski, Jonas N. Becker, Benjamin Pingault, Hadwig Sternschulte, Doris Steinmüller-Nethl, Adam Gali, Jeronimo R. Maze, Mete Atatüre, and Christoph Becher. Electronic Structure of the Silicon Vacancy Color Center in Diamond. *Physical Review Letters*, 112(3):036405, January 2014.

[129] Yu Zhou, Abdullah Rasmita, Ke Li, Qihua Xiong, Igor Aharonovich, and Wei-bo Gao. Coherent control of a strongly driven silicon vacancy optical transition in diamond. *Nature Communications*, 8(1):14451, April 2017.

[130] K. V. Kepesidis, M.-A. Lemonde, A. Norambuena, J. R. Maze, and P. Rabl. Cooling phonons with phonons: Acoustic reservoir engineering with silicon-vacancy centers in diamond. *Physical Review B*, 94(21):214115, December 2016.

[131] Ariel Norambuena, Sebastián A. Reyes, José Mejía-Lopéz, Adam Gali, and Jerónimo R. Maze. Microscopic modeling of the effect of phonons on the optical properties of solid-state emitters. *Physical Review B*, 94(13), October 2016.

[132] Ariel Norambuena, Jerónimo R. Maze, Peter Rabl, and Raúl Coto. Quantifying phonon-induced non-Markovianity in color centers in diamond. *Physical Review A*, 101(2):022110, February 2020.

[133] H. Sternschulte, K. Thonke, R. Sauer, P. C. Münzinger, and P. Michler. 1.681-eV luminescence center in chemical-vapor-deposited homoepitaxial diamond films. *Physical Review B*, 50(19):14554–14560, November 1994.

[134] Chunlang Wang, Christian Kurtsiefer, Harald Weinfurter, and Bernd Burchard. Single photon emission from SiV centres in diamond produced by ion implantation. *Journal of Physics B: Atomic, Molecular and Optical Physics*, 39(1):37–41, January 2006.

[135] Jonas Nils Becker and Christoph Becher. Coherence Properties and Quantum Control of Silicon Vacancy Color Centers in Diamond (Phys. Status Solidi A 11/2017). *Physica Status Solidi A*, 214(11):1700586, 2017.

[136] Michael Kilgour and Dvira Segal. Coherence and decoherence in quantum absorption refrigerators. *Physical Review E*, 98(1):012117, July 2018.

[137] P. R. Eastham, P. Kirton, H. M. Cammack, B. W. Lovett, and J. Keeling. Bath-induced coherence and the secular approximation. *Physical Review A*, 94(1):012110, July 2016.

[138] Richard Hartmann and Walter T. Strunz. Accuracy assessment of perturbative master equations: Embracing nonpositivity. *Physical Review A*, 101(1):012103, January 2020.

[139] Archak Purkayastha, Abhishek Dhar, and Manas Kulkarni. Out-of-equilibrium open quantum systems: A comparison of approximate quantum master equation approaches with exact results. *Physical Review A*, 93(6):062114, June 2016.

[140] Junjie Liu and Dvira Segal. Coherences and the thermodynamic uncertainty relation: Insights from quantum absorption refrigerators. *Physical Review E*, 103(3):032138, March 2021.

[141] R.-E. Plessix. A review of the adjoint-state method for computing the gradient of a functional with geophysical applications. *Geophysical Journal International*, 167(2):495–503, November 2006.

[142] A. Strathearn, P. Kirton, D. Kilda, J. Keeling, and B. W. Lovett. Efficient non-Markovian quantum dynamics using time-evolving matrix product operators. *Nature Communications*, 9(1):3322, August 2018.

[143] Maria Popovic, Mark T. Mitchison, Aidan Strathearn, Brendon W. Lovett, John Goold, and Paul R. Eastham. Quantum Heat Statistics with Time-Evolving Matrix Product Operators. *PRX Quantum*, 2(2):020338, June 2021.